THE ROLE OF FIBULIN-5 IN THE GROWTH AND REMODELING OF MOUSE CAROTID ARTERIES

A Dissertation
Presented to
The Academic Faculty

by

William Wan

In Partial Fulfillment
of the Requirements for the Degree
Doctor of Philosophy in Bioengineering

Georgia Institute of Technology

December 2011

THE ROLE OF FIBULIN-5 IN THE GROWTH AND REMODELING OF MOUSE CAROTID ARTERIES

Approved by:

Dr. Rudolph L. Gleason, Jr., Advisor
School of Mechanical Engineering
School of Biomedical Engineering
Georgia Institute of Technology

Dr. W. Robert Taylor
School of Medicine
Emory University

Dr. Robert Guldberg
School of Mechanical Engineering
Georgia Institute of Technology

Dr. Evan Zamir
School of Mechanical Engineering
Georgia Institute of Technology

Dr. Manu Platt
School of Biomedical Engineering
Georgia Institute of Technology

Date Approved: October 27, 2011

To family and friends, new and old

ACKNOWLEDGEMENTS

The work presented in this dissertation could not have been completed without the technical help and moral support of colleagues, friends and family members. I would first like to thank Dr. Rudy Gleason for taking me into his new laboratory and for his mentorship. He constantly encouraged me to try new things in the lab and to struggle with experiments, sometimes seemingly endlessly, until they worked and I collected real data. He was very accessible when help was needed and allowed me to work things out at other times. Without sacrificing productivity, Rudy is among the most patient and thoughtful advisors. I would also like to thank my reading committee, Drs. Robert Guldberg, Manu Platt, W. Robert Taylor, and Evan Zamir for their comments and helpful discussions. They pushed me to think about the broader implications of my work and to be able to explain its importance to a more general audience. I would also like to acknowledge the critical discussions of our research and the insightful advice of Dr. Alexander Rachev. He was one of the few professors to encourage students to "save some work for tomorrow" and to enjoy life. I am also indebted to Dr. Hiromi Yanagisawa and Shelby Chapman at UT Southwestern for their generous help in starting our colony of fibulin-5 knockout mice. Given that my previous biology class was taken in high school in 1996, Shelby was especially patient in helping me learn the nuances of the knockout mice and in genotyping. I would also like to thank the professors whose classes I had the opportunity take. Near the end of my project, I also received the generous assistance of Drs. Luke Timmins and J. Brandon Dixon in analyzing collagen fiber angles from my multiphoton images and in critically reviewing one of our manuscripts. I would also like to thank the members of the Guldberg and García labs for allowing me to

borrow their bench space and equipment when genotyping my mice. They were always willing to unlock the PCR/Radiation room for me, and Kellie Templeman and David Dumbald were instrumental in helping me learn and troubleshoot PCR. I would also like to thank former and current managers of IBB core facilities in maintaining equipment critical to this project in working order. I also thank the staff of the PRL for taking care of our mouse colony.

Through the Cell and Tissue Engineering training grant, I had the opportunity to work at Genzyme as a Graduate Co-op. I would like to thank my managers at Genzyme, Tim Butler and Tom Jozefiak for the opportunity to work in an industrial R&D setting and to spend time in the New England region. My colleagues at Genzyme, both fulltime employees and co-ops were, very helpful in providing a well-rounded experience.

I would also like to thank my fellow graduate students for their support as this effort. The current and former members of the Gleason lab gave insightful advice in practice presentations, in discussing failed and successful experiments and provided comedic as well as stress relief. I would also like to thank Laura Hansen and Alex Caulk for taking care of my mice while I was in Boston. Thanks also go out to Alex Caulk and Roy Wang for introducing me to workouts at the CRC. The other students in Wing 2A of IBB also deserve mentioning as they provided equipment and advice whenever needed. I am also especially grateful for the friendship of former students, now postdocs elsewhere, Yap and Dave Bark. They were very helpful in troubleshooting experiments, discussing research ideas and for general graduate student stuff.

My parents, Steve and Melinda Wan have supported me through their love and patience in this adventure as well as in previous journeys. From my decision to become

an elementary school teacher to my return to graduate school in engineering, my parents have always been there to encourage me to get plenty of sleep and exercise. As a testament to their understanding, they never once complained when I told them that I was graduating at the end of the semester. For almost two years, I told them that I was gradating at "the end of the semester."

My journey through grad school at Tech would not have been nearly as fun without my non-lab friends. When I first moved to Atlanta, I taught elementary school in the Atlanta Public Schools system, and many of my teacher friends were still around I joined Georgia Tech. Ed Chang and Liz Boswell (now Liz Skolnicki) warrant special mention; our friendship began in early 2001 when we lived in Grant Park and shared in the adventures of first year teaching in APS. Ed and Liz were also the first to challenge me to explain how my research is more interesting and important than just "killing mice for their blood vessels." Many friends in the non-lab category include the fun people whom I have met through an ultimate frisbee game organized by Ben Johnstone. My frisbee friends were also instrumental in fulfilling my parent's desire for me to get adequate exercise and in following Dr. Rachev's advice for taking time to enjoy life.

My wife Claire, whom I met through the frisbee group, deserves her own paragraph among these acknowledgements. I could not have finished this dissertation with the same level of sanity without her love and support. From making yummy food at my defense to going on walks/runs to organizing social outings, Claire was also instrumental in helping me get enough sleep and exercise. Like my parents, she was also extremely patient when I once told her a paper would be finished "next week." I am honored that she joined me in this adventure as well as many more to come.

TABLE OF CONTENTS

LIST OF TABLES

LIST OF FIGURES

LIST OF ABBREVIATIONS

3D	3-dimensional
AAA	Abdominal aortic aneurysm
AMD	Age-related macular degeneration
ANOVA	Analysis of variance
CVD	Cardiovascular disease
DANCE	Developmental arteries and neural crest EGF-like
ECM	Extracellular matrix
EGF	Epidermal derived growth factor
EVEC	Embryonic vascular EGF-like repeat-containing protein
f-l	Axial force-length
fbln5	Fibulin-5
fbln5$^{-/-}$	Fibulin-5 null
fbln5$^{+/+}$	Fibulin-5 wildtype
IP	Intraperitoneal
KO	Fibulin-5 knockout/null
LTBP-2	Latent transforming growth factor-beta-binding protein 2
μCT	Micro-computed tomography
μm	Micrometers
mmHg	Millimeters of mercury
mN	Millinewtons
P-d	Pressure-diameter

SEM	Standard error of the mean
SHG	Second harmonic generation
SMC	Smooth muscle cell
US	United States of America
WT	Wildtype

SUMMARY

The evolution of biomechanical behavior of arteries plays a key role in the on-set and progression of cardiovascular disease. Elevated arterial stiffness, for example, is a key predictor of subsequent cardiovascular events. Arterial stiffening occurs naturally with aging and in disease and is often associated with the loss of functional elastic fiber and increased collagen deposition. Indeed, the biomechanical behavior is governed by the content and organization of the key structural constituents (e.g., collagen, elastin, and smooth muscle) and vessel geometry. The evolution of biomechanical behavior of arteries is governed by biologically-mediated synthesis, degradation, and reorganization of these key structural constituents. A hallmark goal in biomechanics is quantifying the relationship between the microstructure of tissues and their mechanical response throughout tissue growth and remodeling; this will provide a crucial link in understanding the tissue level effects of biological processes involved in disease and normal growth.

Fibulin-5 (*fbln5*) is an ECM protein that binds tropoelastin and interacts with integrins. Knockout mice lacking *fbln5* exhibit loose skin, are prone to pelvic organ prolapse and have tortuous arteries. Mutations of the *fbln5* gene are also linked to human diseases such as cutis laxa syndrome, prostate cancer and age-related macular degeneration. Arteries from *fbln5* knockout mice lack functional elastic fibers and provide a system for investigating the link between an artery's microstructure and its mechanical response. The overall goal of this project was to develop multi-scaled theoretical and experimental frameworks to quantify the relationship between microstructural content and organization and tissue level material properties of arteries

from *fbln5* null mice and littermate controls and to quantify the effects of *fbln5* on the *in vivo* maturation of mouse carotid arteries.

We found that common carotid arteries from adult *fbln5*$^{-/-}$ mice exhibited lower *in vivo* axial stretch and lower *in vivo* stresses while maintaining a similar compliance over physiological pressures compared to littermate controls. We developed a novel imaging technique to image cells, collagen and elastin in live pressurized and stretched arteries and found that carotid arteries from *fbln5*$^{-/-}$ mice lack distinct functional elastic fibers defined by the lamellar structure of alternating layers of smooth muscle cells and elastin sheets. These data suggest that structural differences in *fbln5*$^{-/-}$ arteries correlate with significant differences in mechanical properties.

During maturation we found significant differences the in evolution of mechanical and material properties between wildtype and knockout mice. The *in vivo* axial stretch ratio increased between 3 and 13 weeks in wildtype arteries while in knockout arteries there were no statistically significant differences. In addition, the opening angle of wildtype arteries decreased during maturation while the opening angle of knockout vessels maintained similar levels. During maturation, wildtype vessels experience significant changes in *in vivo* axial force and compliance while knockout vessels do not undergo such changes. Parameter estimation results suggest that the altered growth and remodeling takes place through changes in material properties as well as through microstructural properties. The results of this study suggest that the lack of fbln5 causes altered material and microstructural properties in mouse carotid arteries, and changes in these properties take place at different time scales.

In addition, we developed a microstructurally-motivated 3-dimensional (3D) constrained mixture computational framework for vascular growth and remodeling. This model incorporates microstructurally-motivated kinematics and a structurally motivated constitutive equation. We simulated conditions of altered pressure and flow in the presence or absence of elastin turnover, using physiological rates of constituent growth turnover and found that simulated results capture the salient findings found in the literature.

We measured collagen fiber angles in mouse carotid arteries under various loading conditions, quantified the degree of affine motion exhibited and used the fiber angle distribution in structurally motivated constitutive relations. Incorporating experimentally measured fiber angle data into four-fiber and fiber distribution constitutive relations yielded similar fitting errors; however, when using mean parameters to predict experimental data, the constitutive relation accounting for the entire fiber distribution yielded greater predictive accuracy.

This dissertation incorporates experimental data quantified at the micro (microstructural-level fiber distributions) and macro (tissue-level mechanical response) scale and incorporates these data into microstructurally motivated constitutive relations.. The use of structurally motivated constitutive relations and experimentally measured microstructural data provides a foundation for future work in further understanding the relationship between processes governing microstructure and the tissue level effects of disease and normal growth.

CHAPTER 1

INTRODUCTION

Cardiovascular disease (CVD) is the leading cause of death in the US, accounting for approximately 1 in every 6 deaths (120). Diseased arteries often undergo physical adaptations such as increased arterial wall thickness due to hypertension (161), maladaptations such as wall thinning and vessel dilation in aneurysm formation, and intimal hyperplasia with restenosis following angioplasty (87). Many of these physical phenomena have a biological basis such as SMC hypertrophy in the case of hypertension (111), upregulation of matrix metalloproteinases in aneurysm formation (86, 143) and SMC migration in intimal hyperplasia (106, 126). Examples of treatments for vascular diseases include drugs for hypertension (97), balloon angioplasty with stents for arterial stenosis (33, 141), and drug eluting stents for the prevention of stent thrombosis (70, 100). Indeed, mechanically-mediated vascular growth and remodeling mechanisms play a key role in the development and progression of CVD and the success (or failure) of clinical interventions; examples include atherosclerosis, arteriosclerosis, hypertension, aneurysms, and outcomes of by-pass grafts and angioplasty (81, 157). Thus, vascular diseases manifest physically, have a biological basis, and are treated through both mechanical and biochemical techniques (drugs). A multiscaled approach towards studying vascular growth and remodeling may reconcile experimental observations made at the microstructural level with observations made at the tissue level, provide insight into the mechanical effects of biological changes that take place at the cellular level, and may lead to the discovery of novel intervention strategies.

Research in CVD spans multiple disciplines and experimental scales from examining signaling molecules to measuring the mechanical properties of atherosclerotic arteries. Understanding the relationship between biological processes that give rise to the structure of arteries and the artery's mechanical response will provide insight into disease progression, allow prediction of long-term intervention outcomes, and may motivate new therapeutics and interventions. This may also provide insight into effects of different interventions such drugs that can alter biological processes or physical interventions such as angioplasty that alter mechanical properties. Experimental techniques that measure arterial microstructure and mathematical models that calculate mechanical response based on arterial constituents can establish a crucial link in the connection between local biological processes and tissue mechanical response.

This study seeks to quantify the relationship between arterial microstructure and mechanical response by studying the evolution of microstructure and of mechanical properties of arteries from *fbln5* knockout (KO) and wildtype (WT) mice. The **central hypothesis** is that, without functional elastic fibers, carotid arteries of mice lacking *fbln5* will exhibit a stiffer mechanical response due to growth and remodeling that has increased collagen and smooth muscle cell content relative to WT controls. The effects of the growth remodeling process can be quantified in terms of the artery's microstructural and mechanical properties and used to develop predictive mathematical models of growth and remodeling.

Aim 1: Quantify the biomechanical and microstructural differences in common carotid arteries of adult *fbln5* null and wildtype (WT) mice during maturation. Our

working hypothesis is that the lack of functional elastic fibers in *fbln5* null mice will cause changes in the microstructure and mechanical response of carotid arteries leading to increased stiffness and decreased axial prestretch, and these differences will become increasingly apparent throughout the maturation.

Phenotypic differences between KO and WT mice do not appear until 3 weeks of age, suggesting an age-dependent onset of physical adaptations to the lack of functional elastic fibers. Quantifying the microstructural changes of arteries from *fbln5* KO mice in parallel with those in WT mice will reveal insight into the relationship between microstructure evolution and the evolution of mechanical properties. This data may also be used to develop constitutive relations that use microstructure to predict mechanical response and to develop evolution equations that describe the evolution of microstructure during growth and remodeling. Mouse carotid arteries are geometrically advantageous as they contain relatively few bends, and their length to diameter ratio allows biaxial testing while neglecting end effects of the mounting sutures. The wall thickness of the mouse carotid artery also allows confocal microscopy of the entire thickness of the wall from the lumen to the adventitia. In humans, carotid artery tortuosity is linked to aging (21). Carotid arteries from *fbln5*$^{-/-}$ mice are tortuous and often looped, while arteries from *fbln5*$^{+/+}$ mice appear similar to WT mice.

Aim 2: Develop microstructurally-motivated constitutive and stress-mediated evolution equations that quantify changes in arterial biomechanical behavior that occur during growth and remodeling and maturation. Our *working hypothesis* is that the evolution of mechanical behavior can be described using measurable metrics that describe cell and ECM content and organization.

Vascular diseases are often characterized by changes in tissue level mechanical properties (31, 148) and by changes at the microstructural level (11, 18, 26, 58, 74). This suggests that correlating microstructural configuration to the mechanical properties of tissues can provide insight into the progression of disease and inform treatment. Microstructurally motivated constitutive relations offer a physically meaningful method for relating local microstructure to local mechanical properties. This study will extend structural based constitutive relations and incorporate microstructural data such as constituent mass fractions and fiber angles in the mathematical modeling of arteries (56).

Previous experiments have been established that suggest that arteries grow and remodel to restore wall stresses to homeostatic levels (73, 76, 98). Matsumoto and Hayashi showed that arterial wall thickness increased in hypertensive rats, suggesting that circumferential (hoop) stress was a target for growth and remodeling. A leftward shift in pressure-circumferential stretch ratio curves suggested that strain was not a target for growth and remodeling (98). Stress-mediated evolution equations will describe the changes in mass within the vessel wall based on the local mechanical environment that cells are experiencing. Rather than prescribing the geometric consequences of growth (119, 131), we prescribed the cell-mediated processes by which growth and remodeling occurs – changes in the production and removal of constituents such as elastin, collagen, and SMC (67). This provides a more physiologically motivated description of the biological environment and provides a tool for predicting and investigating changes occurring at the cellular level. Evolving the mass at the constituent level allows the study of effects of knocking out certain genes or the influence of different physical elements of the vessel wall.

CHAPTER 2

BACKGROUND AND LITERATURE REVIEW

Cardiovascular disease (CVD) is the leading cause of death in the US and results in a yearly loss of productivity of over $20 billion USD (92). The death rate from CVD has declined in recent years, while the number of hospital discharges due to CVD has increased (142). This research area presents an opportunity for developing tools for reducing mortality and improving quality of life. Vascular diseases include atherosclerosis, arteriosclerosis, hypertension and aneurysms, and a leading predictor of these diseases is arterial stiffening (81, 157). Diseased arteries undergo physical adaptations such as increased arterial wall thickness due to hypertension (161) and maladaptations such as wall thinning in aneurysm formation. The physical manifestations of CVD necessitate in depth study of the mechanics of arteries as well as their growth and remodeling processes.

Vascular Mechanics

Blood vessels are composite structures consisting of living cells and an ECM, with the major load bearing components consisting of smooth muscle cells (SMC), elastin and collagen. Roach and Burton postulated that the mechanical response of arteries at low pressures was due to elastin while at high pressures, collagen prevents over extension of the vascular wall (118). The endothelium, a single layer of endothelial cells, is the innermost layer an artery and is separated from the media by a fenestrated sheet of elastic tissue, the internal elastic lamina. The media consists of concentric sheets of SMC separated by collagen fibers and elastin. The outermost layer of an artery, the adventitia, limits excessive deformation at high pressures (68) and consists of collagen

fibers and fibroblasts. Smooth muscle cells contract and relax in the presence of vasoactive agents released by endothelial cells or introduced exogenously. For example, in response to an increase in flow rate, endothelial cells upregulate the expression of vasodilatory compounds (e.g., nitric oxide) which relaxes SMC and the cells also downregulate the expression of vasoconstricting agents (e.g., endothelin-1) which constricts SMC; this process increases vessel caliber restoring wall shear stress on the endothelium (75). In addition, hypertensive patients have higher levels of arterial endothelin-1 expression, a potent vasoconstrictor (124).

In vivo, blood vessels are mechanically loaded by pressure, axial force and fluid shear stress; thus, cells within the blood vessel experience multi-axial loading. Given geometry and applied loads, universal solutions (e.g., LaPlace's Law) may be used to calculate mean wall stresses and knowledge of material properties is not necessary. However, constitutive relations are required to calculate the stress distribution through the arterial wall. In contrast to earlier phenomenological blood vessel models (22, 38), recent constitutive relations for blood vessels use a structural approach and consider physical attributes such as fiber angles (63, 174). Constitutive relations that consider the microstructure of the artery correlate tissue level mechanical behavior to physically measureable microstructural parameters such as fiber angles, undulations and mass fractions of constituents. Recent advances in confocal microscopy permit the imaging of microstructure of blood vessels (95, 172). Despite advances in imaging and in modeling theories, there remains a need to validate these models using experimental data and a need for developing experimental techniques to quantify microstructural data.

Growth and Remodeling

Blood vessels grow and remodel in response to altered loading conditions, and the resulting adaptations often appear to restore local walls stresses to homeostatic values (73, 76, 98). As blood vessels adapt to development, maturation, aging, exercise, or disease via growth and remodeling, not only do their physical dimensions change, but their mechanical properties such as stiffness and compliance change as well. Under normal conditions, local stresses within the blood vessel appear to be maintained at homeostatic values. Cells and the ECM can undergo reorganization and changes in turnover rates to restore homeostatic loading conditions. For example, blood vessels in rats loaded under hypertensive conditions have been shown to increase in outer diameter and increase in the ratio between media thickness and lumen diameter while maintaining constant wall stresses at the mean blood pressure (167). In flow induced remodeling, rat carotid arteries have been shown to increase in luminal area under higher flow and decrease in luminal area under low flow (102). Furthermore, rabbit carotid arteries subject to an increase in axial strain have been shown to remodel to normal axial stress values within one week (73). These studies also suggest that growth and remodeling is a multi-axial phenomenon and a key feature of blood vessels.

Growth and remodeling models

Mathematical descriptions of growth and remodeling have taken on different forms over time. In the early 1980s, Skalak et al proposed a theory for finite volumetric growth that allowed for the development of residual stresses within tissues and defined velocities of surface growth (128, 130). These ideas were later extended by many others to define volumetric growth in terms of stress-dependent relations (36, 112, 119). In this

framework, growth and remodeling is defined as changes in the zero-stress states of material (e.g. cells and ECM proteins) in local region. The zero-stress states of the local materials are allowed to evolve independently (deformation gradient $\mathbf{F}_g$) in a manner that need not be continuous. Finally, the local material is then mapped or assembled into a continuous, traction-free configuration (deformation gradient $\mathbf{F}_a$) that is then residually stressed. Under loads applied to the traction-free configuration (deformation gradient $\mathbf{F}_e$), the overall deformation gradient becomes $\mathbf{F}=\mathbf{F}_e\mathbf{F}_a\mathbf{F}_g$. In contrast to the volumetric growth approach, Fung suggested an approach in which mass evolves in a stress-dependent manner (39). Microstructurally-motivated approaches attempt to account for the heterogeneous (e.g. SMC, collagen fibers and elastin) nature of biological tissues (27, 50, 80, 146), and these approaches differ in the manner that they evolve constituents and the constitutive relations used. Humphrey and Rajagopal proposed a constrained mixture theory in which, individual constituents are deposited at homeostatic stretches that are not necessarily equal between different types of constituents (67). In this framework, altered mechanical loading causes existing constituents that are now stretched beyond homeostatic values to be removed and replaced with new constituents deposited at their respective homeostatic stretches. The removal of old and the addition of new constituents evolve the stress-free state of the overall tissue (44, 51). Whether defined through volumetric growth or through evolving masses fractions of constituents, experimentally validating these frameworks for growth and remodeling remains on open problem. This dissertation extends the constrained mixture approach (50) into 3-D framework using structural parameters that can be experimentally quantified (3, 95, 101, 145).

Evolution Equations

Under pathological conditions, growth and remodeling can occur without the complete restoration of homeostatic wall stresses. In aneurysms, changes in mechanical properties can include increases in wall stresses (31, 148) while various biological processes that occur can include elastin degradation (11, 18), upregulation of collagenase (10), and SMC apoptosis (58, 74). Thus, understanding the relationship between the evolving microstructure of blood vessels and their evolving mechanical properties may provide insight into the development and progression of vascular diseases. Examples of these insights include quantifying aneurysm growth or quantifying the rate of arterial stiffening with aging. Mathematical models offer the potential to simulate growth and remodeling and provide a possible timeline of disease progression. Evolution equations can describe the growth and remodeling process and can adopt various forms; early reports of stress as a possible target for regulating homeostasis prompted the development of volumetric approaches for modeling the growth and remodeling of tissues (119, 131). While these initial theories captured the overall geometric changes of growth and remodeling, they do not predict the evolution of microstructure within the vessel wall such as changes in volume fractions of constituents. Evolution equations that predict local microstructural changes provide a more physiological description of the cell-mediated processes that take place during growth and remodeling (156). Employing a constrained mixture approach, Gleason et al. have shown that evolution equations based on first order kinetics can capture key features of growth and remodeling such as the turnover and production of various ECM components (50). Because stress appears to be a

target for growth and remodeling (98, 99), this project proposes new stress-mediated evolution equations for simulating growth and remodeling (153).

The use of mathematical models to quantify the evolution of microstructure and to predict mechanical responses may reveal new insights into the progression and characterization of vascular diseases. Evolution equations that predict changes in microstructure along with constitutive relations that use microstructure to predict local mechanical responses will help elucidate the link between biological processes that occur at the cellular level with changes that take place at the tissue level. Developing and validating mathematical models is greatly enhanced through the use of genetic KO animal models. Knockout animals provide a system for studying the effects of a single gene and provide a means of testing the descriptive and predictive capabilities of mathematical models.

Constitutive Equations

Vascular diseases are often characterized by changes in tissue level mechanical properties such as geometry and opening angle (88, 93, 148) and by changes at the microstructural level such as elastin degradation (11, 18), and SMC apoptosis and migration (26, 58, 74). This suggests that knowledge of both microstructural configuration as well as the mechanical properties of tissues can provide insight into the progression of disease and inform treatment. Current technologies such as ultrasound and magnetic resonance imaging may be used to estimate properties such as compliance and pulse wave velocity over physiological loading conditions (110); however, they do not characterize the local mechanical environment at cellular length scales. The fundamental inability of most mechanical tests to experimentally measure the *in situ* local mechanical

environment necessitates the use of constitutive relations, which offer a mathematical approach for predicting the local mechanical response of tissues. Furthermore, the local mechanical environment may provide better correlations to the local biological response (14). Microstructurally motivated constitutive relations offer a physically meaningful method for relating local microstructure to local mechanical properties. Various forms of constitutive relations for blood vessels have been proposed, from purely phenomenological based (16) to more structurally-motivated forms (63). Because biological-mediated cell and ECM production, degradation, and remodeling determine an artery's microstructure which determine its mechanical properties, microstructurally-motivated constitutive relations play a key role in correlating biological responses to wall stresses. With advances in imaging technology (42) that permit in vivo imaging of tissue heterogeneities, predicting clinically relevant mechanical parameters using tissue microstructure may soon become a reality. Recent constitutive relations for arteries provide a framework for describing both material and structural properties (56, 63, 156). These models can incorporate parameters that describe microstructural organization such as fiber distributions (56), fiber angles (63), fiber crimping (156), and constituent volume fractions (67), amongst others. This study will extend structural based constitutive relations and incorporate microstructural data such as constituent mass fractions and fiber angles in the mathematical modeling of arteries (56).

The mechanical response of individual constituents within blood vessels is determined by geometry, organization, and level of crosslinking as well as other properties. Thus, material parameters determined through nonlinear regression represent an aggregate effect of these properties rather than a single material property such as

modulus. For example, in skin from fbln5 knockout mice, desmosine levels are decreased, but tropoelastin levels are not significantly different (15, 171). In this case material parameters describing elastin may account for both the level of crosslinking as well as the mechanical response of elastic fibers. Collagen and elastin are cross-linked in processes mediated by lysyl oxidases (17), and inactivation of the murine LOX gene causes cardiovascular abnormalities such as aneurysms and elastin fragmentation (64, 94). Collagen can also be enzymatically cross-linked by transglutaminases (54) and through nonenzymatic cross-linking by glycation (116, 117). Changes in elastin and collagen crosslinking can ultimately change the constituent's mechanical response without changing mass fraction or tissue-level geometry; thus, material parameters estimated from constitutive relations must be interpreted carefully. A commonly used four-fiber constitutive relation for arteries utilizes material parameters describing properties of fibers at orthogonal and diagonal angles (4). The interpretation of these material parameters should consider that the mechanical response of the constituent maybe due in part to the level of crosslinking of fibers to each other as well as the collective mechanical response of the fibers themselves. The material parameters estimated from constitutive relations used in this dissertation do not discern the level of cross-linking, rather they describe the overall mechanical response of the constituent.

Affine motions

Affine motions are defined as those in which a material deforms identically both microscopically and macroscopically, and in the case of biological tissues, affine deformations are characterized by cells and fibers deforming according to the overall deformation of the tissue (59). Commonly used constitutive relations (16, 63) assume

affine deformations; however, some studies suggest that local deformations of individual microstructural constituents do not always follow the deformation of the tissue as a whole (6). Blood vessels are often tested under quasistatic conditions with the assumption that they behave pseudoelasticity (37), and the resulting data is used in constitutive equations that often assume affine deformations. Using small angle light scattering, Billiar et al. found that porcine aortic valve leaflets and bovine pericardium undergo non-affine deformations under certain configurations of biaxial stretching (6). Studies of porcine small intestinal submucosa (SIS), also using small angle light scattering, suggest that biaxial deformations are affine while uniaxial deformations are non-affine (43). In human tissues, fibers in the annulus fibrosus appear to undergo affine fiber motion during tensile loading (55) while collagen fibers in the supraspinatus tendon undergo affine motions only in specific loading orientations (82). It is yet unknown whether blood vessels undergo affine deformations and whether affine deformations for blood vessels only encompass a subset of deformations experienced during biaxial testing. Studies of collagen gels also suggest non-affine fiber kinematics (12). Parameter estimation studies of arterial biaxial mechanical test data often results in model predictions that match the experimental data to different extents at different stretches (56), which suggests that the accuracy of prediction for the constitutive model varies according to the type and magnitude of deformation.

Maturation

Throughout maturation, the mechanical properties of the mouse cardiovascular system evolve in both the circumferential and axial directions. Cardiac output also undergoes changes that, along with changes geometry, affect wall shear stresses.

Observations of 129/SvEv and C57BL/6 strains of mice reveal that, within the first 30 days after birth, the mean blood pressure more than doubles (66, 71), and after postnatal day 35, mean arterial pressure continues to increase (71, 144). Wiesmann et al. found that mean body weight of C57BL/6 mice increased from 2.2 g at postnatal day 2 to 26.6 g at week 16 (159). They also found that left ventricular cardiac output increased from 1.1 ml/min at postnatal day 2 to 14.3 ml/min at week 16. In another study of C57BL/6 mice mean adult blood pressure was reached at the 2 weeks of age (66). Despite the vast body of knowledge detailing cardiovascular changes during maturation, there remains a need to quantify the structural and material properties of arteries during maturation.

Fibulin-5

Fibulin-5 (*fbln5*), also known as DANCE (developmental arteries and neural crest epidermal growth factor-like) or EVEC (embryonic vascular epidermal growth factor-like repeat-containing protein), is an ECM protein that is critical for elastic fiber formation and is expressed in developing arteries as well as balloon injured and atherosclerotic arteries (104, 105). The *fbln5* protein has been mapped to human chromosome 14q32.1 and consists of 488 amino acids and contains six epidermal growth factor (EGF)-like domains with an RGD motif in the first EGF-like domain. The amino acid sequence of *fbln5* is well conserved between mice, rats and human variants with at least 94% identical sequences (77, 105). Fibulin-5 is localized to fibrillin-1 microfibrils (34) and binds to tropoelastin (164) and to $\alpha_V\beta_3$ integrins (104). Tropoelastin coacervation, a necessary step prior to crosslinking into mature elastic fibers, appears to be mediated by *fbln5* (61, 149). Localization to fibrillin-1 appears to be regulated by latent transforming growth factor-beta-binding protein 2 (LTBP-2) while the knockdown of LTBP-2 promotes the

localization of *fbln5* to fibrillin-2 microfibrils (60). In aged mice, the expression of truncated *fbln5*, a form that does not promote elastic fiber formation, increases with age while full-length *fbln5* diminishes with age (61). Fibulin-5 has been observed to be an antagonist for angiogenesis (1) as well as a suppressor of tumor growth (2, 163). Analysis of skin from WT and *fbln5* KO mice revealed that the absence of *fbln5* also upregulates the expression of fibulins2, fibulin-4, lysyl oxidase and lysyl oxidase like-1 (15). Fibulin-5 interacts with $\alpha5\beta1$ and $\alpha4\beta1$ integrins; however, SMC plated on *fbln5* exhibited reduced migration when compared to cells plated on fibronectin (91).

Mice lacking both alleles of the *fbln5* gene experience loose skin, emphysema and tortuous blood vessels (104, 164). Large arteries from KO mice (*fbln5*$^{-/-}$) have a greater number of branches than WT mice (136). Endogenous *fbln5* also influences angiogenesis by regulating levels of vascular endothelial growth factor and angiopoietins. Fibulin-5 may also regulate vascular redox state through binding of extracellular superoxide dismutase (108). Polyvinyl alcohol sponges implanted in KO mice exhibited greater infiltration of blood vessels than polyvinyl alcohol sponges implanted into WT mice (136). Overexpression of *fbln5* via retrovirus transfection enhances wound healing in rabbits; this was characterized by greater wound closure as well as increased collagen type 1 synthesis (85). In KO mice, however, *fbln5* deficiency did not affect wound healing and did not affect breaking strength of skin from healed full thickness wounds (170). This suggests that endogenous *fbln5* may have different effects than the over-expressed version of the protein. Fibulin-5 also affects the proliferation and migration of SMC. Carotid artery ligation in KO mice produced greater neointima formation and thrombus formation when compared to ligation of carotid arteries from WT mice. The

loss of *fbln5* prevented formation of mature elastin and allowed overproliferation of SMCs (133). Double knockout mice of *fbln5* and fibulin-2 have disrupted internal elastic laminae (13). Fibulin-5 is also expressed in lung fibroblasts (79) and may have a role in lung injury repair (78).

Phenotypic consequences of mutations in the *fbln5* have also been characterized in humans. Homozygous mutations of the *fbln5* gene have led to a severe form of cutis laxa syndrome with one month old infants exhibiting loose skin in the face and neck. Adults have skin, cardiac and lung features similar to those found in *fbln5* KO mice. Humans with mutations of only one *fbln5* allele appear phenotypically normal (20, 90). In lung cancer samples, *fbln5* expression was decreased while over expression of *fbln5* in cell lines prevented metastasis in mice (166). In prostate and bladder cancer tissue samples, *fbln5* was shown to be downregulated (65, 160). Fibulin-5 is expressed in aging human eyes and found in extracellular deposits associated with age-related macular degeneration (AMD) (103); missense variations of *fbln5* have been found in a subset of AMD patients (134). Sato et al. found increased *fbln5* expression in major portal vein branches of livers with idiopathic portal hypertension (123). Illustrating the role of *fbln5* in maintaining intact elastic fibers, tissue samples from thoracic aortic dissection patients demonstrated decreased levels of *fbln5* expression (155).

Altered expression of *fbln5* plays a key role in a variety of pathologies involving elastic tissues, and as an angiogenesis inhibitor, *fbln5* expression also appears to be linked to certain cancers. Its interaction with integrins, lysyl oxidase, extracellular superoxide dismutase, tropoelastin and microfibrils results in pathologic effects when *fbln5* is downregulated or silenced. Despite a vast amount of observations on the

biochemistry and molecular interactions of *fbln5*, its role in vascular mechanics and growth and remodeling remains a relatively unexplored area. The *fbln5* KO mouse provides a means for developing constitutive relations and evolution equations for growth and remodeling. This study will utilize the unique properties of KO mice to study growth and remodeling of carotid arteries. This mouse model, with altered growth and remodeling characteristics and stiffer, tortuous vasculature, presents a unique scenario for studying the implications of altered microstructure on the mechanical response of arteries.

CHAPTER 3

BIOMECHANICAL AND MICROSTRUCTURAL PROPERTIES OF COMMON CAROTID ARTERIES FROM FIBULIN-5 NULL MICE

Introduction

Alteration in the mechanical properties of arteries occurs with aging and disease and arterial stiffening is a key risk factor for subsequent cardiovascular events. Arterial stiffening is associated with the loss of functional elastic fibers and increased collagen content in the wall of large arteries. Arterial mechanical properties are controlled largely by the turnover and reorganization of key structural proteins and cells, a process termed growth and remodeling. Fibulin-5 is a microfibrillar protein that binds tropoelastin, interacts with integrins, and localizes to elastin fibers; tropoelastin and microfibrillar proteins constitute functional elastin fibers. We performed biaxial mechanical testing and confocal imaging of common carotid arteries from *fbln5* null mice (*fbln5*$^{-/-}$) and littermate controls (*fbln5*$^{+/+}$) to characterize the mechanical behavior and microstructural content of these arteries; mechanical testing data were fit to a four fiber-family constitutive model. We found that carotid arteries from *fbln5*$^{-/-}$ mice exhibited lower *in vivo* axial stretch and lower *in vivo* stresses while maintaining a similar compliance over physiological pressures compared to littermate controls. Namely, for *fbln5*$^{-/-}$ the axial stretch λ_z=1.4±0.07, the circumferential stress σ_q= 101±32 kPa, and the axial stress σ_z = 74±28 kPa; for *fbln5*$^{+/+}$, λ_z = 1.64±0.03, σ_q = 194±38 kPa, and σ_z = 159±29 kPa. Structurally, carotid arteries from *fbln5*$^{-/-}$ mice lack distinct functional elastic fibers defined by the lamellar structure of alternating layers of SMC and elastin sheets. These data suggest that structural differences in *fbln5*$^{-/-}$ arteries correlate with significant differences in

mechanical properties. Despite these significant differences *fbln5*$^{-/-}$ carotid arteries exhibited nearly normal levels of cyclic strain over the cardiac cycle.

Methods

Surgical preparation and vessel isolation

Adult male mice, *fbln5*$^{-/-}$ (13±5 weeks old, *n*=6) and *fbln5*$^{+/+}$ (13±1 weeks old, *n*=7) littermate controls on the C57-BL6 X 129/SvEv background were anesthetized with sodium pentobarbital (100 mg/kg IP). All mice were produced from a breeding pair originally obtained from Dr. Hiromi Yanagisawa (UT Southwestern). Under sterile conditions, both common carotid arteries were excised, placed in fresh culture medium, dissected free of perivascular tissue, and mounted on the glass cannulae of our biomechanical testing device using sterile suture (46). All animal procedures were approved by the Institute Animal Care and Use Committee (IACUC) at the Georgia Institute of Technology.

Biomechanical testing

A device modified from one reported by Gleason et al (46) was used to perform cylindrical biaxial biomechanical and vasoreactivity tests and to perform multi-photon, confocal microscopy. Pressure-diameter (*P*-*d*) data were collected from 0 to 180 mmHg at constant axial extensions, and axial force-length (*f*-*l*) data were collected over cyclic axial extensions up to λ = 1.70 for *fbln5*$^{+/+}$ arteries and λ = 1.55 for *fbln5*$^{-/-}$ arteries at constant pressures, P = 60, 100, and 160mmHg. Here, $\lambda = l/L$ where l is the current length and L is the original unloaded length; l and L were measured as the distance between mounting sutures. The *in vivo* axial stretch ratio was defined as the stretch for

which axial force remains nearly constant during the pressurization cycle (24, 140). *P-d* tests were performed at stretches above and below the *in vivo* axial stretch ratio and were performed at different sets of axial extensions for *fbln5*$^{-/-}$ and *fbln5*$^{+/+}$ arteries. All *P-d* and *f-l* tests were performed quasi-statically over 3 loading-unloading cycles, and to prevent damage from over stretching, the maximum axial load was limited to 9 mN and 4.4 mN for *fbln5*$^{+/+}$ and *fbln5*$^{-/-}$ vessels, respectively. Tests were performed in the same order for all vessels; *P-d* at $\lambda <$ *in vivo* axial stretch, *P-d* at $\lambda \sim$ *in vivo* axial stretch, *P-d* at $\lambda >$ *in vivo* axial stretch, *f-l* at $P = 60$, *f-l* at $P = 100$, and *f-l* at $P = 160$mmHg. Vessel wall thickness was measured using a custom video-caliper LabView subroutine by measuring the inner and outer diameter of the vessel following Gleason et al., (46).

Immediately following these ('basal') biomechanical tests, vessels were loaded to $P = 90$ mmHg and $\lambda =$ *in vivo* axial stretch ratio, and allowed to stabilize for 15 minutes. Contractile function was then assessed by measuring relative changes in diameter and axial force in response to the sequential administration vasoactive agents to the bathing media: phenylephrine or norepinephrine to elicit smooth muscle cell contraction, carbamylcholine chloride to elicit endothelial-dependent dilation, and sodium nitroprusside to elicit endothelial-independent dilation (46). Values of diameter and axial force were normalized to values measured at the end of the 15-minute recovery period.

Opening Angle

It is well known that the traction free configuration of arteries is typically not stress-free; rather these unloaded vessels contain residual stresses (16). To quantify the degree of residual stress in these arteries, opening angle measurements were made. Multiple unloaded rings were cut from excised carotid arteries (17 *fbln5*$^{-/-}$ and 12 *fbln5*$^{+/+}$

total), and a single radial cut was imposed, which caused the vessel rings to spring open, relieving much of the residual stress. The opening angle, Φ_0, was calculated as

$$\Phi_0 = \pi - \frac{L_o - L_i}{2H} \quad \text{and} \quad A = \frac{H(L_o + L_i)}{2} \tag{3.1}$$

where the second term on the right-hand side of equation $(3.1)_1$ is the angle of the open sector as defined by Chuong and Fung (16), L_o and L_i are the outer and inner arc lengths of the stress-free sector, H is the wall thickness of the stress-free sector and A is the cross-sectional area of the wall in the open sector. A mean value for H was calculated by measuring the area of the sector and using equation $(3.1)_2$.

Stress, Strain, and Compliance

The mean circumferential stress (σ_θ) and axial stress (σ_z) were then calculated as

$$\sigma_\theta = \frac{Pa}{h} \quad \text{and} \quad \sigma_z = \frac{f}{\pi(b^2 - a^2)} \tag{3.2}$$

where P is the transmural pressure, a is the current inner radius, b is the current outer radius, h is the current thickness, and $f = f_m + \pi a^2 P$ is the force applied to the vessel wall; f_m is the force measured by the force transducer. The mean circumferential and axial components of the Green Strain were calculated as

$$\bar{E}_{\theta\theta} = \frac{\overline{\lambda_\theta}^2 - 1}{2} \quad \text{and} \quad \bar{E}_{zz} = \frac{\bar{\lambda}^2 - 1}{2} \tag{3.3}$$

where the mean circumferential stretch was calculated as $\overline{\lambda_\theta} = r_{mid}/\rho_{mid}$, using mid-wall loaded and unloaded radii $r_{mid} = (a + b)/2$ and $\rho_{mid} = (\rho_o - \rho_i)/2$, respectively; here ρ_i and ρ_o are the unloaded inner and outer radii. Compliance is defined through the relation

$$C\,\Delta P = \Delta\ \varepsilon\ = \frac{\Delta r_m}{\bar{r}_m} \tag{3.4}$$

where C is compliance, Δr_m is the difference in the mid-wall radii measurements at two different pressures, $\bar{r}_m$ is the mid-wall radius at the mean pressure, ΔP is difference in the two pressures, and $\Delta\varepsilon$ is the local linearized cyclic strain experienced over ΔP. Physiological blood pressures were defined as 133/92mmHg (systole/diastole) for *fbln5*$^{+/+}$ mice and 151/94mmHg for *fbln5*$^{-/-}$ mice (164).

Multiphoton Microscopy

Freshly isolated vessels were imaged on an LSM 510 META inverted confocal microscope (Zeiss). The laser reached the sample through either a 40x/1.3NA or a 63x/1.4NA oil immersion objective (Zeiss). The META module of the microscope was configured as a 380-420nm bandpass filter to detect backwards scattering SHG signal from collagen (173). Elastin was detected using a 500-550nm bandpass filter with 488nm laser excitation (162). Confocal microscopy of embedded sections showed nearly identical morphology of elastin and collagen as samples stained with Verhoeff's and picro sirius red stains. Smooth muscle cells were visualized by staining the extracellular space with carboxyfluorescein (95). Imaris software (Bitplane) was used for 3D reconstruction of images.

Constitutive Modeling

Kinematics

We considered three configurations: a loaded configuration β_t, a traction-free (unloaded) configuration β_u, and a (nearly stress-free) reference configuration β_o; see Chuong and Fung (16). For inflation and extension of an axisymmetric tube, the

deformation gradient, right Cauchy Green strain, and Green strain tensors have components

$$[\mathbf{F}] = diag\,\{\lambda_r, \lambda_\theta, \lambda_z\}, \qquad [\mathbf{C}] = diag\,\{{\lambda_r}^2, {\lambda_\theta}^2, {\lambda_z}^2\},$$
$$[\mathbf{E}] = diag\,\{({\lambda_r}^2 - 1)/2, ({\lambda_\theta}^2 - 1)/2, ({\lambda_z}^2 - 1)/2\} \tag{3.5}$$

where

$$\lambda_r = \frac{\partial r}{\partial R}, \quad \lambda_\theta = \frac{\pi r}{\Theta_o R}, \quad \text{and} \quad \lambda_z = \lambda\Lambda \tag{3.6}$$

and Λ and λ are the axial stretches for the motions from β_o to β_u and from β_u to β_t, respectively and $\Theta_o = (\pi - \Phi_o)$ is the sector angle in β_o. If the material is assumed to be incompressible, det(**F**) = 1, the current radius may be related to the reference radius (in β_o) as

$$r = \sqrt{\frac{\Theta_o}{\pi\lambda\Lambda}(R^2 - R_i^2) + r_i^2} \quad \text{or} \quad r = \sqrt{r_o^2 - \frac{\Theta_o}{\pi\lambda\Lambda}(R_o^2 - R^2)} \tag{3.7}$$

where R_i and R_o inner or outer radii in β_o and r_i and r_o are inner and outer radii in β_t. Thus, given measured values for the reference configuration (R_i, R_o, the unloaded axial length L_z, and Θ_o) and the current configuration (r_o, r_i, and the loaded length l), the components of **F**, **C**, and **E** are easily calculated.

Equilibrium

Inflation and extension of a long, straight, axisymmetric, closed-ended tube in equilibrium requires that

$$P = \int_{r_i}^{r_o} (\hat{T}_{\theta\theta} - \hat{T}_{rr})\frac{dr}{r} \quad \text{and} \quad f_{\mathrm{m}} = \pi \int_{r_i}^{r_o} (2\hat{T}_{zz} - \hat{T}_{\theta\theta} - \hat{T}_{rr}) r dr\,; \tag{3.8}$$

where

$$\mathbf{T} = \widehat{\mathbf{T}} - p\mathbf{I} \quad \text{where} \quad \widehat{\mathbf{T}} = 2\mathbf{F}\left(\frac{\partial W}{\partial \mathbf{C}}\right)\mathbf{F}^T \tag{3.9}$$

$\widehat{\mathbf{T}}$ is the so-called 'extra' stress due to the deformation and W is the strain energy density function; see Humphrey (68).

Constitutive Equation

We used a four fiber family proposed by Baek et al. (4), which is a simple extension of the model proposed by Holzapfel et al. (63) and Spencer (132), with strain energy function

$$W = \frac{b}{2}(I_1 - 3) + \sum_{k=1,2,3,4} \frac{b_1^k}{2b_2^k}\left\{\exp\left[b_2^k\left((\lambda^k)^2 - 1\right)^2\right] - 1\right\} \tag{3.10}$$

where b, b_1^k, and b_2^k are material parameters with k denoting a fiber family, $I_1 = \text{tr}(\mathbf{C}) = C_{rr} + C_{\theta\theta} + C_{zz}$ is the first invariant of $\mathbf{C}$, $\lambda^k = \sqrt{\mathbf{M}^k \cdot \mathbf{C}\mathbf{M}^k}$ is the stretch of the k^{th} fiber family, $\mathbf{M}^k = \sin(\alpha^k)\mathbf{e}_\theta + \cos(\alpha^k)\mathbf{e}_z$ is the unit vector along the k^{th} fiber direction in the reference configuration, and α^k is the associated angle between the axial and fiber directions. In general, $(\lambda^k)^2 = C_{\theta\theta}\sin^2(\alpha^k) + 2C_{\theta z}\sin(\alpha^k)\cos(\alpha^k) + C_{zz}\cos^2(\alpha^k)$, but $C_{\theta z} = 0$ for inflation and extension tests, given material symmetry. Under compression, the fiber-families do not contribute to the mechanical response in an exponential fashion, as they do in tension. Thus, when $\lambda^k < 1$, we set $b_1^k = 0$; therefore, we model the vessel under compression as a neo-Hookean material. Here, we consider four fiber families with $\alpha^1 = 90°$ (circumferential), $\alpha^2 = 0°$ (axial), and $\alpha^3 = -\alpha^4 = \alpha$ (diagonal) which is left as a variable to be determined along with the seven material

parameters (with $b_1^3 = b_1^4$ and $b_2^3 = b_2^4$ for the diagonal fibers to ensure material symmetry) via non-linear regression.

Parameter Estimation

Equations (3.8) were used to calculate *P* and *f* based on measured values of outer diameter, axial length, unloaded radius, unloaded length and wall thickness. We employ equation (3.6), with equation (3.7), and specify the *in vivo* configuration and transmural strains in this configuration to determine $\mathbf{F}$ and $\mathbf{C}$. Material parameters were identified via nonlinear regression by minimizing the error function

$$error = \left\{ \sum_{i=1}^{N} \left(\frac{P_{meas}(i) - P_{model}(i)}{\bar{P}} \right)^2 + \sum_{i=1}^{N} \left(\frac{f_{meas}(i) - f_{model}(i)}{\bar{f}} \right) \right\}^2 \tag{3.11}$$

where $P_{meas}(i)$ and $f_{meas}(i)$ are measured values and $P_{model}(i)$ and $f_{model}(i)$ are predicted values of pressure and axial force for data point *i* and $\bar{P}$ and $\bar{f}$ are mean values of pressure and force over all data points. Thus, equation (3.11) quantifies the difference between experimental data and modeling predictions. Calculations were performed in MATLAB 7.1 using the *lsqnonlin* subroutine.

Statistical analysis

Mean values were compared using unpaired, two-tailed t-tests, with significance taken at $p<0.05$. Welch's correction was used when variances between groups were unequal.

Rcsults

Mechanical response of fbln5-/- arteries and controls

Pressure-diameter tests of *fbln5*$^{+/+}$ mice and *fbln5*$^{-/-}$ mice revealed distinct regimes over lower pressure and higher pressure ranges characteristic of rodent large arteries (Figure 3.1a). Not all curves reached 180 mmHg because tests were stopped when the axial force reached the maximum limit or when the axial force became negative. Force measurements taken during *P-d* tests indicated that at lower axial stretch ratios, axial force decreases with increased pressure while at higher axial stretch ratios, axial force increases with increased pressure (Figure 3.1b). Although the range of axial stretch ratios used for testing was different for the *fbln5*$^{-/-}$ and *fbln5*$^{+/+}$ groups, there were stretch ratios that overlapped both groups. Namely, at λ =1.40, it is clear that the mechanical responses of the two types of vessels are different (Figure 3.1b). For each vessel tested, there was an axial stretch ratio for which the force remains nearly constant with increased pressure, indicating the *in vivo* axial stretch ratio (24, 140). Mid-wall radii were calculated at the *in vivo* axial stretch ratio revealing significant differences in geometry at pressures greater than or equal to 70 mmHg (Figure 3.2a and Table 3.1). In addition, the axial force was significantly different between groups when measured at the *in vivo* axial stretch ratio (Figure 3.2b). Given the significantly lower *in vivo* axial stretch of the *fbln5*$^{-/-}$ vessels, *P-d* tests for *fbln5*$^{-/-}$ vessels were performed at lower axial stretch ratios than *fbln5*$^{+/+}$ vessels. Results from axial force-length tests (Figure 3.3) revealed a cross-over point which represents the *in vivo* axial stretch ratio (147); the mean *in vivo* axial stretch ratio of *fbln5*$^{-/-}$ arteries was λ =1.40, compared to a mean *in vivo* axial stretch ratio of λ = 1.64 in *fbln5*$^{+/+}$ arteries (Table 3.1). The *in vivo* axial stretch ratios as determined from $f-\ell$ tests were similar to the axial stretch ratio determined from *P-d* tests.

(a) (b)

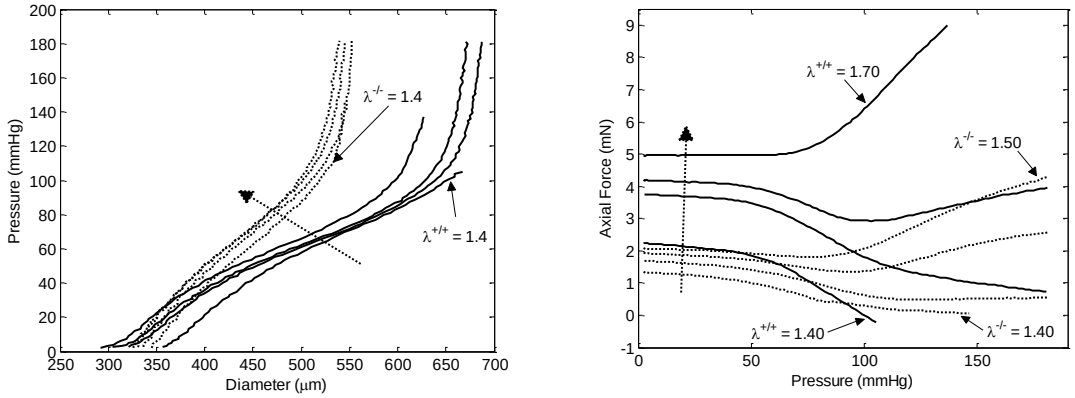

Figure 3.1: Representative plots of pressure-diameter (a) and pressure-force (b) results for *fbln5*$^{+/+}$ (solid lines) and *fbln5*$^{-/-}$ (dotted lines) arteries. Curves for *fbln5*$^{+/+}$ plot indicate axial stretch ratios of λ = 1.40, λ = 1.45, λ = 1.48, and λ = 1.50, while curves for *fbln5*$^{-/-}$ plot indicate axial stretch ratios of λ = 1.40, λ = 1.60, λ = 1.65, and λ = 1.70. Dotted arrow indicates direction of increasing axial stretch ratios. The exponentially stiffening portion of the mechanical response of *P-d* curves occurs at smaller diameters in *fbln5*-/- arteries.

(a) (b)

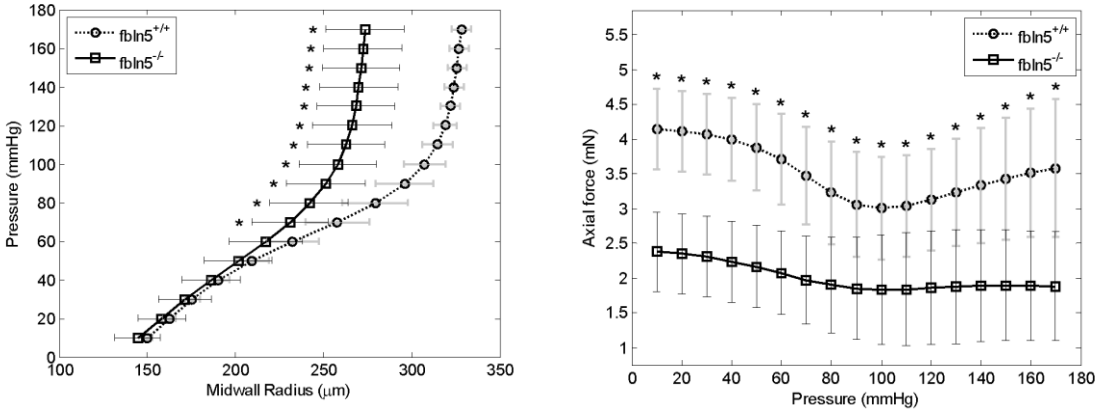

Figure 3.2: Mean pressure-mid-wall radii (a) and pressure-force (b) plots for *fbln5*$^{+/+}$ (circles) and *fbln5*$^{-/-}$ (squares) arteries. Data were collected at the *in vivo* axial stretch ratio and indicate that *fbln5*$^{-/-}$ vessels had smaller circumferential dimensions. Asterisks indicate $p<0.05$; error bars indicate standard deviation.

Table 3.1 Animal age and weight and vessel geometry, contractile response, and mechanical metrics for *fbln5*$^{+/+}$ and *fbln5*$^{-/-}$ mice; Values are means (SD), * indicates $p<0.05$ between fbln5+/+ and fbln5-/- vessels, # indicates $p<0.05$ within groups

	fbln5$^{+/+}$ (n=6)	*fbln5*$^{-/-}$ (n=7)
Age (weeks)	13.42 (0.29)	12.69 (1.74)
Body weight (g)	28.93 (0.77)	24.04 (1.00)*
Opening angle	91.81 (34.34)	28.02 (20.03)*
Unloaded dimensions (μm)		
Inner diameter	248.41 (33.92)	201.9 (98.95)
Outer diameter	402.67 (21.02)	417.43 (22.88)
Wall thickness	77.13 (15.30)	107.77 (41.59)
In vivo dimensions (μm)		
Inner diameter	603.26 (25.21)	491.78 (57.21)*
Outer diameter	651.86 (23.03)	576.95 (42.77)*
Wall thickness	24.30 (4.51)	42.58 (11.11)*
In vivo axial stretch ratio	1.64 (0.03)	1.4 (0.07)*
Response to vasoagonists (Normalized diameter)		
Norepinephrine	0.86 (0.08)#	0.94 (0.04)#
Carbachol	0.89 (0.08)	0.96 (0.03)
Sodium nitroprusside	1.00 (0.03)#	1.00 (0.03)#
Physiologic compliance (MPa^{-1})	14.00 (7.44)	8.51 (3.62)
Linearized cyclic strain (%)	7.76 (4.13)	6.46 (2.75)
Mean in vivo stresses (kPa)		
Circumferential	194.44 (37.75)	101.23 (32.42)*
Axial	158.67 (29.22)	74.39 (27.88)*

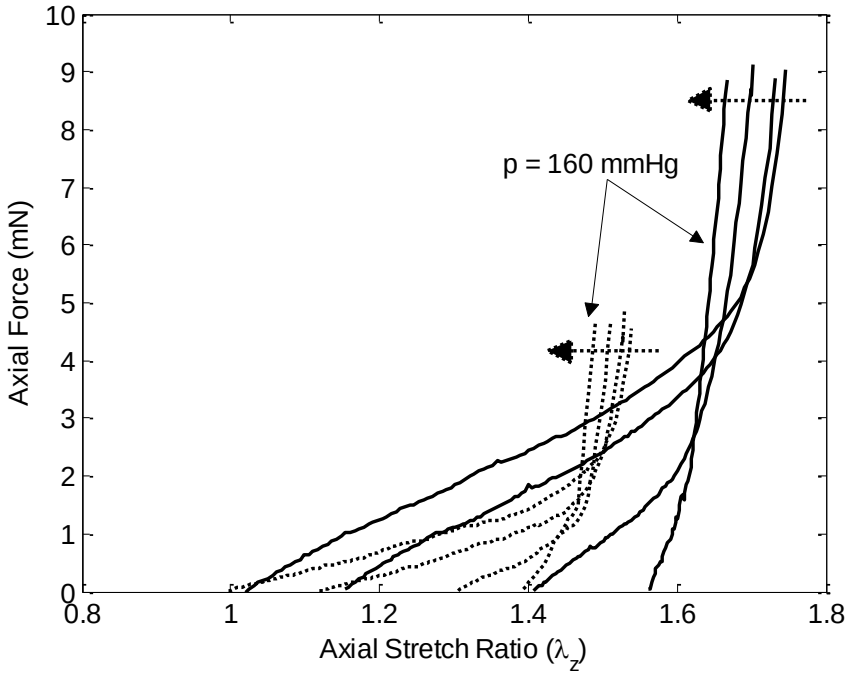

Figure 3.3: Representative plots of axial force-stretch results for *fbln5*$^{+/+}$ (solid lines) and *fbln5*$^{-/-}$ (dotted lines) arteries. Axial force-stretch tests were conducted at pressures of P = 0, P = 60, P = 100, and P = 160 mmHg. Dotted arrows indicate direction of increasing pressure. The crossover points represent *in vivo* axial stretch ratios; and the data suggests that *fbln5*$^{-/-}$ vessels have a lower *in vivo* axial stretch ratio

Stress, Strain and Compliance.

Since the pressure-diameter and axial force-length responses depend on both material properties and geometry, it is difficult to quantify differences in the material properties between different vessels from *P-d* and $f - \ell$ plots. Stress-strain plots, however, only depend on material properties; thus, differences in the stress-strain response indicate differences in the material properties. While large segments of the mean stress-strain plots in both circumferential and axial directions overlap (Figure 3.4), calculations based on *in vivo* axial stretch and mean blood pressures reveal significant differences in both *in vivo* axial and circumferential stresses (Table 3.1). Mean circumferential and axial (Cauchy) stress versus mid-wall Green strain reveal significant

differences in the material response between *fbln5*$^{+/+}$ and *fbln5*$^{-/-}$ vessels (Figure 3.4a, b). Namely, the exponentially stiffening portion of the stress strain plots occurs at lower strains for *fbln5*$^{-/-}$ vessels. The overall compliance, between systolic and diastolic pressures, of the *fbln5*$^{-/-}$ carotid arteries was not statistically different than *fbln5*$^{+/+}$ carotid arteries. The *in vivo* local linearized cyclic strain $\Delta\varepsilon$ over the cardiac cycle was also not statistically different across groups (Table 3.1). The local compliance, calculated at 10 mmHg intervals, was also not significantly different at the overlapping physiological pressures; however, compliance was different at 50, 60, 70, 80 and 150 mmHg. (Figure 3.5).

(a) (b)

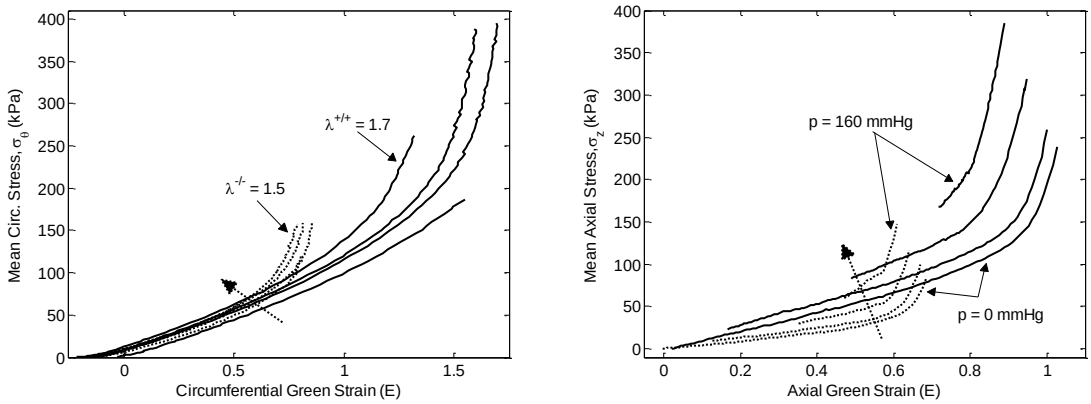

Figure 3.4: Representative plots of mean circumferential stress-strain (a) and mean axial stress-strain (b) results for *fbln5*$^{+/+}$ (solid lines) and *fbln5*$^{-/-}$ (dotted lines) arteries. For the circumferential stress-strain plot, curves for *fbln5*$^{+/+}$ plot indicate axial stretch ratios of λ = 1.40, λ = 1.45, λ = 1.48, and λ = 1.50, while curves for *fbln5*$^{-/-}$ plot indicate axial stretch ratios of λ = 1.40, λ = 1.60, λ = 1.65, and λ = 1.70. For the axial stress-strain plot, curves reflect tests conducted at pressures of P = 0, P = 60, P = 100, and P = 160 mmHg. Dotted arrows reflect the direction of increasing axial-stretch ratio or direction of increasing pressure. The exponentially stiffening portion of the curves occurs at lower strains in the *fbln5*$^{-/-}$ artery.

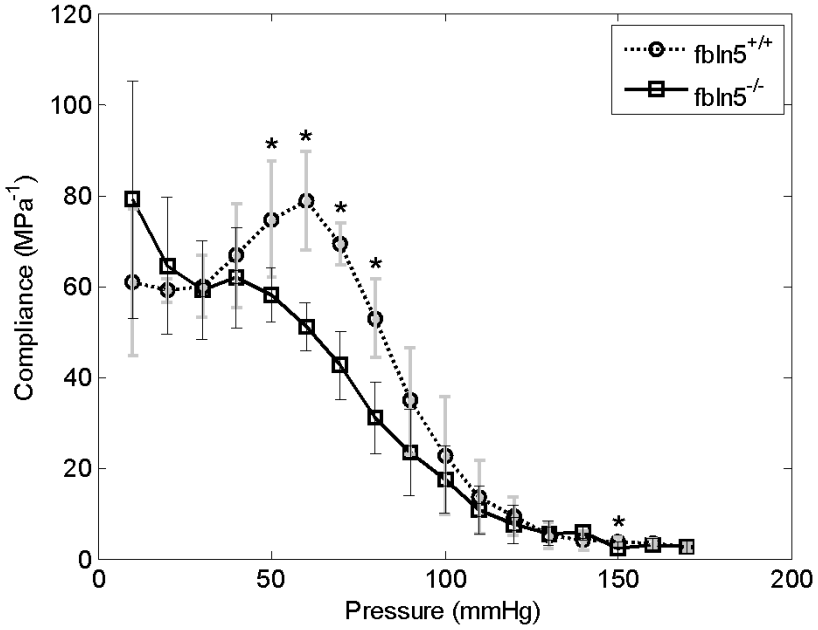

Figure 3.5: Compliance calculated at 10 mmHg intervals at the *in vivo* axial stretch ratio. At overlapping physiological pressures, there were no significant differences in compliance. Asterisks indicate $p<0.05$; errors bars indicate one standard deviation.

Stress Free, unloaded and loaded configuration

Excised *fbln5*$^{+/+}$ carotid arteries exhibited slight bending upon excision compared to the marked tortuosity of *fbln5*$^{-/-}$ arteries (Figure 3.6). Opening angles of sectors cut from *fbln5*$^{-/-}$ arteries were statistically greater than angles of *fbln5*$^{+/+}$ arteries (Figure 3.7 and Table 3.1), and there was also greater variability across samples in opening angle measurements from *fbln5*$^{-/-}$ arteries. Inner diameter, outer diameter, and wall thickness were not statistically different in unloaded, traction-free configurations of *fbln5*$^{+/+}$ and *fbln5*$^{-/-}$ arteries. Under *physiological* loading conditions, *fbln5*$^{-/-}$ vessel had significantly smaller inner and outer diameters and larger wall thicknesses than the *fbln5*$^{+/+}$ vessel (Table 3.1).

(a) (b)

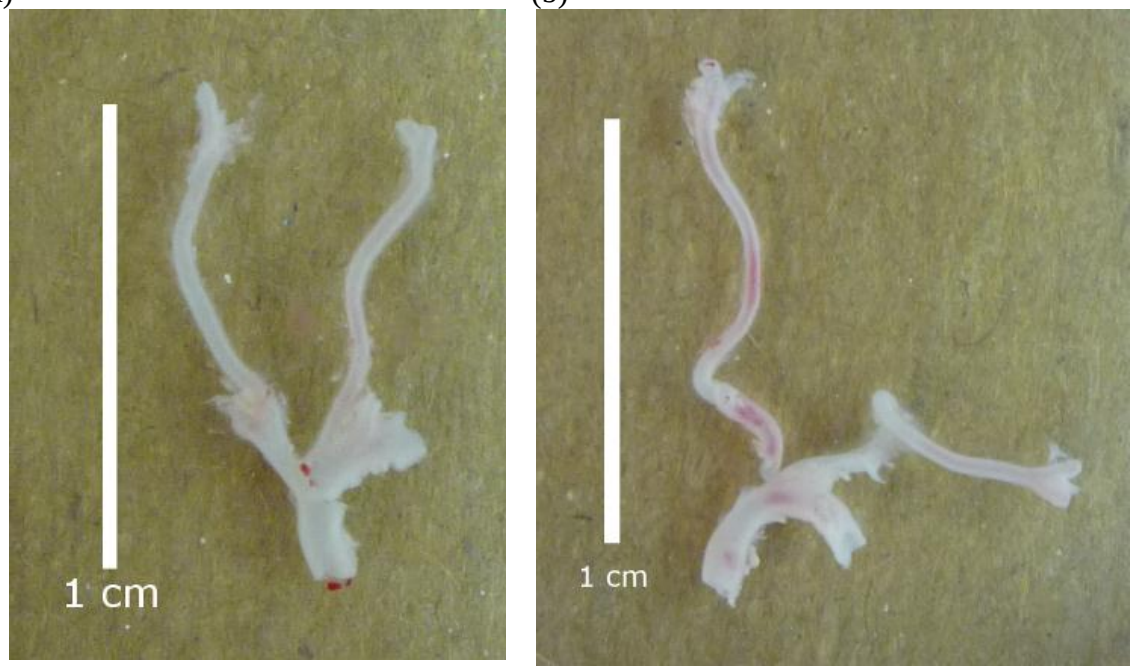

Figure 3.6: Representative images of excised arteries from *fbln5*$^{+/+}$ (a) and *fbln5*$^{-/-}$ (b) vessels. Vessels in the unloaded state from KO mice exhibit significant tortuosity compared with slight bending observed in WT vessels

(a) (b)

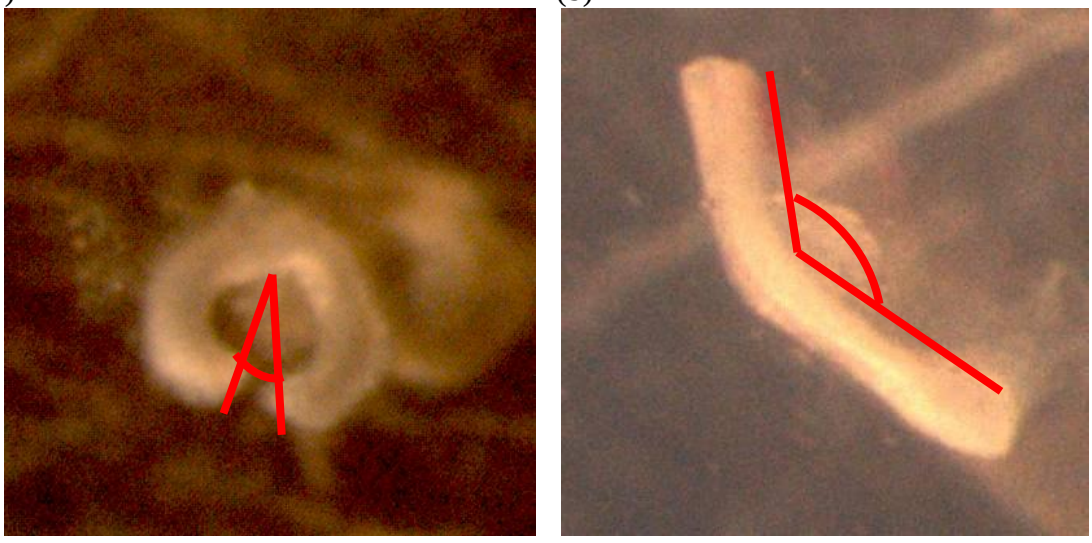

Figure 3.7: Representative opening angle sectors from *fbln5*$^{+/+}$ (a) and *fbln5*$^{-/-}$ (b) arteries

Functional response

Following 'basal' biomechanical testing, smooth muscle and endothelial cell function was confirmed by pharmacologically induced constriction and dilation. Both *fbln5*$^{-/-}$ and *fbln5*$^{+/+}$ vessels decreased in diameter in response vasoconstrictors while relaxing to near basal levels of outer diameter in response to vasodilators (Table 3.1). Both WT and KO vessels exhibited significant differences in normalized diameter at maximal contraction and normalized diameter at maximal relaxation.

Microstructural Organization

In the traction-free configuration, elastin from the *fbln5*$^{+/+}$ artery appeared undulated with a distinct internal elastic lamina while elastin in the *fbln5*$^{-/-}$ artery appears disorganized with no distinct internal lamina (Figure 3.8). Under *in vivo* conditions, distinct layers of elastin are visible in the *fbln5*$^{+/+}$ artery while the *fbln5*$^{-/-}$ artery lacks noticeable lamellar units (Figure 3.8). Collagen in the traction free configuration appears to exist with varying degrees of undulation in the *fbln5*$^{-/-}$ and the *fbln5*$^{+/+}$ arteries (Figure 3.9). Under identical conditions of axial stretch and transmural pressure, collagen fibers in *fbln5*$^{-/-}$ arteries appear to be straightened and engaged while collagen fibers in *fbln5*$^{+/+}$ arteries appear undulated (Figure 3.9). Under *in vivo* conditions, individual SMC show similar morphology in both *fbln5*$^{-/-}$ and the *fbln5*$^{+/+}$ arteries; however, distinct lamellar units were visible in the *fbln5*$^{+/+}$ arteries (Figure 3.10).

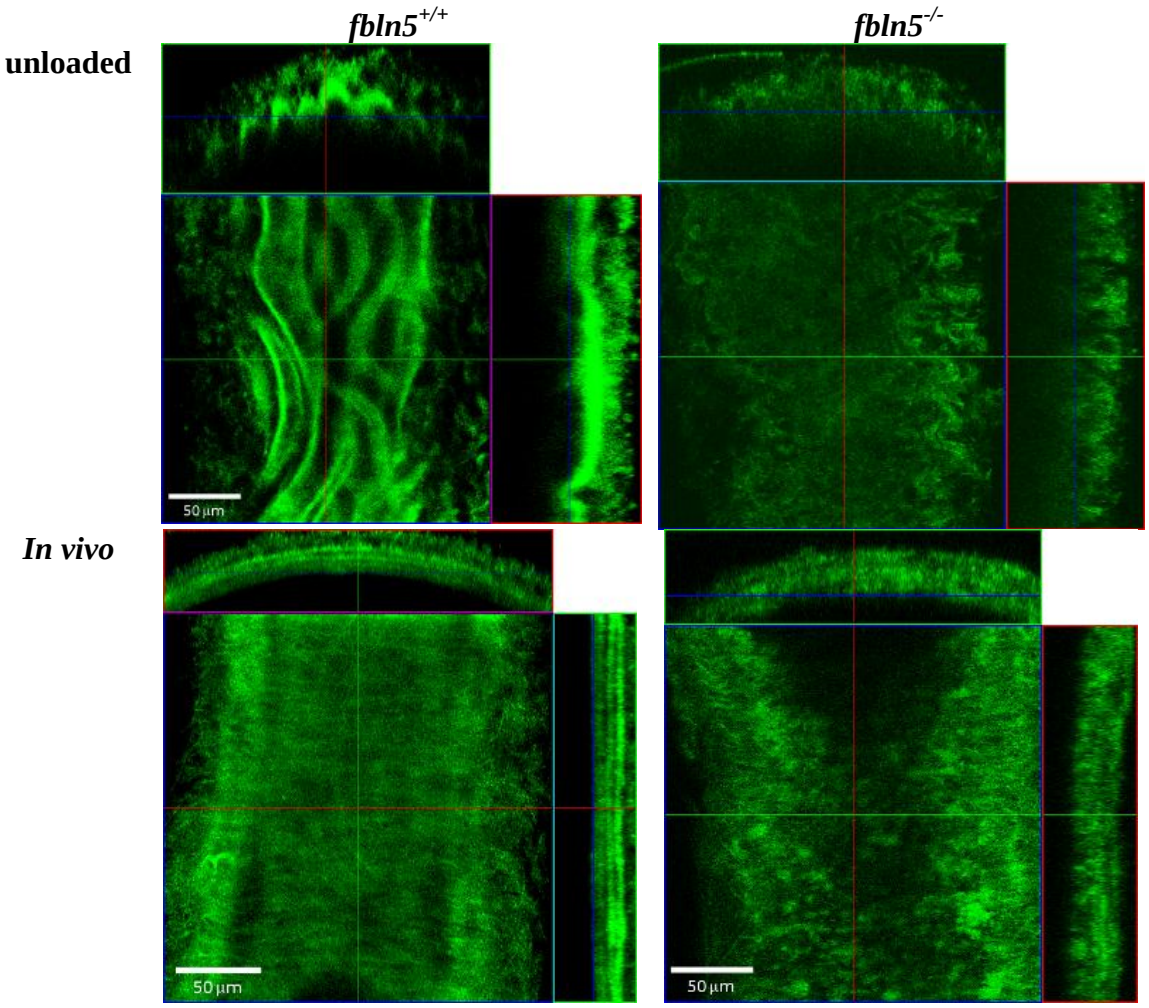

Figure 3.8: The undulated internal elastic lamina is clearly visible in the traction-free configuration of the *fbln5*$^{+/+}$ artery while elastin is more disorganized in the *fbln5*$^{-/-}$ artery. When pressurized to *in vivo* conditions, elastin organized into lamellar units is visible in the *fbln5*$^{+/+}$ artery while in the *fbln5*$^{-/-}$ artery elastin remains disorganized. Panels i, ii, and iii show cross, *en face* and longitudinal sections, respectively.

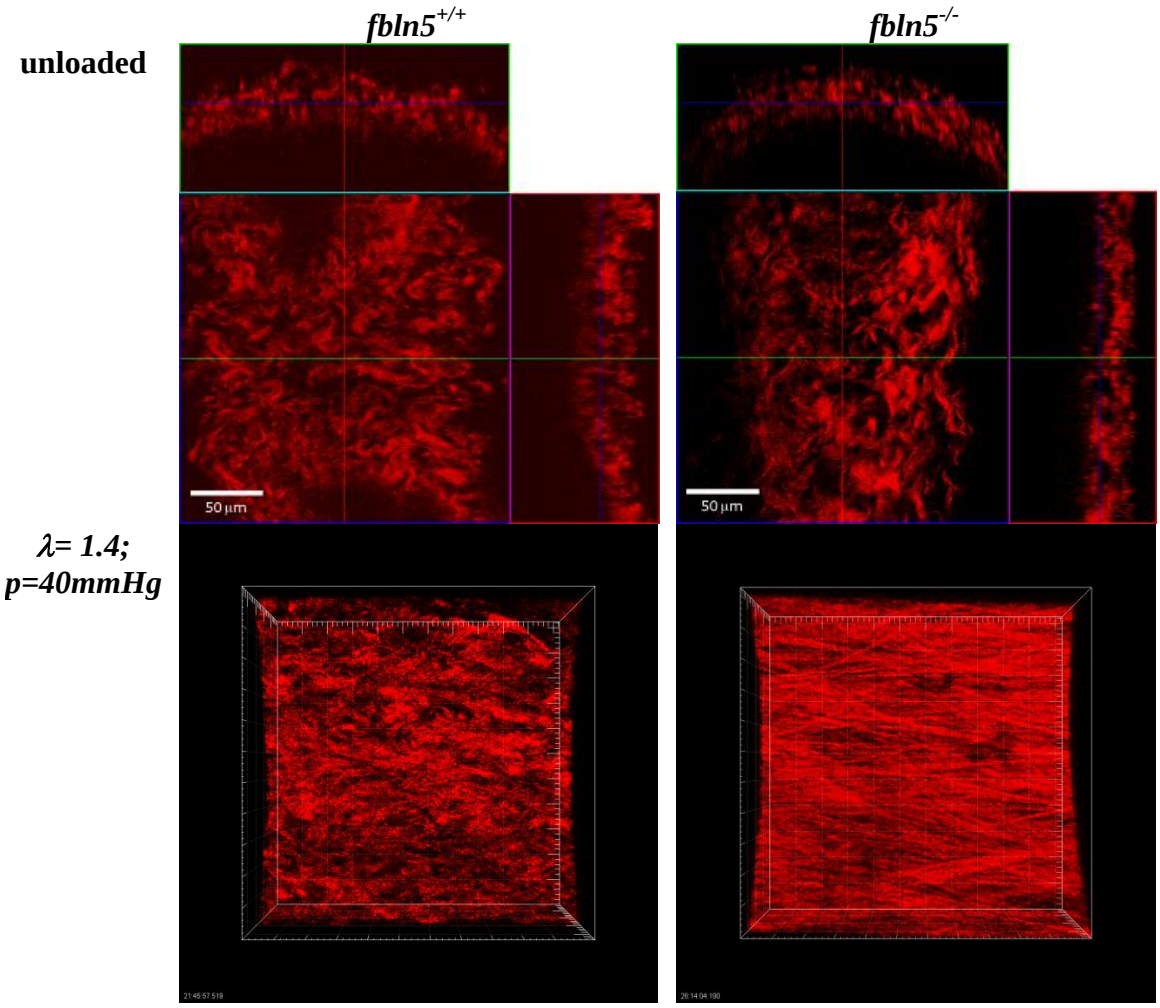

Figure 3.9: In the traction-free state, collagen fibers in the *fbln5*$^{+/+}$ artery and the *fbln5*$^{-/-}$ artery have different degrees of undulation. Panels i, ii, and iii show cross, *en face* and longitudinal sections, respectively. Collagen was imaged at an axial stretch of λ = 1.4 and transmural pressure of P = 40mmHg for both KO and WT arteries; images were stacked to generate a 3D reconstruction. Collagen fibers from the *fbln5*$^{-/-}$ vessel appear straightened while collagen fibers from the *fbln5*$^{+/+}$ vessel appears undulated, indicating that collagen fibers in *fbln5*$^{-/-}$ vessels become engaged at a lower axial stretch ratio.

(a) (b)

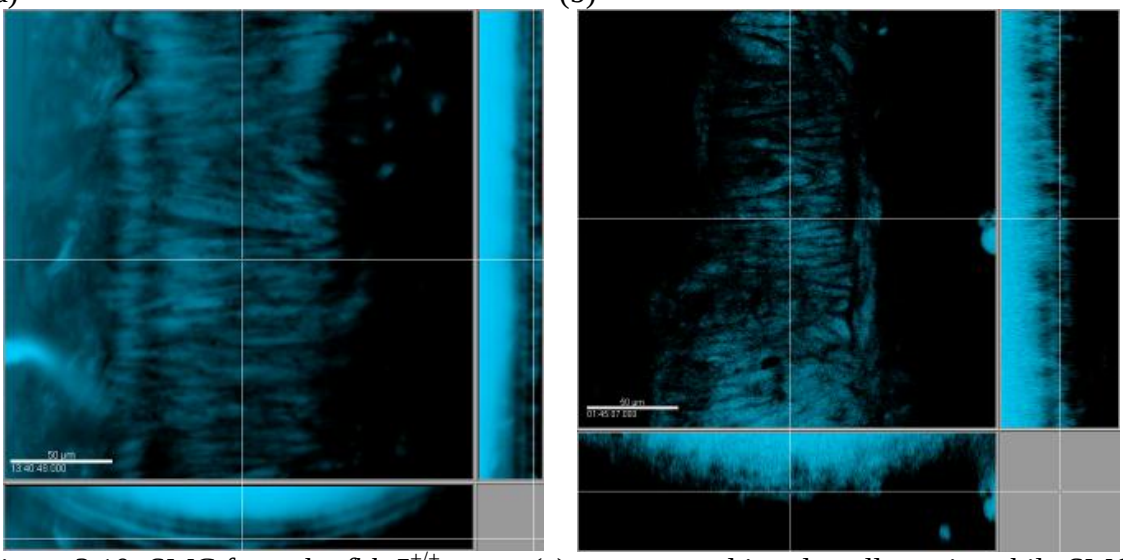

Figure 3.10: SMC from the *fbln5*$^{+/+}$ artery (a) are arranged into lamellar units while SMC from the *fbln5*$^{-/-}$ artery (b) lack lamellar structure. Panels i, ii, and iii show cross, *en face* and longitudinal sections, respectively.

Parameter Estimation

A four fiber model was able to capture the full range of mechanical behaviors in both *fbln5*$^{-/-}$ and the *fbln5*$^{+/+}$ arteries (Figure 3.11). The lower and upper limits of the parameters were prescribed as b and $b_1^k \in [0,10^5]$, $b_2^k \in [10^{-4},10^5]$, and $\alpha \in [0^o,90^o]$. The upper bounds were selected to encompass the full working range of individual parameters and the non-zero lower bound for b_2^k was selected to prevent the algorithm from searching for values close to zero. Final parameter values were insensitive to initial guesses. The mean values of *error* = 0.058 and *error* = 0.042 indicate reasonably good fits to experimental data; error values on (Table 3.2) reflect the error calculated from equation (3.11) normalized to the total number of data points for each vessel. A significant increase in b_2^2 and b_2^3, was seen for the *fbln5*$^{-/-}$ groups (Table 3.2); these are the parameters in the exponential terms for the axially and diagonally oriented fiber

families equation (3.10). Note that the elastic modulus term, *b*, was lower in *fbln5*$^{-/-}$ vessels; however, this difference was not statistically significant.

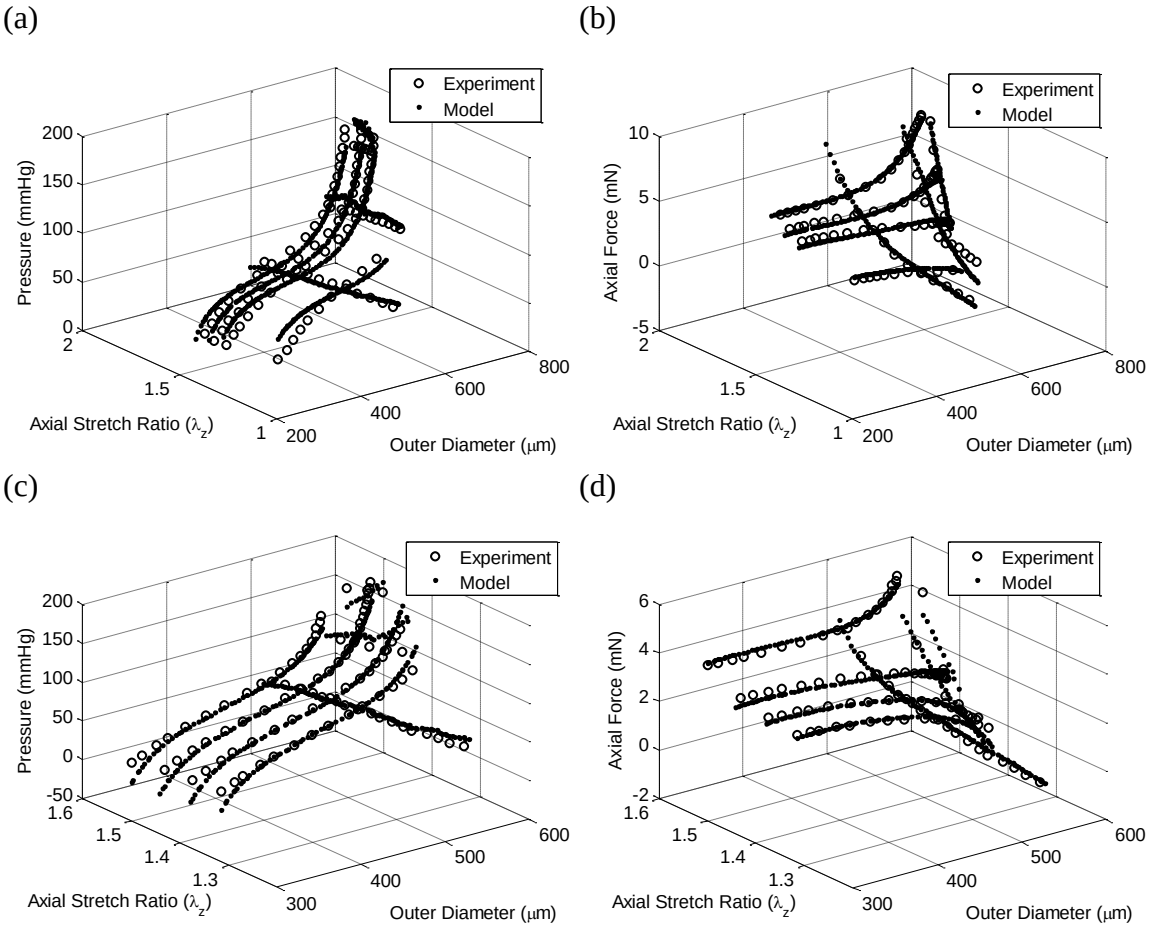

Figure 3.11: Illustrative plots of pressure and axial force versus diameter and axial stretch for model predictions (●) and experimentally measured (○) for *fbln5*$^{+/+}$ (a) and *fbln5*$^{-/-}$ (b) arteries. At lower diameters, these two cases show the model overestimating pressure for the *fbln5*$^{+/+}$ artery while underestimating pressure for the *fbln5*$^{-/-}$ artery.

Table 3.2: Material parameters for *fbln5*$^{+/+}$ and *fbln5*$^{-/-}$ carotid arteries obtained for a 4-fiber constitutive model; Asterisks indicate that the parameter is statistically different between KO and WT mice (p<0.05)

	b (kPa)	b_1^1 (kPa)	b_2^1	b_1^2 (kPa)	b_2^2	b_1^3 (kPa)	b_2^3	α
fbln5$^{+/+}$								
1	26.295	0.036	0.709	0.141	1.201	0.576	0.835	43.075
2	26.905	3.569	0.129	0.611	0.768	0.803	0.885	32.934
3	17.004	0.431	0.216	0.418	0.783	0.246	0.850	32.041
4	40.516	0.974	0.278	0.105	0.932	0.012	1.562	41.237
5	31.285	0.385	0.290	0.333	1.004	0.370	0.861	33.567
6	13.805	3.153	0.044	17.744	0.000	0.274	0.726	30.704
Mean	25.968	1.425	0.278	3.225	0.781 *	0.380	0.953 *	35.593
SD	9.687	1.535	0.231	7.115	0.415	0.276	0.303	5.206
fbln5$^{-/-}$								
1	26.735	5.077	0.859	0.000	5.537	0.050	3.426	36.128
2	24.002	2.940	0.633	0.610	2.659	1.080	2.026	40.749
3	26.699	0.963	0.625	0.032	5.305	0.368	2.688	34.875
4	0.189	0.727	0.068	4.876	1.078	2.682	0.399	36.51
5	0.133	2.313	0.023	9.448	0.000	1.688	0.717	25.94
6	11.716	0.992	0.353	0.990	5.638	0.447	3.450	29.886
7	19.889	6.527	0.306	0.000	9.086	0.081	3.139	34.379
Mean	15.623	2.791	0.410	2.279	4.186 *	0.914	2.264 *	34.067
SD	11.747	2.246	0.310	3.606	3.128	0.975	1.267	4.816

Values are means (SD), * indicates P <0.05

Discussion

Since the classic paper by Roach and Burton, it is thought that functional elastic fibers in large arteries mediate the shape of the pressure-diameter curves at low pressures while collagen mediates this behavior at higher pressures (118). Genetically altered mouse models that suppress expression of tropoelastin and microfibrillar proteins (e.g., fibrillins and fibulins) provide a unique platform to study the role of functional elastic fibers in the mechanical response of arteries (29, 151). In this study, we quantified the mechanical properties of *fbln5*$^{-/-}$ common carotid arteries, which lack functional elastic laminae, and the *fbln5*$^{+/+}$ arteries, which have normal elastic laminae. We performed biaxial mechanical tests and multiphoton (confocal) microscopy imaging on isolated carotid artery segments from *fbln5*$^{+/+}$ and *fbln5*$^{-/-}$ mice. Biaxial tests revealed that arteries

from *fbln5*$^{-/-}$ mice were circumferentially and axially stiffer with a lower *in vivo* axial stretch than arteries from *fbln5*$^{+/+}$ mice. Although vascular stiffness was elevated in *fbln5*$^{-/-}$ vessels, since the *in vivo* pulse pressure is also higher in *fbln5*$^{-/-}$ vessels, the cyclic strain in *fbln5*$^{-/-}$ and *fbln5*$^{+/+}$ carotid arteries were not statistically different. This result suggests that, although significant microstructural differences exist between *fbln5*$^{-/-}$ and *fbln5*$^{+/+}$ carotid arteries, growth and remodeling mechanisms that occur throughout development have altered the geometry and microstructural organization to achieve similar values of cyclic strain. Confocal microscopy images reveal significant differences in the structure of elastin, and the organization of SMC of *fbln5*$^{-/-}$ carotid arteries. In contrast to *fbln5*$^{+/+}$ carotid arteries, *fbln5*$^{-/-}$ carotid arteries lacked organized elastic lamellae and had collagen fibers that engaged at lower axial stretch ratios. These differences in microstructure were coincident with elevated vascular stiffness and a lower *in vivo* axial stretch ratio in *fbln5*$^{-/-}$ vessels. Constitutive modeling revealed that the mechanical behavior of *fbln5*$^{+/+}$ and *fbln5*$^{-/-}$ vessels could be described well with the four fiber-family model of Baek et al., 2007 (4).

These microstructural differences manifest in significant differences in the biaxial biomechanical behavior across these groups. In particular, loss of functional elastic laminae results in vessels with an 15% reduction in *in vivo* mid-wall diameter, a 75% increase *in vivo* wall thickness, a 15% reduction in *in vivo* axial stretch, and a ~50% reduction in *in vivo* stresses. It appears that the presence of functional elastic laminae in control vessels serve to increase the *in vivo* axial stretch ratio and prevent vessel tortuosity. In *fbln5*$^{-/-}$ arteries, the exponential stiffening region of the stress-strain plot occurs at lower axial and circumferential strains. This phenomenon can be further

illustrated by images of collagen from KO and WT arteries that are pressurized and stretch to identical loading conditions. Collagen fibers seen in *fbln5*$^{-/-}$ carotid arteries at an axial stretch of λ = 1.4 and pressure of P = 40 mmHg appear straightened while collagen fibers from *fbln5*$^{+/+}$ arteries remain undulated (Figure 3.9).

Decreases in *in vivo* axial stretch have been observed in mice deficient in elastin (*eln*), fibrillin-1 (*fbn1*), dystrophin (*mdx*), and sarcoglycan-δ (*sgcd*) (28, 29, 151). In addition to a lower *in vivo* axial stretch ratio and reduced elastin content , carotid arteries of elastin haploinsufficent mice also exhibit arterial tortuosity, and lower outer diameters.. Despite these differences, and in contrast to our *fbln5*$^{-/-}$ data, there were no significant differences in circumferential and axial stress-stretch relationships when held near the *in vivo* stretch and no differences in opening angles between the elastin haploinsufficient and control carotid arteries or abdominal aorta (151). For a mouse model of Marfan's Syndrome in which fibrillin-1 is reduced to 15-25% of normal levels (*fbn1*$^{R/R}$), carotid arteries exhibit similar *in vivo* outer diameters, but 5% reduction in *in vivo* axial stretches compared to control vessels; namely, the axial stretch in *fbn1*$^{R/R}$ was 1.63±0.02, compared to 1.71±0.02 in wild-type controls. Again, in contrast to our data, there are no significant differences in the circumferential mechanical behavior at *in vivo* axial stretches between the *fbn1*$^{R/R}$ and control carotid arteries. Force length tests, however, suggest differences in axial stress between *fbn1*$^{R/R}$ arteries and WT controls at pressures from P = 60mmHg to

P = 100mmHg and at axial stretches above λ = 1.64. In mouse models of muscular dystrophy pressure-diameter relationships near the *in vivo* axial stretch ratio are not statistically different (28). Thus, it appears that the presence of some functional

elastic fibers, even in lowered quantities, is sufficient to allow large arteries to adapt to achieve normal circumferential *in vivo* mechanical behavior. Arterial tortuosity was also not noted in studies of mice deficient in *fbln1*, *mdx* and *sgcd* suggesting that the decrease in the production of functional elastic fibers is the cause of tortuosity (28, 29). Biomechanical properties of elastin KO mice ($Eln^{-/-}$) show significant geometric and mechanical differences; however, these mice die within 72 hours of birth (150). Our study, as well as others, highlights the need to further investigate the axial mechanical behavior of arteries.

To quantify the local mechano-biological response of cells to their local mechanical environment, it is necessary to accurately predict their local mechanical environment; this requires a constitutive model with adequate predictive capability. Given that growth and remodeling are controlled through turnover and remodeling of key structural constituents, we submit that such a constitutive model should be structurally motivated; thus, we employed a fiber-family model. Parameter estimation results suggest significant differences in the material properties of $fbln5^{-/-}$ arteries. Each artery was modeled as anisotropic axial, circumferential and diagonal fibers embedded in an isotropic matrix. The isotropic portion of the vessel is associated with the parameter, b, while the anisotropic fibers are associated with b_1^k and b_2^k. Parameter estimation studies indicated increases in exponential terms, b_2^2 and b_2^3, for $fbln5^{-/-}$ arteries. These two parameters suggest differences in the mechanical behavior of axial and diagonal portions of the model. Because this constitutive relation does not account for mass fractions and altered crosslinking of constituents, differences in the structural configuration of constituents could have produced the changes observed in these parameters. A few

parameters were force to zero highlighting the relative degree of exponential behavior of that fiber family. A fiber family with a b_2^k term near zero or very much smaller than the b_1^k term would exhibit high degree of exponentially stiffening behavior. There was also a large degree in variability in some of the parameters such as the case of b for fbln5$^{-/-}$ mice and b_1^2 for both groups. Large variations in parameters describing experiments that exhibit similar mechanical behaviors highlights the sensitivity of parameters to small perturbations in biaxial test data and is characteristic of constitutive relations with exponential terms (37, 62). Results from parameter estimation studies illustrate the need for detailed investigation of the structure of arteries as well the need for constitutive relations that account for the structural components of the arterial wall (56).

Mechanically-induced vascular remodeling occurs as cells sense and adapt their local mechanical environment and plays a key role in many physiological and pathophysiological processes, as well as in the outcomes of many clinical interventions; examples include arterial stiffening with age, development of aneurysms, hypertension, atherosclerosis, and restenosis of vascular grafts. These adaptations (or maladaptations) are controlled largely by delicate balances (or imbalances) in the production, removal, and reorganization of structural proteins.

Whereas much attention has been paid to the role of wall shear stress and circumferential (hoop) stress in vascular remodeling and CVD, the role of axial stress has been largely overlooked. Findings suggest, however, that altered axial stretch (or stress) induces remodeling at rates that are ‘unprecedented’ compared to that of pressure and flow (73). We submit that cells sense and respond to their local mechanical environment and grow and remodel to restore their local mechanical environment to a ‘desired’ state.

Many clinical observations highlight the importance of axial remodeling in the vasculature; marked tortuosity in AAAs, mammary artery by-pass grafts, and reduced axial strain in hypertension and aging are but a few examples. Circumferential expansion, wall thinning and axial lengthening of AAAs is coincident with a progressive loss of elastin and smooth muscle and a decrease in glycosaminoglycans. Indeed, the level of aortic tortuousity is among the greatest indicators of risk for AAA rupture (32). These observations suggest that elastic fibers endow arteries with their *in vivo* axial strain and the loss of functional elastic fibers (which occurs in AAAs, hypertension, and aging) may be associated with impaired axial remodeling and development of tortuousity.

The lack of differences in compliance at pressures within the physiological range as well as differences in physiological geometry suggests that compliance (or cyclic strain) may be a primary target for adaptations in vascular growth and remodeling. *In vivo* mean stresses in the axial and circumferential directions were not restored suggesting that stress, while a target for growth and remodeling in cases of altered loading conditions (72, 76, 99), may not be the primary target in development and maturation. Indeed, these results suggest that cyclic strain is restored during maturation, with *in vivo* stresses, perhaps being a secondary target for growth and remodeling. This speculation, however, warrants further investigation as other reports in the literature may suggest otherwise (99).

In summary, biaxial mechanical tests have revealed distinct differences in the material properties of the *fbln5*$^{+/+}$ and *fbln5*$^{-/-}$ arteries while confocal and multi-photon imaging have revealed structural differences in elastin, collagen and smooth muscle cell organization between *fbln5*$^{+/+}$ and *fbln5*$^{-/-}$ arteries. Analysis of the *fbln5*$^{-/-}$ mouse suggests

that elastin plays a key role in the mechanical response of mouse carotid arteries and that functional elastic fibers appears to be necessary for the normal development of the *in vivo* axial stretch ratio. Further studies that quantify the microstructure and constitutive modeling with more advanced models will provide a more definitive link between the microstructure and mechanics of *fbln5*$^{-/-}$ arteries.

CHAPTER 4

EVOLUTION OF BIOMECHANICAL AND MICROSTRUCTURAL PROPERTIES OF COMMON CAROTID ARTERIES IN FIBULIN-5 NULL MICE DURING MATURATION

Introduction

A common characteristic of vascular diseases such as abdominal aortic aneurysms, peripheral arterial disease, and aortic dissection is elastin fragmentation. Examining tissue growth and remodeling in the presence of dysfunctional elastic fibers may provide insight into the adaptive or maladaptive changes that tissues undergo in compensating for structural deficiencies. Many clinical interventions such as bypass grafting take place in patients with previously diagnosed arterial stiffening or using saphenous vein grafts that are stiffer than the arteries they are replacing. This study used the *in vivo* maturation of arteries in fibulin-5 knockout (KO) and wildtype (WT) mice as a platform to study the effects of fibulin-5 and the loss of functional elastic fibers on the growth and remodeling of mouse carotid arteries. Fibulin-5 (*fbln5*) is an extracellular matrix protein that binds to integrins and localizes tropoelastin to microfibrils. The vascular anomalies in *fbln5* knockout mice resemble those that occur during ageing. Previous studies have shown that arteries from *fbln5* knockout mice have altered biomechanical as well as microstructural properties. In this study, we measured the microstructural properties and the mechanical response, of common carotid arteries during maturation from fibulin-5 null and wildtype mice. We also performed parameter estimation using biaxial testing data collected from arteries aged 3, 4, and 8 weeks. Multiphoton microscopy was used to image collagen fibers in pressurized and stretched arteries, and image stacks were analyzed to quantify collagen fiber orientations. Biaxial

tests revealed significant differences in mechanical response between genotypes and between different age groups. Analysis of image stacks collected through multiphoton microscopy suggests that there is a greater variation in fiber angles between genotypes than between different ages. Parameter estimation revealed significant differences in material parameters between genotypes and between age groups. The results of this study suggest that functional elastic fibers are necessary for normal maturation of mouse carotid arteries, and without *fbln5*, the mechanical response is altered. Parameter estimation and fiber orientation analysis suggest that this remodeling takes place through changes in material as well as microstructural properties.

Methods

Surgical preparation and vessel isolation

Adult male WT and *fbln5* KO mice (3, 4, and 8 weeks old) on the C57-BL6 X 129/SvEv background were euthanized with an overdose of CO_2. All mice were generated from a breeding pair originally obtained from Dr. Hiromi Yanagisawa (UT Southwestern). Both common carotid arteries were excised under sterile conditions, placed in Dulbecco's phosphate buffered saline (PBS), dissected free of perivascular tissue, and mounted on the glass cannulae of our biomechanical testing device using sterile suture (46). All animal procedures were approved by the Institute Animal Care and Use Committee (IACUC) at the Georgia Institute of Technology.

Biaxial mechanical testing

A previously described device was used to perform cylindrical biaxial biomechanical testing and to perform multiphoton microscopy (154). Pressure-diameter

(*P-d*) data were collected from 0 to 160 mmHg at constant axial extensions, and axial force-length (*f*- ℓ) data were collected over cyclic axial extensions at constant pressures of, *P* = 60, 100, and 140 mmHg. The *in vivo* axial stretch (λ_z^h) ratio was defined as the intersection of force-length tests performed at different transmural pressures (147). Force-length tests were performed first and the *in vivo* axial stretch ratio was used to determine axial stretches ratios for pressure-diameter tests. Axial stretch ratios for pressure-diameter tests were selected to include the *in vivo* axial stretch ratio as well as those above and below the *in vivo* value.

Compliance

Compliance was defined through the relation

$$C\,\Delta P = \Delta\varepsilon = \frac{\Delta r_m}{\bar{r}_m} \tag{4.1}$$

where *C* is compliance, Δr_m is the difference in the mid-wall radii measurements at two different pressures, $\bar{r}_m$ is the mid-wall radius at the mean pressure, ΔP is difference in the two pressures, and $\Delta\varepsilon$ is the local linearized cyclic strain experienced over ΔP.

Opening Angle

After biaxial testing, arteries were cut into two or three segments, and carefully cut open into sectors. The opening angle of the sectors provided a measure of residual stress within the arteries (16). The opening angle, Φ_o,was calculated as

$$\Phi_o = \pi - \frac{(L_o - L_i)}{2H} \text{ and } A = \frac{H(L_o - L_i)}{2} \tag{4.2}$$

where $\frac{(L_o - L_i)}{2H}$ represents the angle of the open sector as defined by Chuong and Fung (16), L_o and L_i are the outer and inner arc lengths of the stress-free sector, H is the wall thickness of the stress-free sector and A is the cross-sectional area of the wall in the open sector (154). A mean value for H was calculated by measuring the area of the sector using a MATLAB script and using equation $(4.2)_2$.

Multiphoton Microscopy

Mouse carotid arteries were mounted on the biaxial testing device and imaged on an LSM 510 META inverted confocal microscope (Zeiss) fitted with a tunable multiphoton laser (Chameleon). The laser was tuned to 800 nm and reached the sample through a 40x/1.3NA oil immersion objective (Zeiss). The META module of the microscope was configured as a 350-450 nm bandpass filter to detect backwards scattering SHG signal from collagen (172, 173). Wildtype vessels were imaged at λ_z=1.54 and *P*=110 mmHg as well as at λ_z=1.39. Knockout vessels were imaged at λ_z=1.39 and *P*=110 mmHg. Here, $\lambda_z = l/L$ where l is the current length and L is the original unloaded length; l and L were measured as the distance between mounting sutures, while on the mechanical testing device. Axial stretch ratios of λ_z=1.54 and λ_z=1.39 represent *in vivo axial* stretch ratios for 8 week old WT and KO mice as determined in this study and blood pressures were previously measured (164).

Measurement of collagen fiber angle distribution

The angular distribution of collagen fibers for each optical slice in a z-stack was estimated using a MATLAB script modified from a previously reported fast Fourier series algorithm (107, 152). Only collagen fibers in the adventitia of the vessel were

visible with the imaging system (154). The first and last optical slices of collagen fibers within the image stack were determined by reconstructing the vessel and examining the orthogonal views. Each optical slice was low-pass filtered, converted to a binary image using Otsu's method to threshold, and windowed with a 2D Tukey window. A fast Fourier transform was performed on each optical slice, and a power spectrum was generated. This power spectrum was filtered and used to generate a histogram of frequency intensities between -90 and 90 degrees binned into 4 degree increments. The relative location of each optical slice was normalized through the thickness of the adventitia, and corresponding wall locations of optical slices were averaged across samples within each experimental group to generate a surface of fiber angle distributions through the thickness of the adventitial layer.

Protein content assays

Collagen and elastin mass fractions were measured using quantitative dye binding assays. Samples were weighed before and after overnight vacuum drying. Collagen was extracted from dried arteries by incubating for 48 hours at 37°C in a pepsin solution (1:3 mass ratio of pepsin to tissue in 0.2mL of 0.5 M acetic acid). After extraction, the collagen content of each sample was measured using a Sirius red assay. Elastin was extracted by heating at 100°C in 100μL of 0.5M oxalic acid for four successive extractions. After each extraction, samples were centrifuged at 10,000g and the supernatant collected and pooled. The Fastin kit (Biocolor) was used to quantify the elastin content of pooled elastin extracts. Both dry and wet collagen and elastin mass fractions were calculated.

Parameter estimation

A four-fiber constitutive model was used to estimate material and structural parameters (4). This model has been shown in the past to capture the salient features of biaxial tests of arteries (45, 154). Parameters were estimated using the MATLAB optimization function *lsqnonlin* and minimizing the error function,

$$error = \sum_{i=1}^{n}\left(\frac{P_{meas}(i) - P_{model}(i)}{P_{mean}}\right)^2 + \sum_{i=1}^{n}\left(\frac{f_{meas}(i) - f_{model}(i)}{f_{mean}}\right)^2 \quad (4.3)$$

where $P_{meas}(i)$ is the measured pressure for data point i, $P_{model}(i)$ is the pressure predicted by the model at data point i, P_{mean} is the mean of all measured pressures, $f_{meas}(i)$ is the measured axial force for data point i, $f_{model}(i)$ is the axial force predicted by the model at data point i, and f_{mean} is the mean of all axial force measurements (56). Fitting errors for each sample were calculated by dividing the error function, equation (4.3), by the total number of data points, $2n$.

Statistical analysis

Means were compared using two-way ANOVAs with Bonferroni's post-hoc test for pair-wise comparisons. Significance was taken at $p<0.05$.

Results

Biaxial mechanical testing

Significant differences were found in the mechanical response between genotypes at various ages and between ages within genotypes. The *in vivo* axial stretch ratio for WT vessels at significantly increased with age between 3 and 8 weeks while in KO vessels, the *in vivo* axial stretch ratio did not change with age, Figure 4.1.

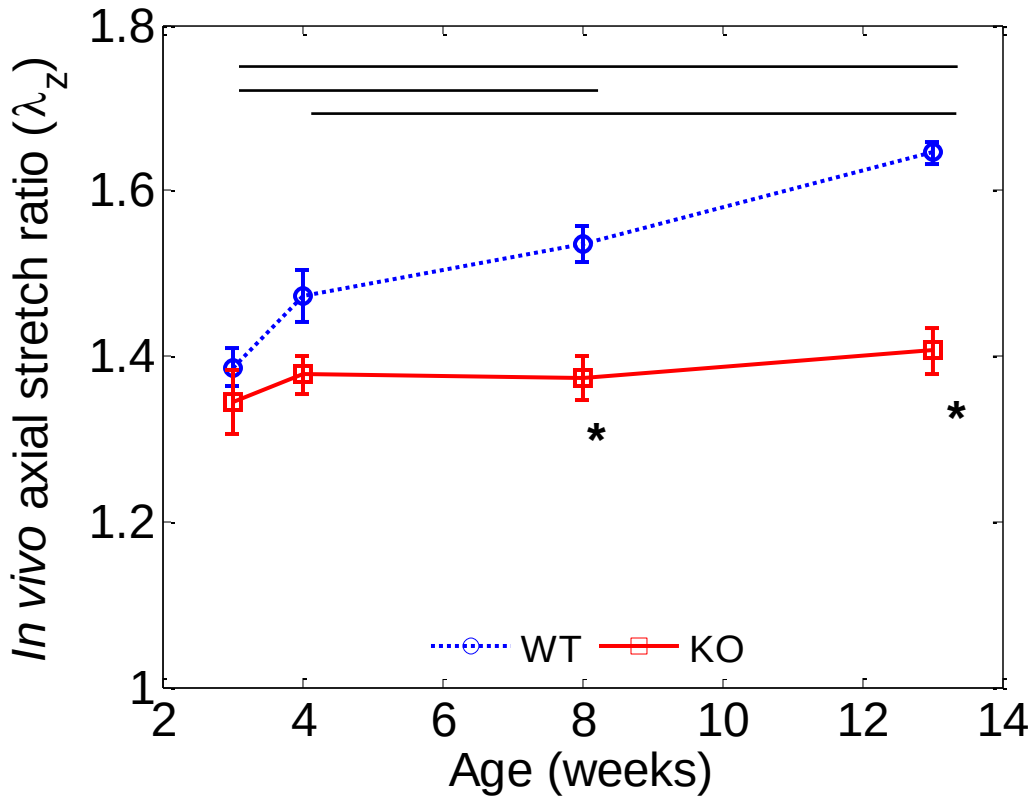

Figure 4.1: The mean in vivo axial stretch ratio was lower in KO vessels for 8 and 13 week samples. The *in vivo* axial stretch ratio for WT vessels at 3 weeks was lower than the *in vivo* axial stretch ratio at 8 and 13 weeks while the *in vivo* axial stretch ratio for WT vessels at 4 weeks was lower than the *in vivo* axial stretch ratio at 13 weeks. There were no statistically significant differences in KO vessels at between ages. Horizontal indicate $p<0.05$ between means at different ages for WT vessels, and asterisks indicate $p<0.05$ between genotypes at the same age. Error bars indicate SEM.

The mean *in vivo* axial stretch ratio was lower in KO vessels for 8 and 13 week samples.

The pressure-diameter test results were used to calculate the midwall radii defined as the mean of the outer and inner radii measured at each pressure, Figure 4.2.

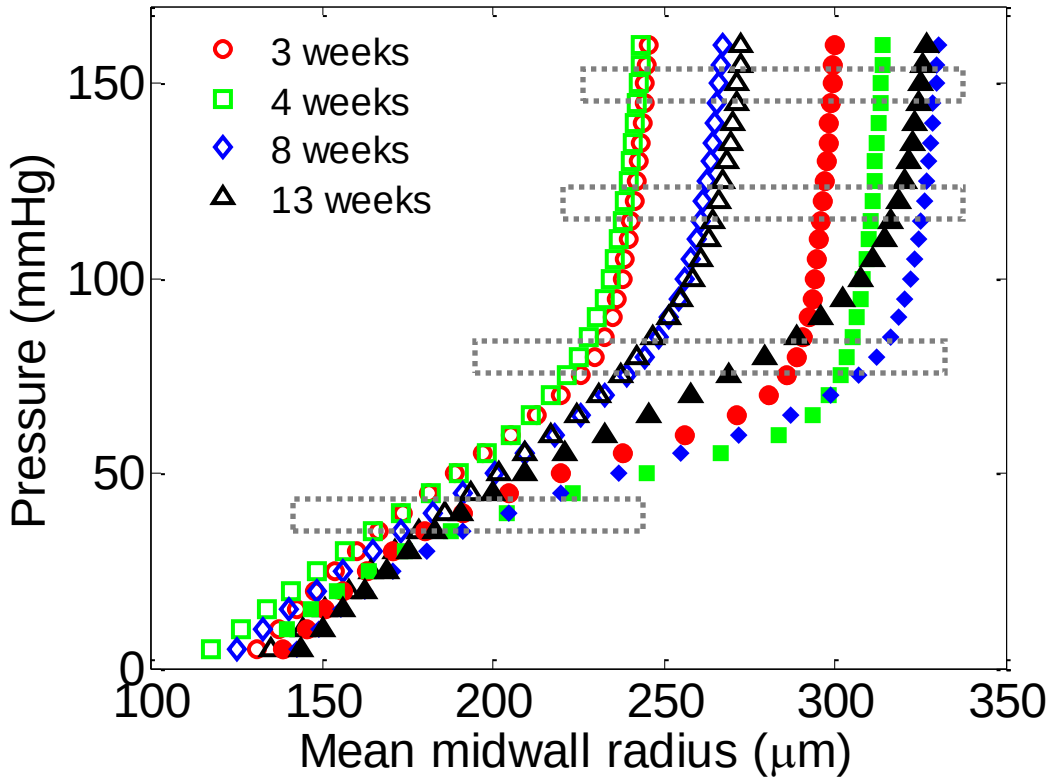

Figure 4.2: Pressure-diameter tests indicate a stiffer mechanical response from KO vessels when compared to WT vessels. A two-way ANOVA was performed at the pressures indicated by the dotted rectangles, P=40, 80, 120, and 150 mmHg. Open symbols indicate KO vessels, and solid symbols indicate WT vessels.

The mean pressure-radius response at the *in vivo* axial stretch ratio suggests that KO vessels at all ages have an overall stiffer circumferential response than WT vessels. Mean midwall radii were also compared at pressures of 40, 80, 120 and 150mmHg. At all ages and all pressures compared, KO vessels had a statistically lower mean midwall radii except for the 13 week age groups at P=40mmHg, Figure 4.3.

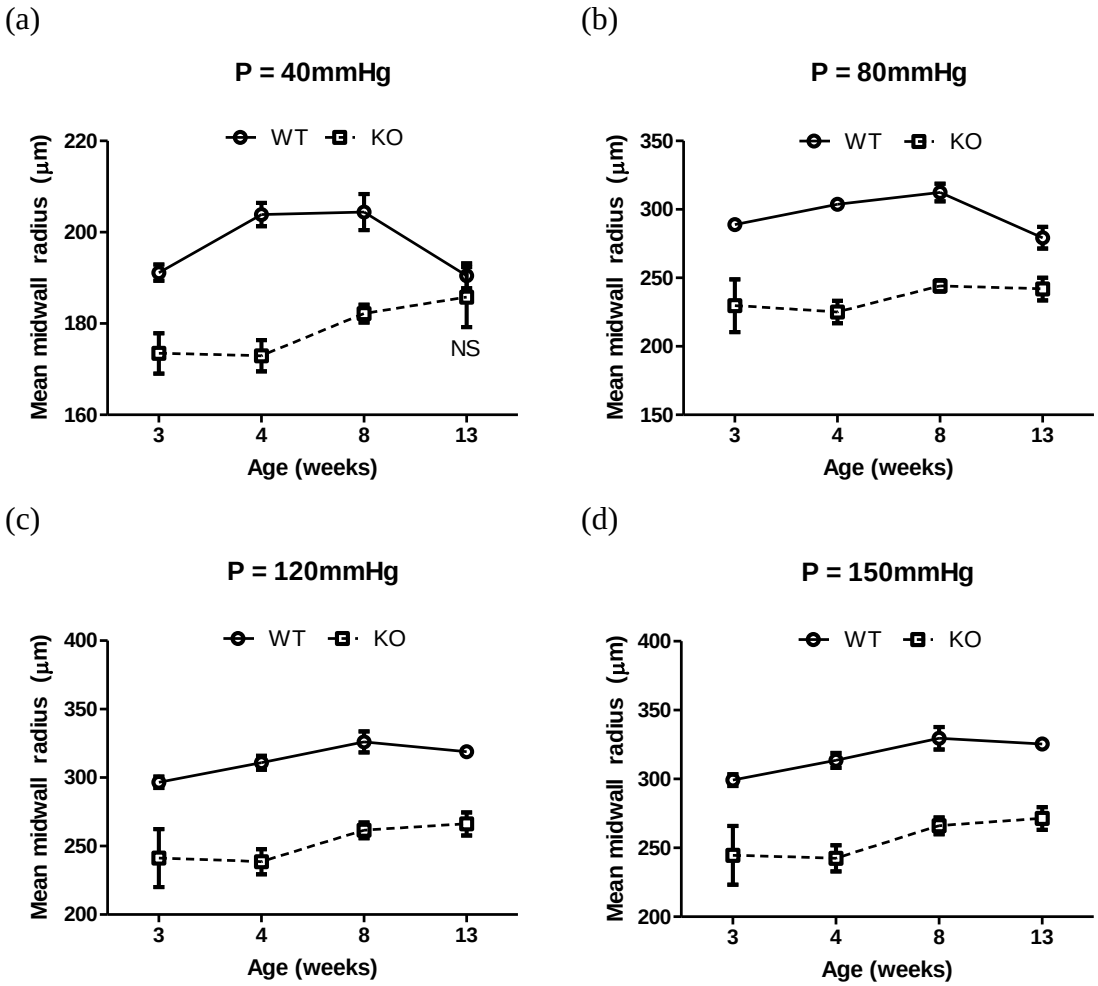

Figure 4.3: KO vessels had smaller mean midwall radii at nearly all pressures and for all ages; the 13 week group at P=40mmHg did not show differences. Genotype accounted for between 44% and 64% of the differences in variance, and was a significant effect at all pressures analyzed, P=40 (a), P=80 (b), P=120 (c), and P=150mmHg (d). Age was a significant effect at P=40mmHg (a). Interaction effects were significant at P=40mmHg. There were no differences between age groups, and NS indicates a nonsignificant difference between genotypes. Error bars indicate SEM.

In WT vessels, there was a greater variation in *in vivo* axial force over time than in KO vessels, Figure 4.4.

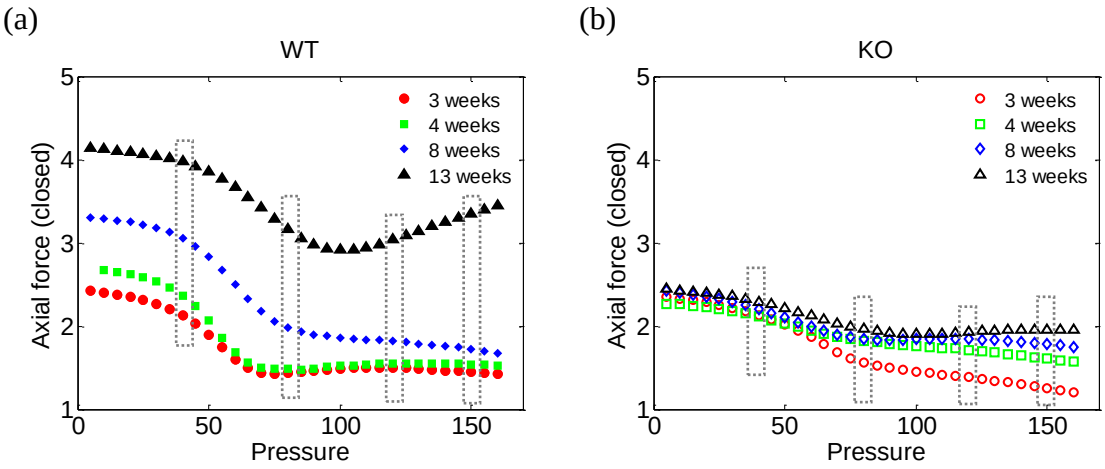

Figure 4.4: In KO vessels, the axial force measured at the *in vivo* axial stretch ratio did not vary across ages. A two-way ANOVA was performed at the pressures indicated by the dotted rectangles, P=40, 80, 120, and 150 mmHg. Open symbols indicate KO vessels, and solid symbols indicate WT vessels.

The mean *in vivo* axial force, the axial force measured by the force transducer during pressure-diameter cycles performed at the *in vivo* axial stretch ratio, was also compared at P=40, 80, 120, and 150mmHg using two-way ANOVAs, Figure 4.5. The axial fore in WT vessels increased between 3 and 13 weeks while the axial force in KO vessels did not change significantly with age, Figure 4.5. At 13 weeks, there was the axial force of WT vessels was significantly greater than that of KO vessels.

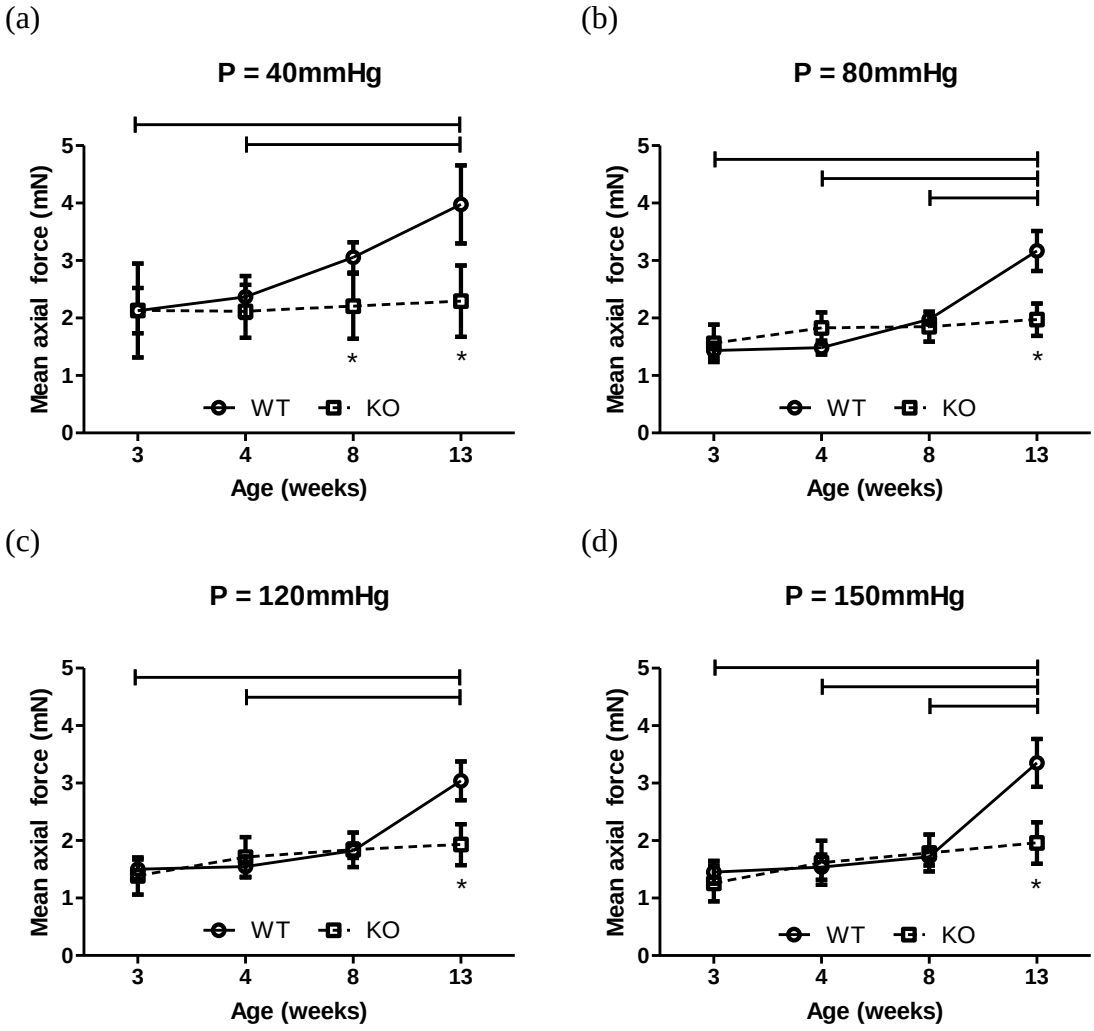

Figure 4.5: At 13 weeks, the axial force was greater for WT vessels than in KO vessels. Axial force was compared across ages and genotypes at P=40 (a), 80 (b), 120 (c), and 150mmHg (d). KO vessels were not significantly different across different ages. Asterisks indicate $p<0.05$ between genotypes at the same age, and horizontal lines indicate $p<0.05$ between ages in WT vessels. Error bars indicate SEM.

Mean local compliance of WT vessels varied with age while the mean compliance of KO vessels remained at similar levels, Figure 4.6.

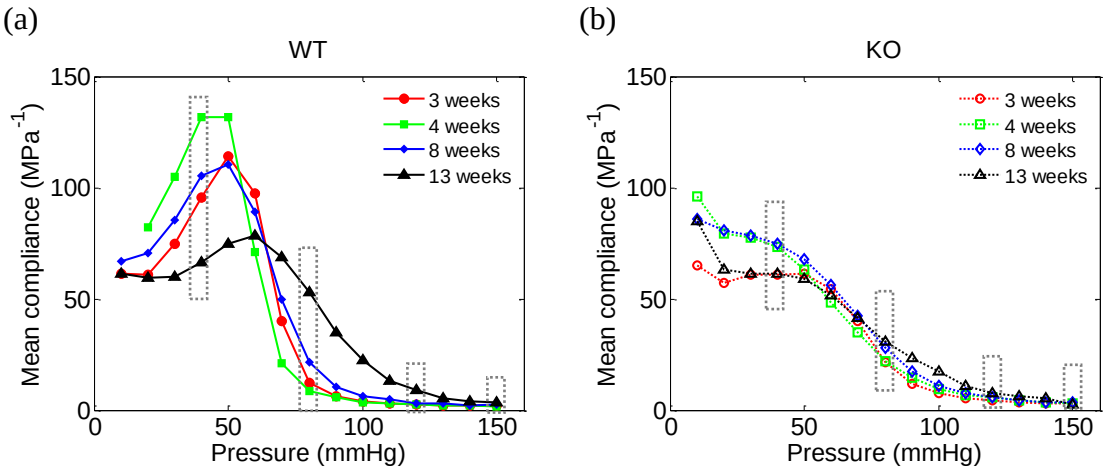

Figure 4.6: Mean local compliance varied with age for WT vessels while KO vessels maintained similar levels of compliance at all ages. A two-way ANOVA was performed at the pressures indicated by the dotted rectangles, P=40, 80, 120, and 150 mmHg. Open symbols indicate KO vessels, and solid symbols indicate WT vessels.

At all pressures analyzed, local compliance did not vary with age for KO vessels; however, compliance did change with age between 3 and 13 weeks in WT vessels, Figure 4.7. In WT vessels, the local compliance at P=40mmHg decreased with age while at P=80, 120, and 150mmHg, the local compliance increased with age. In KO vessels, the local compliance did not vary with age. Differences in local compliance between genotypes was only observed at P=40 and 80mmHg.

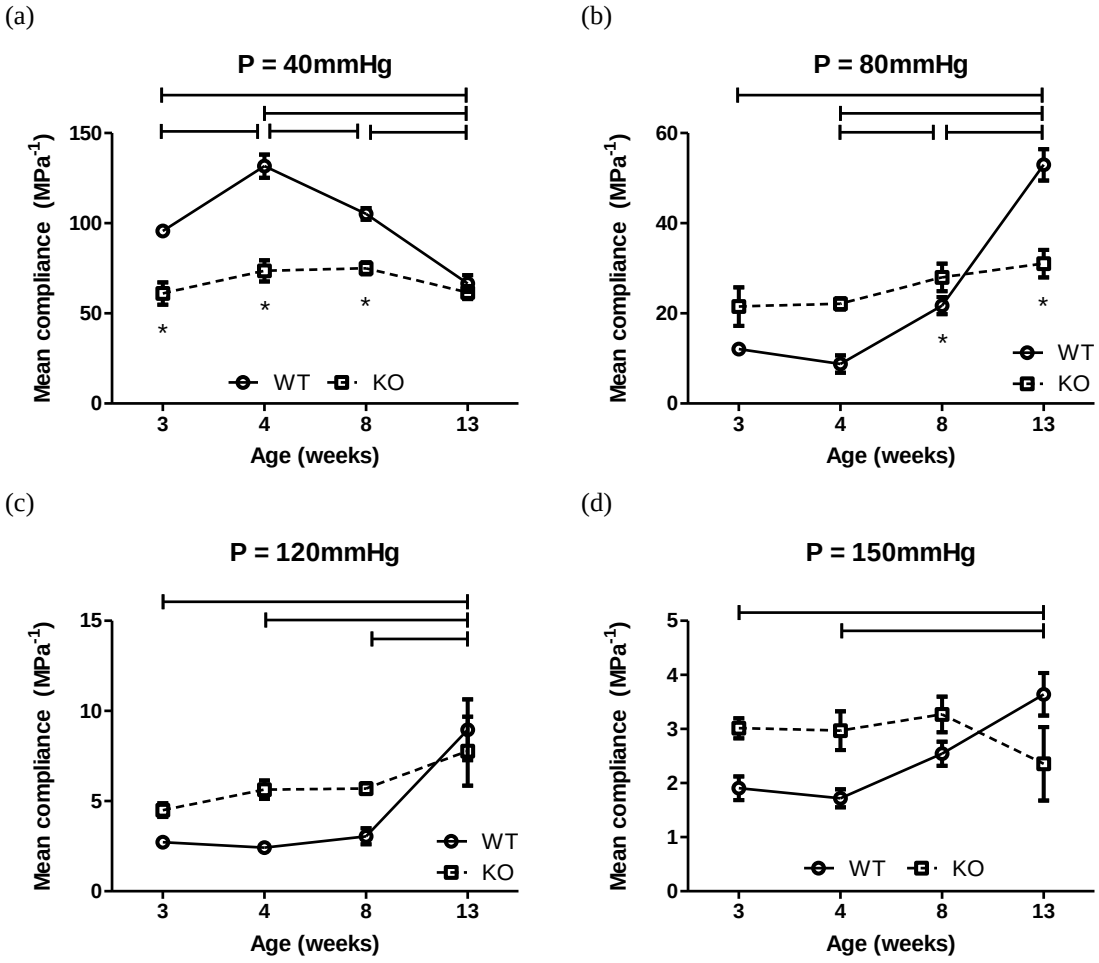

Figure 4.7: Local compliance varied with age in WT vessels at all pressures analyzed; however, the compliance of KO vessels did not change with age. Interaction effects were significant at P=40, 80 and 150mmHg. At P=120, age and genotype effects were significant with age accounting for 36% and genotype accounting for 6% of the total variation. KO vessels were not significantly different across different ages. Asterisks indicate $p<0.05$ between genotypes at the same age, and horizontal lines indicate $p<0.05$ between ages in WT vessels. Error bars indicate SEM.

The mean opening angle decreased with age for WT vessels while no significant differences were seen within KO vessels between any ages, Figure 4.8. At the 4, 8, and 13 week age groups, the opening angle was lower in WT vessels while the difference in opening angle between genotypes was not statistically significant at 3 weeks.

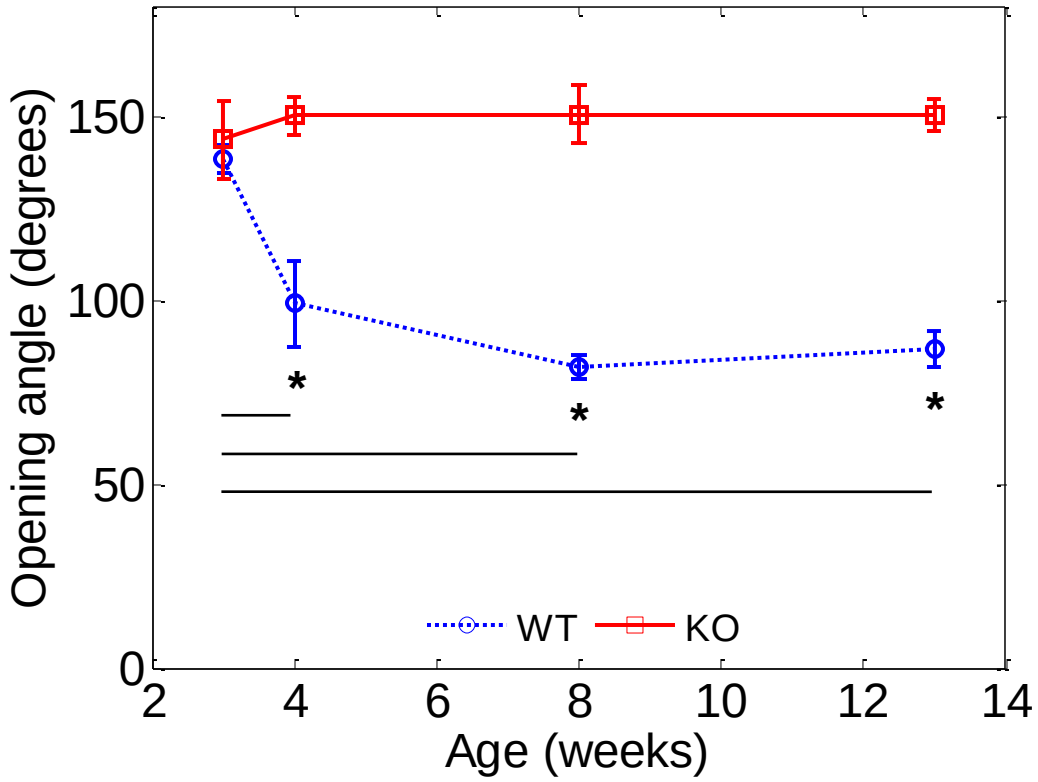

Figure 4.8: The opening angle was not significantly different between genotypes at 3 weeks; however, the opening angle did decrease in WT vessels between 3 week vessels and all other age groups. Asterisks indicate $p<0.05$ between genotypes at the same age, and horizontal lines indicate $p<0.05$ between ages in WT vessels. Error bars indicate SEM.

Measurement of collagen fiber angle distribution. For each artery, fiber angle distributions were quantified for optical slices encompassing the thickness of the adventitia. The thickness of each image stack was normalized and fiber angle distributions at corresponding image slices were averaged to generate a mean fiber angle surface, Figure 4.9.

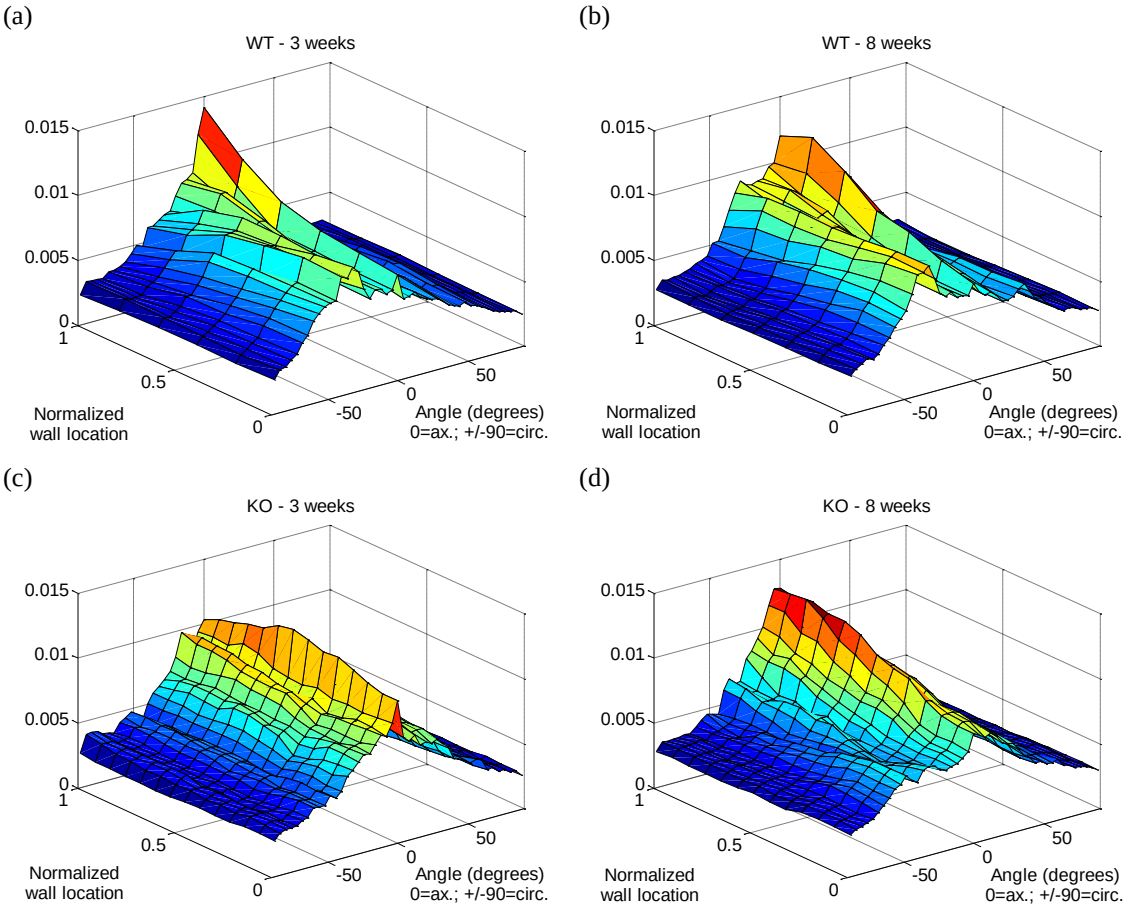

Figure 4.9: Fiber angle distributions varied throughout the thickness of the adventitia. Arteries from KO mice were more aligned in the axial direction than arteries from WT mice. Normalized wall locations at 0 represent the inner surface of the adventitia towards the lumen, and wall locations at 1 represent the outer surface of the adventitia.

Fiber angle distributions varied throughout the thickness of the adventitia, and fibers were more highly aligned in the optical slices taken farther away from the lumen. Fiber angle distributions for all optical slices within each sample were averaged to generate a mean fiber distribution. Mean fiber distributions varied between genotypes, but varied little within genotypes at between 3 and 8 weeks, Figure 4.10.

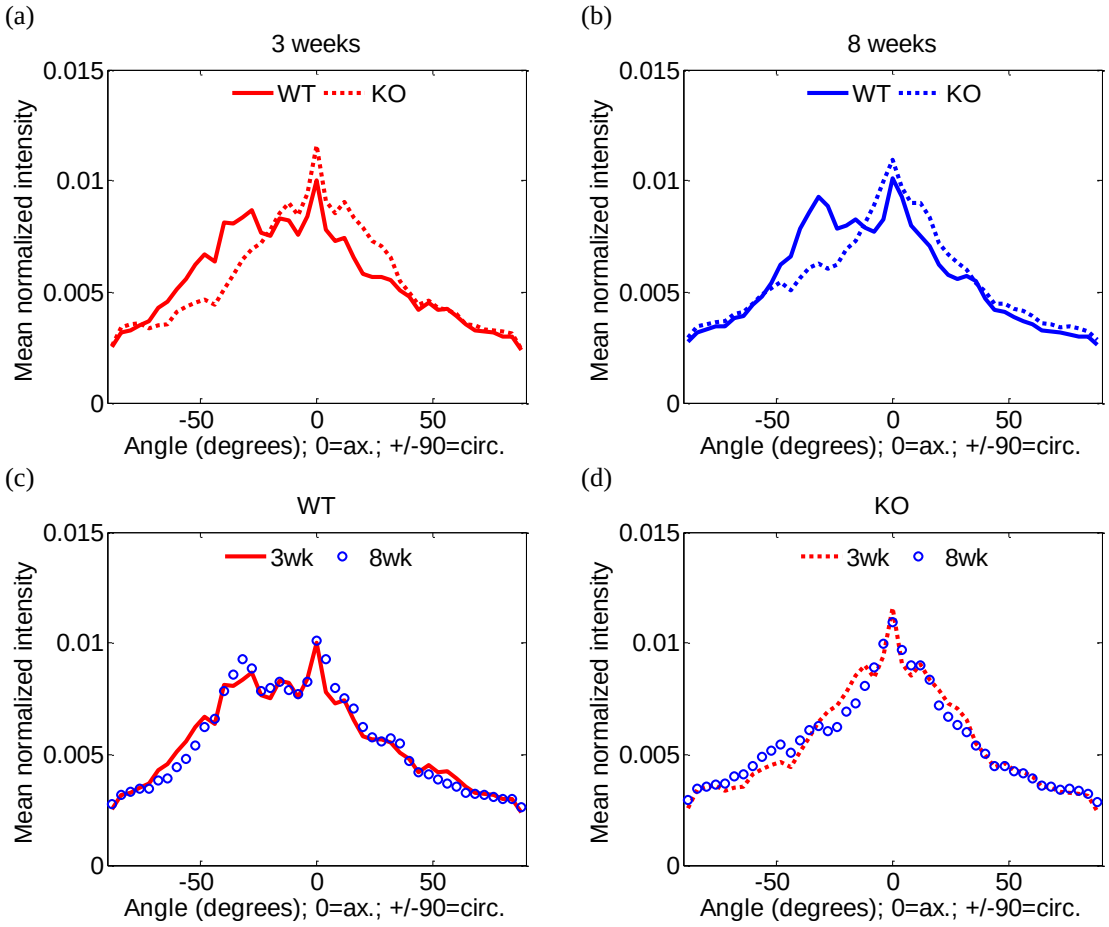

Figure 4.10: Mean fiber distributions varied between genotypes at 3 weeks (a) and at 8 weeks (b) weeks than while fiber distributions of genotypes varied little in between 3 and 8 weeks (c, d).

Protein content assays

The elastin wet mass fraction decreased with age for both WT and KO vessels, Figure 4.11a. The dry elastin mass fraction was not significantly different between ages and genotypes; however, age was a significant source of variation accounting for 15% of the total variation, Figure 4.11b. Collagen wet mass fractions decreased with age, differences between genotypes were not significant, Figure 4.12a. The collagen dry mass

fraction for WT vessels decreased with age; however, differences between genotypes were not different for collagen content calculated on a dry mass basis, Figure 4.12b.

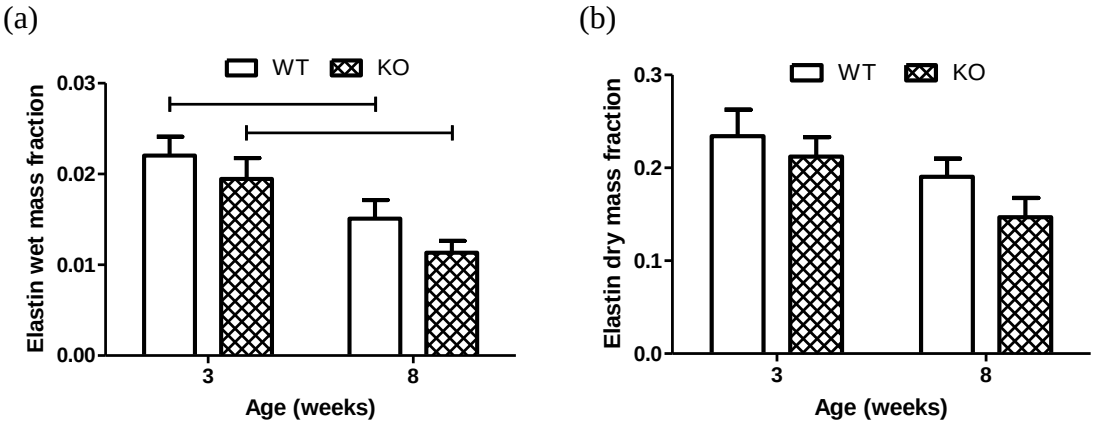

Figure 4.11: The elastin wet mass fraction decreased with age for both WT and KO vessels. In elastin dry mass fractions, no significant differences were seen between samples at different ages or genotypes. Horizontal lines indicate $p<0.05$. Error bars indicate SEM.

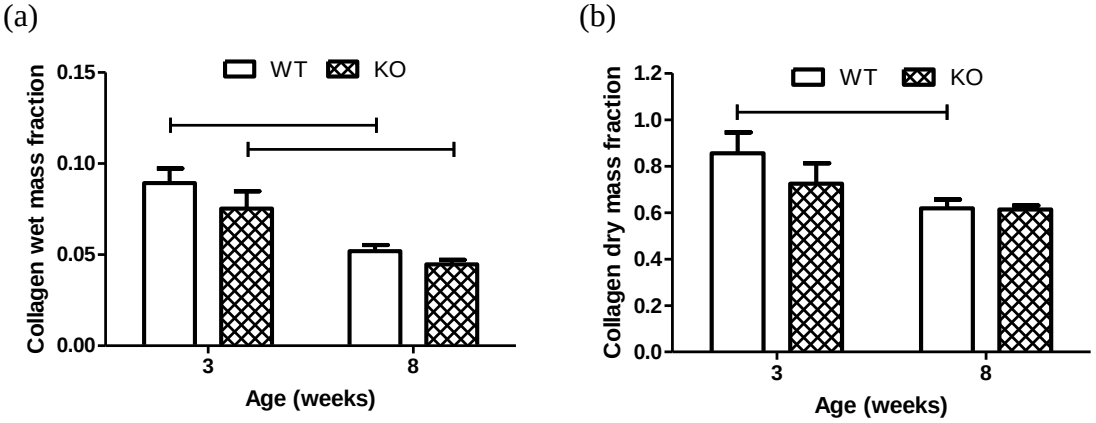

Figure 4.12: Collagen wet mass fractions decreased with age, but was not significantly different between genotypes. In addition, collagen mass fractions decreased with age for WT vessels. Horizontal lines indicate $p<0.05$. Error bars indicate SEM.

Parameter estimation

Parameter estimation reveals that the structural parameter (i.e., fiber angle) does not change with age or genotype, Figure 4.13. In addition, the material parameters $b^{1,2}$

and $b^{3,2}$ did not change with age or with genotype. Material parameters were significantly different between genotypes at 3 weeks for $b^{1,1}$ and $b^{3,1}$ and at 13 weeks for b and $b^{2,2}$. The material parameters $b^{2,1}$, $b^{2,2}$, and $b^{3,1}$ varied with age in KO vessels.

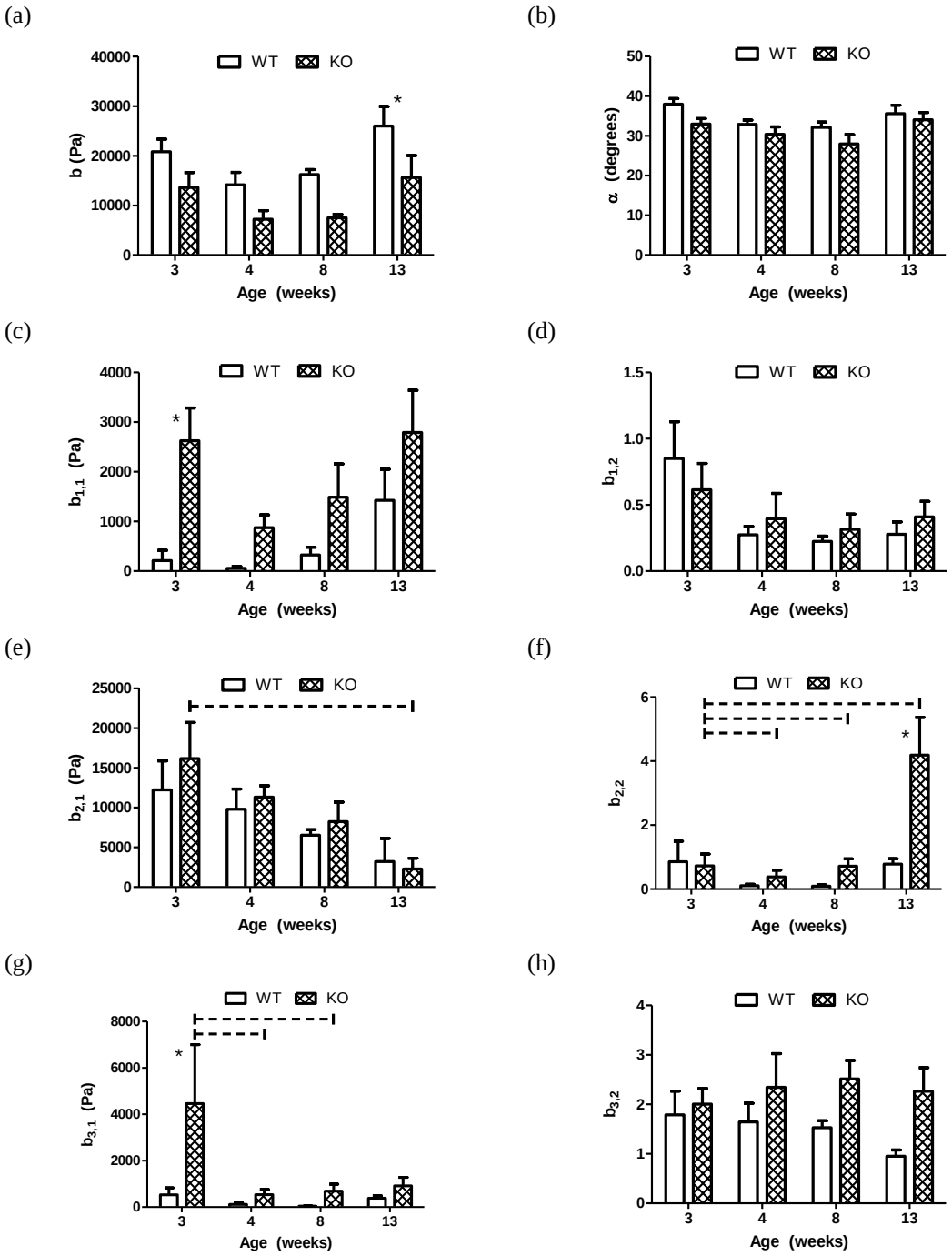

Figure 4.13: Parameter estimation revealed no significant differences in the fiber angle parameter (panel b) between genotypes and between different ages within each genotype. Significant differences were observed in the material parameters, $b^{1,1}$ and $b^{3,1}$, at 3 weeks and in the material parameters, b and $b^{2,2}$, at 13 weeks. In KO vessels, the parameters $b^{2,1}$, $b^{2,2}$, and $b^{3,1}$ were significantly different in various age comparisons. No significant differences in material parameters were calculated for WT vessels at any age. Asterisks indicate $p<0.05$ between genotypes at the same age, and dashed horizontal lines indicate $p<0.05$ between ages in KO vessels. Error bars indicate SEM.

Discussion

Biaxial testing suggests that both age and genotype affect mechanical properties such as pressure-diameter response, *in vivo* axial force, axial stretch ratio, compliance and opening angle. In KO vessels, these properties do not change significantly over the course of maturation, and differences between WT and KO vessels become significant at varying ages. For example, the opening angle decreases overtime in WT vessels and become significantly different from KO vessels at 4 weeks, Figure 4.8, while differences in *in vivo* axial force do not become significant until 13 weeks, Figure 4.1. The midwall radii did not undergo statistically significant changes between different ages within each genotype. However, WT vessels at all age groups exhibited a stiffer mechanical response and greater midwall radii (with the exception at P=40 in the 13 week age group). The pressure-diameter responses measured at the in vivo axial stretch ratio suggests that normal circumferential growth is impaired when elastic fibers are fragments; however, this does not preclude effects from altered SMC migration or proliferation due to the lack of *fbln5*.

The in vivo axial stretch ratio increased over time in WT vessels and differences between genotypes become significant at 8 and 13 weeks. Our findings agree with previous results; namely, Dobrin et al. found that the axial stretch ratio, or prestretch, increases nearly linearly with age (23) and that this increase was due to elastin (25). In WT vessels, the *in vivo* axial force also underwent significant increases between 3 and 13 weeks; however differences between genotypes did not become significant until 13 weeks. This increase in *in vivo* axial force between WT and KO mice agrees with previous experiments in a mouse model with reduced expression of fibrillin-1 (29). These

results suggest that the stretching of intact elastic fibers during maturation may be the cause of the increase in in vivo axial force. In previous experiments on dog carotid arteries elastin was shown to be the primary contributor to axial force (25).

The local compliance varied with age in WT vessels while the local compliance in KO vessels did not undergo significant changes with age. At P=120 and 150mmHg, WT and KO vessels did not have significantly different compliance suggesting that KO vessels may remodel to restore compliance over the physiological pressure range. Under normal *in vivo* conditions, because the artery never experiences P=40mmHg, changes in compliance between genotypes at this pressure may not be relevant in affecting growth and remodeling that take place under physiological condition. However, without knowledge of the *in situ* mechanical response, it is not known whether perivascular surrounding tissue significantly changes the calculated *ex vivo* compliance. It is possible that the perivascular tissue restricts the range of motion of the vessel to a different portion of the pressure-compliance curve than that suggested by physiological pressures.

The opening angle decreased with age in WT arteries, but did not change significantly in KO arteries. In addition, there were no significant differences between genotype in opening angle in samples tested at 3 weeks. A decrease in opening angle during maturation was previously observed in the thoracic aorta between 6 and 30 days of age (66). Because the half-life of elastin is much longer than that of collagen, functional elastic fibers undergo increasing levels of stretch while collagen fibers undergo turnover at their homeostatic stretch ratio, thus inducing increased tension on the lumenal surface of the vessel (83, 127). The lack of changes in collagen and elastin content between WT and KO vessels suggests that changes in material properties may play a role in causing

the changes in opening angles. Changes in opening angles may also arise from changes in geometry or other factors.

Collagen and elastin mass fractions decreased with age, but did not vary significantly between genotypes. The lack of differences in collagen and elastin content suggests that smooth muscle cells may have an effect in the adaptations to the lack of *fbln5* expression. The similarity in collagen and elastin content between genotypes does not preclude, however, any changes in the level of crosslinking. In previous studies of *fbln5* KO mice, analysis of the skin revealed decreased levels of desmosine, but no change in tropoelastin levels (15, 171).

Collagen fiber distributions measured at different ages varied little within each genotype. Larger variations in fiber distributions were seen between genotypes when comparing at the same age. The lack of variation in fiber angles between 3 and 8 weeks suggests that changes in passive mechanical response is likely due to changes in material parameters. Indeed, parameter estimation using a four-fiber model resulted in changes in material parameters between 3 and 8 weeks. However, material parameters that changed with time were only observed in KO vessels while no significant changes in material parameters over time were seen in WT vessels. The high degree of axial fiber alignment in KO vessels may explain the increased axial stiffness of KO vessels (154). Changes in collagen fiber organization due to damage has been previously documented in bioprosthetic aortic heart valves (121, 122); and in humans aortas, changes in fiber alignment with age and tissue depth have also been observed (57).

Parameter estimation revealed significant differences in material parameters and no significant changes in structural parameters in the stress-free state. These finding

suggests that under normal maturation material properties undergo non-significant changes with age and that the lack of fibulin-5 causes changes in material properties of constituents that evolve as vessels adapt to the lack of functional elastin. The structural parameter, α, represents a diagonal family of fibers in the stress-free configuration. When transformed to the *in vivo* configuration, the angles represented in Figure 4.13b may reveal significant differences. In WT vessels, the lack of significant changes in material parameters coupled with the significant changes in mechanical response highlights the need for experimentally measuring material parameters in order to better validate constitutive models. The lack of changes in the fiber angle parameter between genotypes is in contrast to previous studies of knockout mice (45); however, the previous studies did not transform the estimated fiber angle to an *in vivo* fiber angle. Differences in material parameters and *in vivo* fiber distribution suggest that KO arteries adapt to the lack of functional fibers through changes in material properties as well as through changes in fiber orientation. This observation warrants further investigation because the current study did not examine smooth muscle cells, and fibulin-5 has been shown to affect smooth muscle cell migration and proliferation (133).

There are a few limitations to this study that may be addressed in the future. Here, we measured collagen and elastin mass fractions, but did not measure smooth muscle cells content. Active smooth muscle cells play a role in the mechanical response of an artery, and during growth and remodeling, they undergo changes such as hypertrophy (99), proliferation (19) and migration (40, 96). Measurement of smooth muscle cell content and imaging of smooth muscle cell orientation would provide additional insight into the role of fibulin-5 in the microstructural and mechanical properties of arteries. The

protein content assays quantified total collagen and elastin content; however, quantification of the degree of crosslinking may provide further insight into changes in material properties of microconstituents. This study also performed multiphoton imaging and biaxial testing on separate groups of arteries. Performing both tests on a single artery would provide structural information unique to each sample for parameter estimation studies. Finally, because *fbln5* binds to other proteins such as integrins and extracellular superoxide dismutase, the effects observed in this study may not be isolated to fragmented alone (108, 133).

In conclusion, this study highlights the effects of fibulin-5 on the microstructural and mechanical properties of mouse carotid arteries during maturation. We show that although functional elastic fibers are required for the development of a normal mechanical response, KO arteries remodel to restore compliance over physiological pressure ranges. This study also illustrates the advantages of a combined theoretical and experimental approach in analyzing differences in arteries from genetic knockout mice. This study utilizes the collection of biaxial test data at the macroscopic tissue level while quantifying fiber angle distribution at the microstructural level, and we use the experimental data in structurally motivated constitutive relations to elucidate material property relationships that are not yet experimentally tractable.

CHAPTER 5

A 3-D CONSTRAINED MIXTURE MODEL FOR MECHANICALLY-MEDIATED VASCULAR GROWTH AND REMODELING

Introduction

In contrast to the widely applied approach to model soft tissue remodeling employing the concept of volumetric growth, microstructurally-motivated models are capable of capturing many of the underlying mechanisms of growth and remodeling; i.e., the production, removal, and remodeling of individual constituents at different rates and to different extents. A 3D constrained mixture computational framework has been developed for vascular growth and remodeling, considering new, microstructurally-motivated kinematics and constitutive equations and new stress and muscle activation mediated evolution equations.

We employ the general theoretical framework described by Humphrey and Rajagopal (67) for soft tissue growth and remodeling. The purpose of this paper is to develop a computational framework for vascular remodeling that is capable of quantifying spatial and temporal changes in the local mechanical response function in terms of microstructurally-motivated metrics. We extend our (2-dimensional) framework for blood vessel remodeling to altered mechanical loading (47-51) to a 3-dimensional framework and consider new, microstructurally-motivated kinematics and constitutive equations and new evolution equations which relate constituent growth, turnover, and remodeling to stress and muscle activation. Our modeling framework and illustrative simulations can be used to motivate experimental design to identify the most insightful experiments to be performed and to better understand vascular growth and remodeling.

Our computational results for alterations in flow and pressure, using reasonable physiological values for rates of constituent growth and turnover, concur with findings in the literature. For example, for flow-induced remodeling, our simulations predict that, although the wall shear stress is restored completely, the circumferential stress is not restored employing realistic physiological rate parameters. Also, our simulations predict different levels of thickening on inner versus outer wall locations, as shown in numerous reports of pressure induced remodeling. Whereas the simulations are meant to be illustrative, they serve to highlight the experimental data currently lacking to fully quantify mechanically mediated adaptations in the vasculature.

Theoretical Framework

Kinematics

Given the need to track the production and removal of individual constituents, as well as the mechanical states in which these constituents are formed, we model the artery as a constrained mixture. Consider a local neighborhood about a point with position $\mathbf{x}(r,\theta,z)$ in the loaded configuration; let this neighborhood be defined as a cylindrical sector with sides of length $rd\theta$, dz and dr (Figure 5.1a). Let this neighborhood be denoted κ_n in the locally stress-free (or natural) configuration for the mixture, which has position $\mathbf{X}(R,\Theta,Z)$; let this sector have sides, $Rd\Theta$, dZ, dR. Since constituents are constrained to deform together, the current position of each constituent j, denoted $\mathbf{x}^j(r^j,\theta^j,z^j)$, is the same as the current position of the mixture $\mathbf{x}(r,\theta,z)$. Let this neighborhood be denoted κ_t^j in the loaded configuration for each constituent j about point $\mathbf{x}^j$; since $\mathbf{x}^j\left(r^j,\theta^j,z^j\right)=\mathbf{x}(r,\theta,z)$ for a constrained mixture, $\kappa_t^j=\kappa_t$. Each constituent, however, may possess different local stress-free natural configurations,

denoted κ_n^j, that have stress free positions $\mathbf{X}^j(R^j, \Theta^j, Z^j)$, where $\kappa_n^j \neq \kappa_n$; and $\mathbf{X}(R, \Theta, Z) \neq \mathbf{X}(R, \Theta, Z)$. Thus, whereas the mixture natural configuration κ_n is stress-free, the individual constituents within the mixture may be under stress in this configuration; these stresses borne by each constituent balance resulting in a net (mixture) stress of zero in κ_n.

Since individual constituents can be produced, removed, and remodeled in different mechanical states and to different extents, and different constituent classes can possess different natural configurations, we must also consider different members *k* of the same constituent class *j* to possess different natural configurations. Indeed, microscopy reveals significant variations in the undulation of elastin and collagen fibers (84) as well

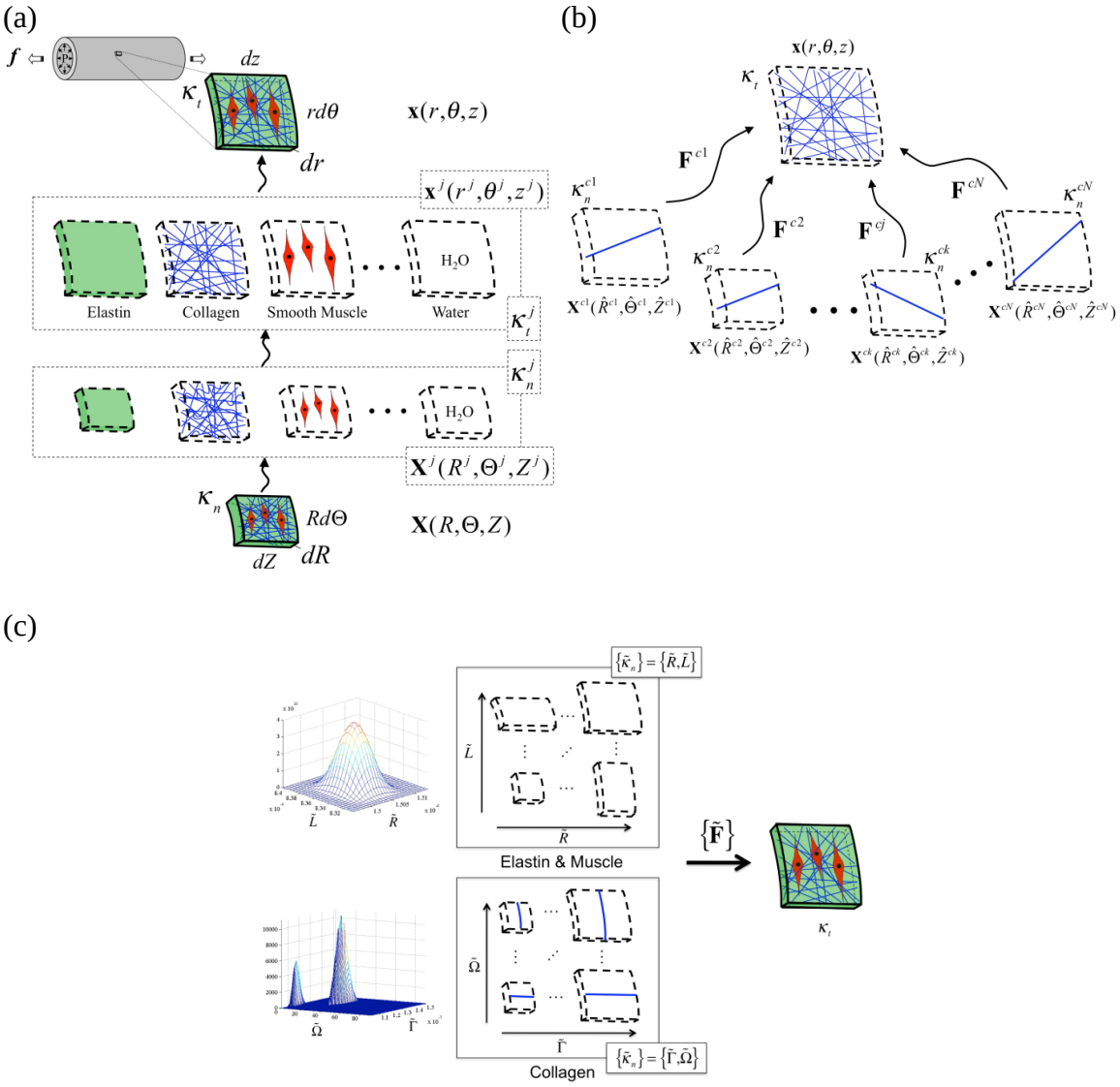

Figure 5.1: Kinematics of a constrained mixture for constituents elastin (*e*), collagen (*c*), muscle (*m*) and water (*w*) that reside within the same neighborhood about a point. Panel (a) depicts key configurations for each constituent class $j = e, c, m,$ and w. Panel (b) depicts key configurations for different members k of the same constituent class j. Panel (c) depicts the use of distribution functions to describe the distribution of constituent j over the set of all possible reference configurations. The set of all possible reference configurations is described in terms of the stress free radius $\tilde{R}$ and length $\tilde{L}$ for elastin and muscle and in terms of the stress free fiber length $\tilde{\Gamma}$ and fiber angle $\tilde{\Omega}$ for collagen.

as in the lengths of the SMC in blood vessels (95). Thus, within the locally stress-free neighborhood κ_n^j, for constituent j, each member k may not be in their stress free, natural

configuration. Rather, each member k of constituent class j may possess its own stress-free natural configuration, denoted κ_n^{jk} which has the position $\mathbf{X}^{\mathrm{jk}}(R^{jk}, \Theta^{jk}, Z^{jk})$; see Figure 5.1b.

As the number of members k becomes large, rather than tracking these many individual members of each constituent class, it is convenient to consider a distribution function $\mathrm{R}^j(\tilde{\kappa}_n; \mathbf{x})$ defined over the set of all possible natural configurations $\{\tilde{\kappa}_n\}$; the distribution function may vary with position $\mathbf{x}$ within the tissue and has the characteristics,

$$\iint \mathrm{R}^j(\tilde{\kappa}_n; r)\, d\tilde{\kappa} \quad \text{and} \quad \mathrm{R}^j(\tilde{\kappa}_n; r) \geq 0 \tag{5.1}$$

The distribution of mass over all possible reference lengths can be written as

$$\Phi^j(\tilde{\kappa}; r) = \phi^j(r)\mathrm{R}^j(\tilde{\kappa}_n; r); \tag{5.2}$$

given $(1)_1$, integration of $\Phi^j(\tilde{\kappa}; r)$ over all possible sets $\{\tilde{\kappa}\}$ at each radial location r yields, ϕ^j, the total mass fraction of constituent j at radial location r.

$\tilde{\kappa}_n$ may be defined in terms of characteristic (infinitesimal) dimensions of a defined natural configuration (Figure 5.1c). For example, for elastin and muscle let the natural configuration $\tilde{\kappa}_n$, with position $\tilde{\mathbf{X}}(\tilde{R}, \widetilde{\Theta}, \tilde{Z})$, again be defined as a cylindrical sector and let this sector have dimensions $d\tilde{R}$, $\tilde{R}d\widetilde{\Theta}$, $d\tilde{Z}$; $\tilde{\kappa}_n$ deformed to κ_t defined as a cylindrical sector with dimensions dr, $rd\theta$ and dz. For an incompressible material, since the motion $(\tilde{R}, \widetilde{\Theta}, \tilde{Z}) \mapsto (r, \theta, z)$ is isochoric, then $\tilde{\kappa}_n$ may be defined in terms of $\tilde{R}d\widetilde{\Theta}$ and $d\tilde{Z}$, leaving $d\tilde{R}$ to be determined from the incompressibility constraint. Thus, let $\mathrm{R}^j(\tilde{\kappa}_n, \mathbf{x}) = \mathrm{R}^j\left(\tilde{R}d\widetilde{\Theta}, d\tilde{Z}; r\right)$ define the distribution of constituent j over all possible

natural configurations; here we restrict this distribution function to be axisymmetric, varying with radial location *r*, but not with θ or *z*. Given this axisymmetry assumption we may let $\mathrm{R}^j\left(\tilde{R}d\tilde{\Theta}, d\tilde{Z}; r\right) = \mathrm{R}^j\left(2\pi\tilde{R}, \tilde{L}; r\right)$, where $\{\tilde{\kappa}_n\}$ is defined in terms of $2\pi\tilde{R}$ and $\tilde{L}$, which define the unloaded dimensions of a cylindrical shell, that have dimensions *r* and *l* (with infinitesimal thickness *dr*) in the loaded configuration.

For inflation and extension of an axisymmetric tube, the map that takes points from $\tilde{\mathbf{X}}\left(\tilde{R}, \tilde{\Theta}, \tilde{Z}\right) \mapsto \mathbf{x}(r, \theta, z)$ is defined as $r = r\left(\tilde{R}\right)$, $\theta = \tilde{\lambda}_\theta\tilde{\Theta}$, and $z = \tilde{\lambda}_z\tilde{Z}$, which has deformation gradient, $\tilde{\mathbf{F}}$, with components $[\tilde{\mathbf{F}}] = diag\{\tilde{\lambda}_r, \tilde{\lambda}_\theta, \tilde{\lambda}_z\}$, where (for elastin and muscle)

$$\tilde{\lambda}_\theta(r) = \frac{r}{\tilde{R}(r)}, \qquad \tilde{\lambda}_z(r) = \frac{l}{\tilde{L}(r)}, \qquad \text{and} \quad \tilde{\lambda}_r(r) = \frac{\partial r}{\partial \tilde{R}} = \frac{\tilde{R}(r)\tilde{L}(r)}{rl} \tag{5.3}$$

here we enforced the incompressibility constraint ($\det\tilde{\mathbf{F}} = 1$) for both the mixture and the individual constituents (which is enforced locally), see equation 5.3_3. Thus, the space of all possible reference configurations is $\{\tilde{\kappa}_n\} = \{\tilde{R}, \tilde{L}\}$. Given specific values for *r*, *l*, and *dr* that defined the current configuration, the set of deformation gradients $\{\tilde{\mathbf{F}}\}$ may be calculated for each combination of $\{\tilde{R}\}$ and $\{\tilde{L}\}$ in the set $\{\tilde{R}, \tilde{L}\}$ via equations (5.3).

For collagen, let the natural configuration $\tilde{\kappa}_n$, with position $\tilde{\mathbf{X}}(\tilde{R}, \tilde{\Theta}, \tilde{Z})$, be described in terms of fiber angles and fiber lengths. Again, let the local neighborhood κ_t in the loaded configuration be defined as a sector with sides of length $rd\theta$, *dz*, and *dr*; let us further define this sector such that $rd\theta/dz = 2\pi r\left(s_p\right)/l\left(s_p\right)$; see Figure 5.1a. Consider a single fiber *k* of constituent *j* that is laid down with a fiber stretch of $\tilde{\lambda}_f = \lambda_f^{jk}\left(s_p\right)$ and a fiber orientation $\tilde{\omega} = \omega^{jk}\left(s_p\right)$ (Figure 5.2).

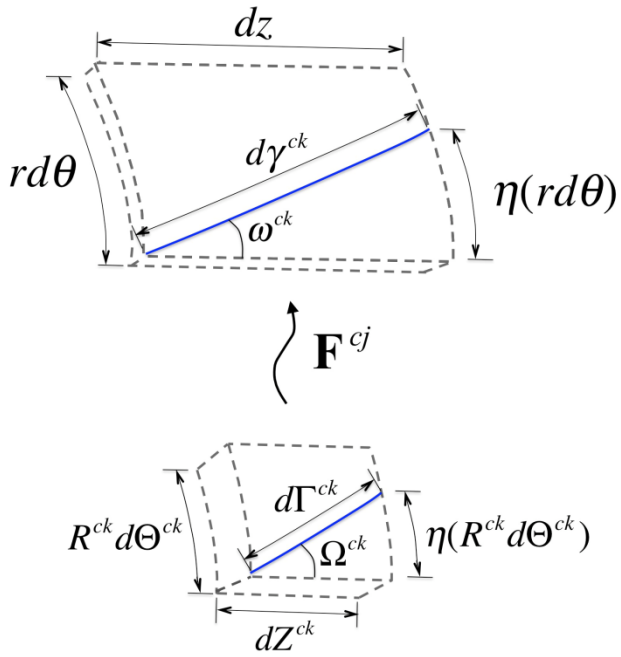

Figure 5.2: Depiction of the kinematics of an individual fiber from the stress-free configuration to the loaded configuration.

Of course, this fiber will be stress free at any angle $\widetilde{\Omega} = \Omega^{jk}$, as long as length of the fiber $d\gamma$ equals the unloaded fiber length $d\widetilde{\Gamma} = d\Gamma^{jk}$. The local neighborhood about this point under stress free conditions κ_n^{jk} will have sides $R^{jk}d\Theta^{jk}$, dZ^{jk}, and dR^{jk}. Let us define this reference configuration such that $R^{jk}d\Theta^{jk} = dZ^{jk}$. It can be shown that, for the case of defining $R^{jk}d\Theta^{jk} = dZ^{jk}$, ω^{jk} is related to Ω^{jk} via

$$\tan\Omega^{jk} = \frac{\eta(R^{jk}d\Theta^{jk})}{dZ^{jk}} = \eta$$

and (5.4)

$$\tan\omega^{jk} = \frac{\eta(rd\theta)}{dz} = \tan\Omega^{jk}\frac{rd\theta}{dz} = \tan\Omega^{jk}\frac{2\pi r(s)}{\ell(s)}$$

Thus, in general,

$$\tilde{\omega} = \tan^{-1}\left[\frac{2\pi r(s)}{l(s)}\tan\tilde{\Omega}\right]. \quad (5.5)$$

In addition, given axisymmetry and neglecting variation along the vessel length, the stretch of any fiber,

$$\tilde{\lambda}_f = \frac{d\gamma}{d\tilde{\Gamma}} = \begin{cases} \dfrac{dz}{d\tilde{\Gamma}\cos(\omega(\tilde{\Omega}))} = \dfrac{\ell(s)}{\tilde{\Gamma}\cos(\omega(\tilde{\Omega}))} & \text{for } 0 \le \tilde{\Omega} \le 45^{\circ} \\ \dfrac{rd\theta}{d\tilde{\Gamma}\sin(\omega(\tilde{\Omega}))} = \dfrac{2\pi r(s)}{\tilde{\Gamma}\sin(\omega(\tilde{\Omega}))} & \text{for } 45^{\circ} \le \tilde{\Omega} \le 90^{\circ} \end{cases} \tag{5.6}$$

where $\widetilde{\Gamma}$ is the effective stress free length of a fiber over the entire radius and length of the vessel, in contrast to $d\tilde{L}$, which is the stress-free length over the local neighborhood about a point. Thus, given specific values for *r* and *l* that define the current configuration, the fiber stretch $\tilde{\lambda}_f$ and fiber angle $\widetilde{\omega}$ may be calculated for all possible combinations of $\tilde{\Gamma}$ and $\widetilde{\Omega}$ in the $\{\tilde{\Gamma}, \widetilde{\Omega}\}$-space via equations (5.4) and (5.5).

In traditional vascular mechanics, one typically considers three configurations: a loaded configuration β_t, a traction-free (unloaded) configuration β_u, and a (nearly stress-free) reference configuration β_o (Figure 5.3). Here, the stress-free configuration is approximated by an excised arterial ring that 'springs open' when cut radially to relieve a large part of the residual stress (16). As all three configurations are measurable, this approach is experimentally tractable. For inflation and extension of a residually-stressed axisymmetric tube, the map$\mathbf{X}_o(R, \Theta, Z) \mapsto \mathbf{p}(\rho, \vartheta, \zeta)$ is defined as $\rho = \rho(R)$, $\vartheta = (\pi/\Theta_o)\Theta$, and $\zeta = \Lambda Z$ and the map $\mathbf{p}(\rho, \vartheta, \zeta) \mapsto \mathbf{x}(r, \theta, z)$ is defined as $r = r(\rho)$, $\theta = \vartheta$, and $z = \lambda_z \zeta$. Thus, the map $\mathbf{X}_o(R, \Theta, Z) \mapsto \mathbf{x}(r, \theta, z)$ is defined as $= r(R)$, $\theta = (\pi/\Theta_o)\Theta$, and $z = \lambda_z \Lambda Z$ which has the deformation gradient with components $[\mathbf{F}] = \mathrm{diag}[(\partial r/\partial R), (\pi r/\Theta_o R), (\lambda_z \Lambda)]$ in cylindrical coordinates. Whereas the radially-cut

configuration β_o is a convenient and experimentally-tractable configuration, it is not necessarily stress-free at all points; i.e., in β_o the local neighborhoods for all points $\widehat{\mathbf{X}}\left(\hat{R}, \widehat{\Theta}, \hat{Z}\right)$ are not necessarily in their natural configuration κ_n for the mixture; nor are all points in the natural configurations κ_n^j for any constituent j. It is important to note, however, that the natural configurations κ_n, κ_n^j, κ_n^{jk}, and $\{\tilde{\kappa}_n\}$ are not experimentally tractable. Rather, we must prescribe the distribution of each constituent over the space of all possible natural configurations $\{\tilde{\kappa}_n\}$ and calculate β_o, and β_u using an appropriate stress response function. These predicted values for β_o, and β_u may then be compared to experimental data.

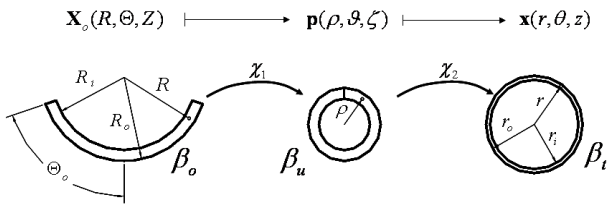

Figure 5.3: Traditional kinematics for blood vessel mechanics which considers a loaded configuration β_t, a traction-free (unloaded) configuration β_u, and a (nearly) stress free configuration β_o that results from imposing a single radial cut in the traction free configuration.

Stress-response

The balance of linear momentum for each constituent class and mixture on the whole requires that

$$\operatorname{div}(\mathbf{T}^j)^{\mathrm{T}} + \rho^j \mathbf{b}^j + \mathbf{p}^j + \hat{m}^j \mathbf{v}^j = \rho^j \mathbf{a}^j \quad \text{and} \quad \operatorname{div}(\mathbf{T})^{\mathrm{T}} + \rho \mathbf{b} = \rho \mathbf{a} \tag{5.7}$$

respectively, where ρ^j is the mass density, $\mathbf{v}^j$ the velocity, $\hat{m}^j$ the (net) local mass production per unit volume, $\mathbf{T}^j$ the Cauchy stress, $\mathbf{b}^j$ the body force, $\mathbf{p}^j$ a momentum exchange that arise between constituents, and $\mathbf{a}^j$ the acceleration for each constituent class j (which includes all members k) and ρ is the density, $\mathbf{T}$ the Cauchy stress, $\mathbf{b}$ the body force, and $\mathbf{a}$ the acceleration for the mixture as a whole (67). For a constrained mixture undergoing a quasi-static process, in the absence of body forces, equations $(5.7)_1$ and $(5.7)_2$ reduce to $\operatorname{div}\left(\mathbf{T}^j\right)^{\mathrm{T}} + \mathbf{p}^j + \hat{m}^j\mathbf{v}^j = 0$ and $\operatorname{div}(\mathbf{T})^{\mathrm{T}} = 0$, respectively. Humphrey and Rajagopal (67) note, however, the difficulty in defining traction boundary conditions in terms of the 'partial' stresses $\mathbf{T}^j$ and in measuring the momentum exchanges that arise between constituents, and suggest an alternative approach wherein one defines the total mixture stress; in this manner, one need only solve the boundary value problem on the mixture (equation $(5.7)_2$), without concern with the partial stress boundary condition (equation $(5.7)_1$). Thus, let the stress of the mixture at any point be described by a simple rule of mixtures (7, 51) as

$$\mathbf{T} = \sum_j \left[\int_{\{\tilde{\kappa}\}} \Phi^j(\tilde{\kappa}; r)[\mathbf{T}^j(\tilde{\mathbf{F}}) + \mathbf{T}^j_{act}(\tilde{\mathbf{F}})]d\tilde{\kappa} \right] \tag{5.8}$$

where $\mathbf{T}^j\left(\tilde{\mathbf{F}}\right) = -p^j\mathbf{I} + 2\tilde{\mathbf{F}}\left(\partial\hat{W}^j/\partial\tilde{\mathbf{C}}\right)\left(\tilde{\mathbf{F}}\right)^T$ is the Cauchy stress for each 'passive' constituent j with deformation gradient $\tilde{\mathbf{F}}$ (modeled as an elastic material), $\mathbf{T}^j_{act}\left(\tilde{\mathbf{F}}\right)$ is the 'active' contribution to the Cauchy stress associated with cellular contraction, $\tilde{\mathbf{C}}$ is the right Cauchy-Green strain tensor, $\left[\tilde{\mathbf{C}}\right] = \left[\tilde{\mathbf{F}}\left(\tilde{\mathbf{F}}\right)^T\right] = diag\left\{\left(\tilde{\lambda}_r\right)^2, \left(\tilde{\lambda}_\theta\right)^2, \left(\tilde{\lambda}_z\right)^2\right\}$, $\hat{W}^j$ is the strain-energy function for constituent class j, and p^j is a Lagrange multiplier due to (local) incompressibility for each constituent. We will consider a mixture of four key

structural constituents: elastin (*e*), collagen (*c*), smooth muscle (*m*) and water (*w*). We will model water as an inviscid fluid, thus $\mathbf{T}^w = -p^w\mathbf{I}$ (i.e., $2\tilde{\mathbf{F}}\left(\partial\hat{W}^j/\partial\tilde{\mathbf{C}}\right)\left(\tilde{\mathbf{F}}\right)^T = 0$) and

$$\mathbf{T} = -p\mathbf{I} + \sum_j \int_{\{\tilde{\kappa}\}} \Phi^j \left[\tilde{\mathbf{F}}\left(\frac{\partial \hat{W}^j}{\partial \tilde{\mathbf{C}}} \right)(\tilde{\mathbf{F}})^T + \mathbf{T}^m_{act}(\tilde{\mathbf{F}}) \right] d\tilde{\kappa} \tag{5.9}$$

where $p = \sum_j \int_{\{\tilde{\kappa}\}} (\Phi^j p^j) d\tilde{\kappa}$ is a Lagrange multiplier due to incompressibility on the mixture as a whole and we consider muscle to be the only constituent with an active contribution to the stress.

For inflation and extension of a long, straight, axisymmetric tube equilibrium requires that $T_{r\theta} = T_{rz} = 0$ and $\partial T_{rr}/\partial r + (T_{rr} - T_{\theta\theta})/r = 0$. Noting that $T_{rr}(r_i) = -P$ the luminal pressure and $T_{rr}(r_o) = 0$, equilibrium requires that

$$P = \int_{r_i}^{r_o} (\hat{T}_{\theta\theta} - \hat{T}_{rr}) \frac{dr}{r} . \tag{5.10}$$

where $\hat{\mathbf{T}} = \mathbf{T} + p\mathbf{I}$, the second term in equation (5.9), is the so-called 'extra' stress due to the deformation. Axial equilibrium requires that axial force maintaining the in vivo axial extension is $f = 2\pi \int_{r_i}^{r_o} T_{zz} r dr$, which can be written as

$$f = \pi \int_{r_i}^{r_o} (2\hat{T}_{zz} - \hat{T}_{\theta\theta} - \hat{T}_{rr}) r dr + \pi r^2 P(1-\xi) , \tag{5.11}$$

where ξ = 1 or 0 for a closed or open ended tube, respectively; see Humphrey (68). For ex vivo biomechanical testing, ξ = 1.

As noted above, we seek to prescribe local natural configurations of each

constituent and predict the global unloaded configuration β_u and (nearly) stress-free configurations β_o of the mixture. To find β_u, we set *P=0* and *f=0* in equations (5.10) and (5.11), and solve for $r_i \equiv \rho_i$ and $l \equiv L_u$; $r_o \equiv \rho_o$, and thus, the thickness H_u may be determined from the incompressibility constraint. If we impose a single radial cut in an unloaded vessel, the bending moment, *M*, is given as

$$M = \int_{r_i}^{r_o} (-p + \hat{T}_{\theta\theta}) r dr \quad \text{where,} \quad p(r) = \hat{T}_{rr} + P - \int_{r_i}^{r} \frac{\hat{T}_{\theta\theta} - \hat{T}_{rr}}{r} dr \,. \tag{5.12}$$

To determine β_o, following Rachev (113), we set *P=0*, *f=0*, and *M=0*, and solve for $r_i \equiv R_i$, $l \equiv L_o$, and Θ_o; again, R_o, and thus the thickness H_o, may be determined from incompressibility.

Constitutive Equations

We will model elastin as a neo-Hookean material; thus,

$$\hat{W}^e = 2b^e (I_{\tilde{C}} - 3), \tag{5.13}$$

where b^e is the elastic modulus and $I_{\tilde{\mathbf{C}}} = tr(\tilde{\mathbf{C}}) = \tilde{C}_{rr} + \tilde{C}_{\theta\theta} + \tilde{C}_{zz}$ is the first invariant of $\tilde{\mathbf{C}}$.

We model muscle as a transversely isotropic material with a circumferentially preferred direction; thus

$$\hat{W}^m_{pas} = b^m \left(I_{\tilde{\mathbf{C}}} - 3 \right) + \frac{b_1^m}{4b_2^m} \left\{ \exp\left(b_2^m \left(\tilde{C}_{\theta\theta} - 1 \right)^2 \right) - 1 \right\} \tag{5.14}$$

where b^m, b_1^m, and b_2^m are material parameters.

We consider collagen to be comprised of a distribution of fibers with fiber orientations $\widetilde{\omega} \in [0,90]$ and fiber stretches $\tilde{\lambda}_f$. For each fiber, we let

$$\hat{W}^c = \frac{b_1^c}{2b_2^c}\left[\exp\left(b_2^c\left(\tilde{\lambda}_f{}^2 - 1\right)^2\right) - 1\right]. \tag{5.15}$$

where b_1^c and b_2^c are material parameters. Each fiber is oriented in the $\tilde{Z} - \widetilde{\Theta}$ plane, $\tilde{\lambda}_f = \gamma/\widetilde{\Gamma}$ is the stretch of the fiber, where $\tilde{\lambda}_f^2 = \mathbf{M}^n \cdot \tilde{\mathbf{C}}\mathbf{M}^n$, $\mathbf{M}^n = \sin(\Omega_n^j)\mathbf{e}_\theta + \cos(\Omega_n^j)\mathbf{e}_z$; thus, $\tilde{\lambda}_f^2 = \tilde{C}_{\theta\theta}\sin^2\left(\widetilde{\Omega}\right) + 2\tilde{C}_{\theta z}\sin\left(\Omega_n^j\right)\cos(\Omega_n^c) + \tilde{C}_{zz}\cos^2\left(\widetilde{\Omega}\right)$, where $\tilde{\Omega}$ denotes the angle between the fiber direction and $\tilde{Z}$ axis in the reference configuration $\tilde{\kappa}_n$, γ is the length of the fiber in the loaded configuration, $\tilde{\Gamma}$ is the unloaded length of fibers oriented in the direction $\tilde{\Omega}$; note that $\tilde{\Gamma}$ is similar to the 'fiber engagement' length described by Lanir (84) and others. Note, that, we assume that the collagen fibers are embedded in the amorphous matrix described by the isotropic terms in equations (5.13) and (5.14). Note too, that we only consider distribution functions that possess symmetry about the $r - z$ plane and the $r - \theta$ plane; thus the limits of integration in equation (5.15) represent the first quadrant, which is repeated in the 2nd, 3rd, and 4th quadrant.

The active smooth muscle behavior will be modeled following Rachev and Hayashi (114) as

$$\mathbf{T}_{act}^m = T_{act}\,\tilde{\lambda}_\theta\left[1 - \left(\frac{\lambda_M - \tilde{\lambda}_\theta}{\lambda_M - \lambda_o}\right)^2\right]\mathbf{e}_\theta \otimes \mathbf{e}_\theta \tag{5.16}$$

where λ_M is the stretch at which the contraction is maximum, λ_o is the stretch at which

active force generation ceases, T_{act} is a parameter associated with the degree of muscle activation, and $\mathbf{e}_\theta$ is the base vector in the circumferential direction in the loaded configuration.

Evolution Equations

For the simulations herein, we assume that the material parameters for each constituent class remain constant for all material produced or removed. Thus, to quantify growth and remodeling, what remains is to quantify how the distribution of mass over all possible reference configurations $\Phi^j(\tilde{R}, \tilde{L}; r, s)$ changes with position and time as the tissue grows and remodels. Towards this end, we must quantify the rate of production and removal of each constituent and the mechanical state (i.e., natural configuration) of all material being produced.

Growth and Turnover Kinetics

Mass balance for each constituent class j within a mixture and for the mixture as a whole requires that

$$\frac{\partial \rho^j}{\partial s} + \mathrm{div}(\rho^j \mathbf{v}^j) = \dot{m}^j \quad \text{and} \quad \frac{\partial \rho}{\partial s} + \mathrm{div}(\rho^j \mathbf{v}) = 0, \tag{5.17}$$

respectively (68). Assuming that the mixture density does not vary significantly with position and time, $(17)_2$ reduce to $\mathrm{div}(\mathbf{v}) = 0$. For a constrained mixture each constituent, including water, is 'constrained' to deform together; thus, each constituent has the same velocity as the mixture (i.e., $\mathbf{v}^j = \mathbf{v}$ and $\mathrm{div}(\mathbf{v}^j) = \mathrm{div}(\mathbf{v})$) and equations $(5.17)_1$ reduce to $\partial \rho^j / \partial s = \dot{m}^j$.

Consider the local neighborhood κ_t about point $\mathbf{x}(r, \theta, z)$ at time $s = 0 \equiv s_o$ in

the loaded axisymmetric, cylindrical configuration that has mass $dm(s_o, r) \equiv dm_o$, volume $dv(s_o, r) \equiv dv_o$, and mass fractions $\phi_o^j(s_o, r) = dm_o^j / dm_o$ within the region at s_o, where $dm_o^j = dm^j(s_o, r)$ is the mass of constituent *j* at *s* = 0. The mass density of the mixture and the constituents over this region are $\rho_o(r) = dm_o / dv_o$ and $\rho_o^j(r) = \phi_o^j dm_o / dv_o = dm_o^j / dv_o$. At a later time s, following some constituent turnover, including addition or loss of mass (i.e., growth or atrophy), the region may have a new mass, $dm(r, s) \equiv \alpha(r, s) dm_o(r)$, new volume *dv(r,s)* in the current configuration, and new mass fractions $\phi^j(r, s) \equiv [\alpha^j(r, s) / \alpha(r, s)] \phi_o^j(r)$ where $\alpha^j(r, s) = dm^j(r, s) / dm_o^j(r)$. If the mixture density remains nearly constant, (i.e., $\rho(r) \cong \rho_o(r) = \text{constant} \quad \forall\, r, s$, c.f., Rodriguez et al. (119), then $dm / dm_o = dv / dv_o \equiv \alpha(r, s)$ and $\rho^j(r, s) = \frac{\alpha^j(r,s)}{\alpha(r,s)} \rho_o^j(r)$. Note too, that since we assume material incompressibility, the volume of this neighborhood in the natural configuration (of the mixture) κ_n, denoted *dV(r,s)*, is equal to the volume in the loaded configuration *dv(r,s)*; thus $dV(s_o, r) \equiv dV_o = dv_o$ and $dV(s, r) \equiv dV = dv$. Since we are adding mass (and volume), $dV \neq dv_o$, we let

$$\frac{dV}{dV_o}\left(= \frac{dv}{dv_o} = \frac{dm}{dm_o} = \alpha(s, r) \right) = \det \mathbf{F}_g = \lambda_{rg} \lambda_{\theta g} \lambda_{zg} \tag{5.18}$$

where $[\mathbf{F}_g] = diag\{\lambda_{rg}, \lambda_{\theta g}, \lambda_{zg}\}$ is a deformation gradient for the mapping of points from their original natural configuration $\kappa_n(s=0)$ to their current natural configuration $\kappa_n(s)$, where we consider only axisymmetric growth (Figure 5.4). λ_{ig} $(i = r, \theta, z)$ are the so-called growth stretch ratios; see Rodriguez et al. (119), Rachev (113), and Taber (138) which may be written

$$\lambda_{rg} = \frac{dR(s)}{dR(0)}, \quad \lambda_{r\theta} = \frac{R(s)}{R(0)}, \quad \text{and} \quad \lambda_{rz} = \frac{dZ(s)}{dZ(0)}. \tag{5.19}$$

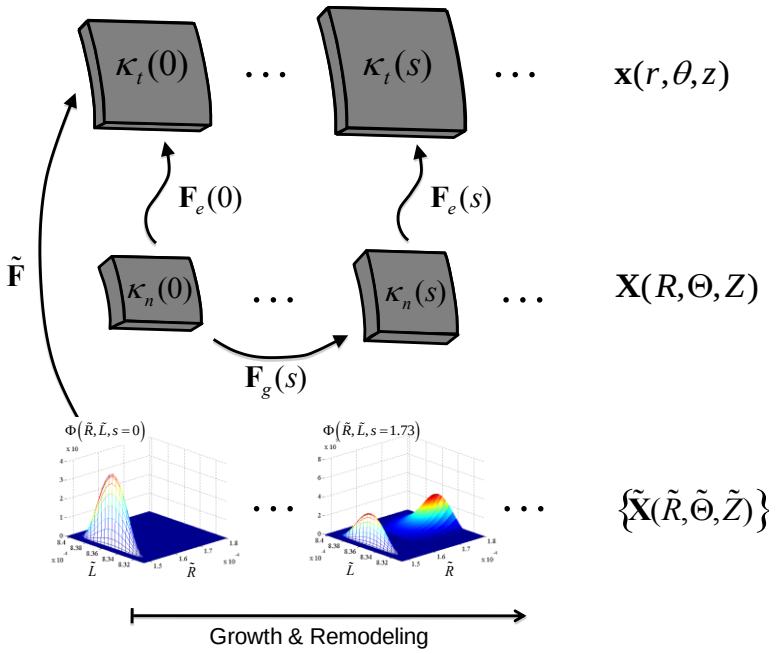

Figure 5.4: Kinematics for the volumetric and constrained mixture approaches. Volumetric growth is described by tracking changes in the local stress free configuration, which is quantified by prescribing evolution equations for the 'growth' deformation $\mathbf{F}_g$. The elastic deformation $\mathbf{F}_e$ is the gradient of the mapping of points from the current stress-free configuration to the current loaded configuration. In the constrained mixture approach, one tracks the evolution of the distribution of mass over all possible combinations of constituent stress free states.

In the traditional volumetric approach, one proceeds by prescribing evolution equations for $\partial\lambda_{ig}/\partial t$. Here, however, we take a different approach; we prescribe the overall rate of change in mass (or volume) with respect to time and prescribe the mechanical state in which new constituents are laid down. Thus, rather than prescribing the evolution of λ_{ig}, we predict these values.

The rate of change of mass of this region may be written as

$$\frac{\partial(dm)}{\partial s} = \sum_j \frac{\partial(dm^j)}{\partial s} = \sum_j \left[\left(\frac{\partial(dm^j)}{\partial s} \right)_{prod} - \left(\frac{\partial(dm^j)}{\partial s} \right)_{rem} \right] \tag{5.20}$$

or equivalently,

$$\frac{\partial \alpha(r,s)}{\partial s} = \sum_j \phi_o^j \frac{\partial \alpha^j(r,s)}{\partial s} = \sum_j \phi_o^j \left[\left(\frac{\partial \alpha^j(r,s)}{\partial s} \right)_{prod} - \left(\frac{\partial \alpha^j(r,s)}{\partial s} \right)_{rem} \right]. \tag{5.21}$$

In general,

$$\left(\frac{\partial \alpha^j}{\partial s} \right)_{rem} = \hat{q}^j \left(\alpha^j(r,s), (\tilde{\sigma}(r,s) - \tilde{\sigma}^h), \cdots; r \right) \tag{5.22}$$

where $\hat{q}^j\left(\alpha^j, \tilde{\sigma} - \tilde{\sigma}^h, \cdots\right)$ allows for the rate to depend on the mass of material present $\alpha^j(s)$, a stress difference(s), $(\tilde{\sigma}(s) - \tilde{\sigma}^h)$, where $\tilde{\sigma}(s)$ is some stress measured relative to its homeostatic value, $\tilde{\sigma}^h$, amongst other factors. Because $\partial\alpha^j/\partial s$, $\left(\partial\alpha^j/\partial s\right)_{prod}$, and $\left(\partial\alpha^j/\partial s\right)_{rem}$ are related through (20), we must prescribe two of these three rates to specify fully the kinetics of turnover. Let us prescribe the net growth rate of *j*, in general, as

$$\frac{\partial \alpha^j}{\partial s} = \hat{g}^j \left(\alpha^j(r,s), (\tilde{\sigma}(r,s) - \tilde{\sigma}^h), \cdots; r \right). \tag{5.23}$$

Thus, the rate of production of *j* is

$$\left(\frac{\partial \alpha^j}{\partial s} \right)_{prod} = \hat{q}^j(r,s) - \hat{g}^j(r,s). \tag{5.24}$$

For our illustrative examples, we let

$$\hat{q}^j(r,s)=\alpha^j(r,s)\left(k_B^j+q^j(\mathbf{T},\tau_w)\right) \quad \text{and} \quad \hat{g}^j(s)=\alpha^j(s)g^j(\mathbf{T},\tau_w) \tag{5.25}$$

where k_B is a constant that yields a 'basal' rate of constituent turnover and we let

$$q^j(r,s)=a_{q1}^j\sqrt{\left(\frac{T_{act}(s)}{T_B}-1\right)^2}\left[a_{q2}^j\sqrt{\left(\frac{T_{\theta\theta}(r,s)}{T_{\theta\theta}^T}-1\right)^2}+1\right] \quad \text{and} \tag{5.26}$$

$$g^j(s)=a_{g1}^j\left[\left(\frac{T_{act}(s)}{T_B}-1\right)+a_{g2}^j\left(\frac{\langle T_{\theta\theta}\rangle}{\langle T_{\theta\theta}^T\rangle}-1\right)\right]\left[a_{g3}^j\left(\frac{T_{\theta\theta}(r,s)}{T_{\theta\theta}^T}-1\right)+1\right]; \tag{5.27}$$

here a_{q1}^j, a_{q2}^j, a_{g1}^j, a_{g2}^j and a_{g3}^j are kinetic parameters. Thus, we hypothesize that the rates of turnover and growth are mediated by mean and local circumferential stress and degree of smooth muscle activation. Constituent removal (i.e., turnover) is mediated by the absolute value of the difference of muscle activation and circumferential stress from basal values and reaches a basal rate when T_{act} is restored. Thus, increases or decreases in these values result in increased turnover. Growth (i.e., net change in mass) is mediated by the muscle activation parameter T_{act}, the mean circumferential stress $\langle T_{\theta\theta}\rangle = P(s)a(s)/h(s)$, and local circumferential stress $T_{\theta\theta}$. The terms in the first set of square brackets in equation (5.27) are not a functions of position while the first term in the second set of brackets is a function of position. Steady state is achieved when the terms in the first set of square brackets reach zero; the term in the second set of square brackets serves to control local differences in stress-mediated growth across the wall.

The rate of change of mass density of each constituent, $\dot{m}^j$, is related to α^j and

α via the relation

$$\dot{m}^j = \frac{d}{ds}\left(\frac{dm^j}{dv}\right) = \frac{d}{ds}\left(\frac{\alpha^j}{\alpha}\frac{dm_o^j}{dv_o}\right) = \rho_o \frac{d}{ds}\left(\frac{\alpha^j}{\alpha}\right). \tag{5.28}$$

Thus, $\dot{m}^j$ is proportional to the rate of change of α^j/α.

Mechanical State of Produced and Removed Material

In biological tissue, material is produced and removed in the loaded configuration, under stress and strain; thus, in our simulations, material is laid down in the in vivo, loaded configuration under stress and strain. In particular, we assume that the new material gets laid down in a homeostatic state of strain.

For growth and turnover of elastin and smooth muscle, we adopt the approach of Gleason and Humphrey (50). Briefly, as new material is produced, we require constituent *j* to be deposited via the homeostatic distribution $\Lambda_h^j(\tilde{\lambda}_\theta, \tilde{\lambda}_z)$. Rather than prescribing the functional form of $\Lambda_h^j(\tilde{\lambda}_\theta, \tilde{\lambda}_z)$, we prescribe the functional form of the distribution of natural configurations$R_h^j(\tilde{R}, \tilde{L}; r, s)$ that results from laying down new material with the distribution of stretches $\Lambda_h^j(\tilde{\lambda}_\theta, \tilde{\lambda}_z)$ in the (known) loaded configuration. Although $\Lambda_h^j(\tilde{\lambda}_\theta, \tilde{\lambda}_z)$ is independent of time, $R_h^j(\tilde{R}, \tilde{L}; r, s)$ depends on *s* because the state $(2\pi r(s_p), \ell(s_p))$ wherein it is produced depends on *s*. We let $R_h^j(\tilde{R}, \tilde{L}; r, s)$ be described by a Beta probability distribution function, with independent variables $\tilde{R}$ and $\tilde{L}$, as

$$R_h^j(\tilde{R}, \tilde{L}; r, s) = \left(\frac{\left(\tilde{R} - R_{min}^j(r,s)\right)^{p_A^j - 1}\left(R_{max}^j(r,s) - \tilde{R}\right)^{q_A^j - 1}}{B\left(p_A^j, q_A^j\right)\left(R_{max}^j(r,s) - R_{min}^j(r,s)\right)^{p_A^j + q_A^j - 1}}\right)\left(\frac{\left(\tilde{L} - L_{min}^j(s)\right)^{p_L^j - 1}\left(L_{max}^j(s) - \tilde{L}\right)^{q_L^j - 1}}{B\left(p_L^j, q_L^j\right)\left(L_{max}^j(s) - L_{min}^j(s)\right)^{p_L^j + q_L^j - 1}}\right) \tag{5.29}$$

where p_A^j, q_A^j, p_L^j, and q_L^j are shape parameters, $B(\cdot,\cdot)$ is the Beta function, $R_{min}^j(r,s) = \overline{R}^j(r,s) - \Delta R^j/2$, $R_{max}^j(r,s) = \overline{R}^j(r,s) + \Delta R^j/2$, $L_{min}^j(s) = \overline{L}^j(s) - \Delta L^j/2$, and $L_{max}^j(s) = \overline{L}^j(s) + \Delta L^j/2$. $\overline{R}^j$ and $\overline{L}^j$ are mean values of the natural configurations, and ΔR^j and ΔL^j are the widths of the distribution. If we know the current state $(r(s_p), l(s_p))$, we can prescribe the mean natural configurations of the distribution as

$$\bar{R}^j(s_p) = \frac{r(s_p)}{\lambda_\theta^j\big|_h} \quad \text{and} \quad \bar{L}^j(s_p) = \frac{\ell(s_p)}{\lambda_z^j\big|_h}, \tag{5.30}$$

where $\lambda_\theta^j\big|_h$ and $\lambda_z^j\big|_h$ are the mean value of the preferred homeostatic stretch distribution.

For collagen, we let the fibers be laid down at a homeostatic distribution of fiber angles described via a sum of normal distribution functions, given as

$$\mathrm{A}(\tilde{\omega}) = \left[\frac{1}{2\sum_p a_p}\right]\sum_p \frac{a_p}{\sigma_p\sqrt{2\pi}}\sum_{n=1}^{2}\left\{\exp\left[\frac{-(\tilde{\omega}+(-1)^n\mu_p)}{2\sigma_p^2}\right]+\exp\left[\frac{-(\tilde{\omega}+(-1)^n(\mu_p-180)}{2\sigma_p^2}\right]\right\} \tag{5.31}$$

where $\tilde{\omega} \in [0,90°]$ is the angle between a fiber and the *z*-axis in the loaded configuration, and μ_p and σ_p are the mean and standard deviation of normal distribution p. In addition, we will assume that at each fiber angle, $\tilde{\omega}$, the fibers are laid down at a homeostatic distribution of stretches, $\Lambda_h^c(\tilde{\lambda}_f, \tilde{\omega}; s)$. As in the case for elastin and smooth muscle, rather than prescribing the distribution of *in vivo* stretches and mapping these stretches back to a reference state, we will simply prescribe the distribution of fiber lengths ($d\widetilde{\Gamma}$) in the reference state; let this distribution be denoted as $\mathrm{B}(d\tilde{\Gamma}, \tilde{\omega}; r)$, via a Beta distribution function, as

$$\mathrm{B}(d\tilde{\Gamma},\tilde{\Omega};s)=\left(\frac{(d\tilde{\Gamma}-d\Gamma_{min}(\tilde{\omega}))^{p^c(\tilde{\omega})-1}(d\Gamma_{max}(\tilde{\omega})-d\tilde{\Gamma})^{q^c(\tilde{\omega})-1}}{B(p^c(\tilde{\omega}),q^c(\tilde{\omega}))(d\Gamma_{max}(\tilde{\omega})-d\Gamma_{min}(\tilde{\omega}))^{p^c(\tilde{\omega})+q^c(\tilde{\omega})-1}}\right) \tag{5.32}$$

where we recall that $\tilde{\omega}=\tilde{\omega}(\tilde{\Omega};s)$, $p^c(\tilde{\omega})$ and $q^c(\tilde{\omega})$ are shape parameters, $d\Gamma_{max}(\tilde{\omega},s)$ and $d\Gamma_{min}(\tilde{\omega},s)$ are the maximum and minimum values of $d\tilde{\Gamma}$ (i.e., $\mathrm{B}(d\tilde{\Gamma},\tilde{\Omega};s)=0$ for $d\tilde{\Gamma}>d\Gamma_{max}$ and $d\tilde{\Gamma}<d\Gamma_{min}$d), and $B(\cdot,\cdot)$ is the Beta function. Note, $d\Gamma_{max}=d\Gamma_{mean}+\Delta d\Gamma/2$ and $d\Gamma_{min}=d\Gamma_{mean}-\Delta d\Gamma/2$, where $d\Gamma_{mean}$ is the mean value and $\Delta d\Gamma$ the width of the $d\tilde{\Gamma}$ distribution function.

The distribution of mass over all combinations of fiber angle and fiber stretch may be given as

$$\hat{\mathrm{R}}^j(\tilde{\Gamma},\tilde{\Omega};r,s)=\mathrm{A}^j(\tilde{\omega}(\tilde{\Omega});r,s)\mathrm{B}^j(\tilde{\Gamma},\tilde{\Omega};r,s) \tag{5.33}$$

This distribution function has the properties

$$\hat{\mathrm{R}}^j(\tilde{\Gamma},\tilde{\Omega})>0 \quad \forall\,\omega,\lambda_f \quad \text{and} \quad \iint_{\tilde{\Gamma},\tilde{\Omega}}\hat{\mathrm{R}}^j(\tilde{\Gamma},\tilde{\Omega})\frac{\partial\tilde{\omega}}{\partial\tilde{\Omega}}d\tilde{\Omega}d\tilde{\Gamma}=1. \tag{5.34}$$

Notice that the 'homeostatic' distribution function $\hat{\mathrm{R}}^c(\tilde{\Gamma},\tilde{\Omega};r,s)$ captures (qualitatively) the fiber orientations observed in these vessels, as well as the observation that different fibers become loaded (i.e., recruited) in different loaded configurations (Figure 5.5).

(a)

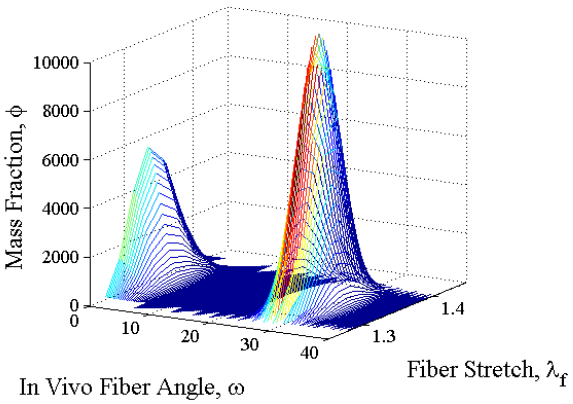

(b)

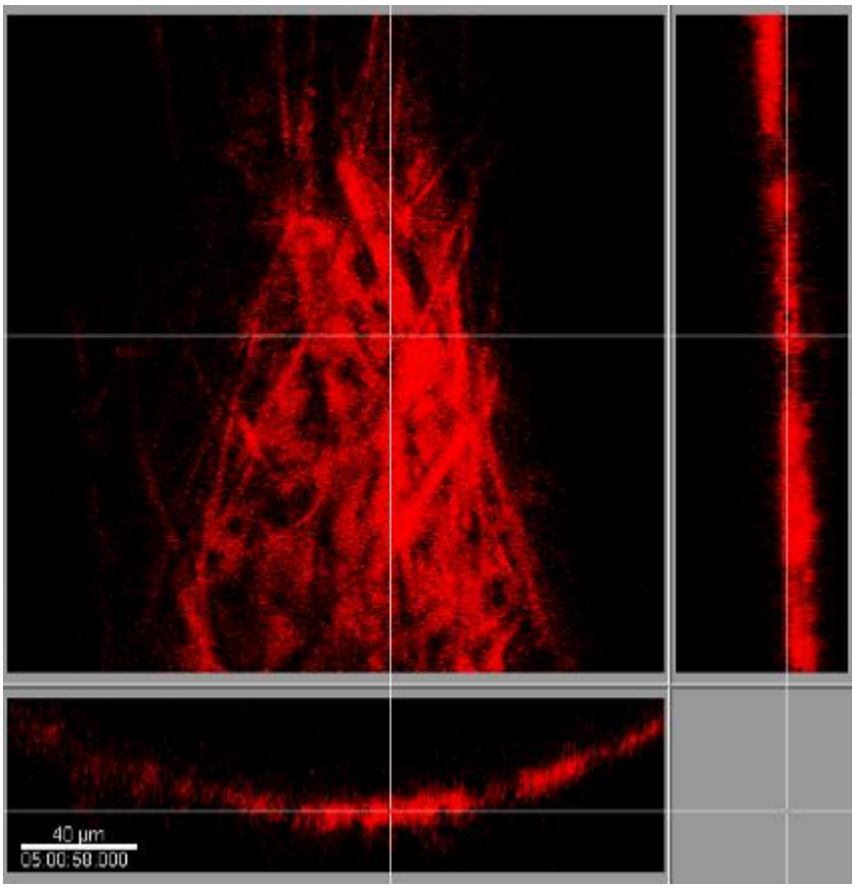

Figure 5.5: (a) Distribution of *in vivo* collagen fiber angles and stretches, (b) Confocal microscopy image of collagen fibers from a mouse carotid artery under in vivo loading conditions

Illustrative Results

The governing equations are the kinematic equations (5.3), the constitutive equations (5.9), (5.12), and (5.13-5.16), equilibrium equations (5.10) and (5.11), the kinetic equations (5.23-5.27) which describe the rate of constituent turnover and growth, and equations (5.29), (5.30), and (5.31-5.33) which describe the mechanical state of newly produced material. Based on data from mouse carotid arteries,(53) we prescribe the initial mean values (over the cardiac cycle): the *in vivo* inner radius a_o = 250 μm, *in vivo* thickness h_o = 24.16 μm, and *in vivo* axial length $l_o = 2\pi a_o$ = 1.57 mm. Structural and material parameters were determined by fitting this constitutive model to experimental data from mouse common carotid arteries from Gleason et al.(53), following the methods described in Hansen et al. (56). The structural parameters for the mechanical state in which constituents are laid down are $\lambda_\theta^e\big|_h$ = 1.98, $\lambda_z^e\big|_h$ = 2.25, $\lambda_\theta^m\big|_h$ = 1.72, $\lambda_z^m\big|_h$ = 1.88, $\lambda_f^c\big|_h$ = 1.34, $\overline{\omega}_1 = 0°$, and $\overline{\omega}_2 = 28°$, and the material parameters are b^e = 103.95 kPa, b^m = 0.362 kPa, b_1^m = 10.15 kPa, b_2^m = 0.402, b_1^c = 751.34 kPa, b_2^c = 1.332, T_B = 363 Pa kPa, λ_M = 2.1, and λ_0 =0.8. Pressure-diameter, axial force-pressure, and mid-wall stress-strain plots show that these material parameters capture the salient feature of large arteries (Figure 5.6). Kinetic parameters used for each simulation are listed below. We solved this system of equations numerically by discretizing the radius and using an implicit time-step implemented in MATLAB 7.4. We also discretized the space of all possible natural configurations $\tilde{\kappa}_n$ (i.e., the $\tilde{R} - \tilde{L}$-space for elastin and muscle and the $\tilde{\Gamma} - \tilde{\Omega}$-space for collagen).

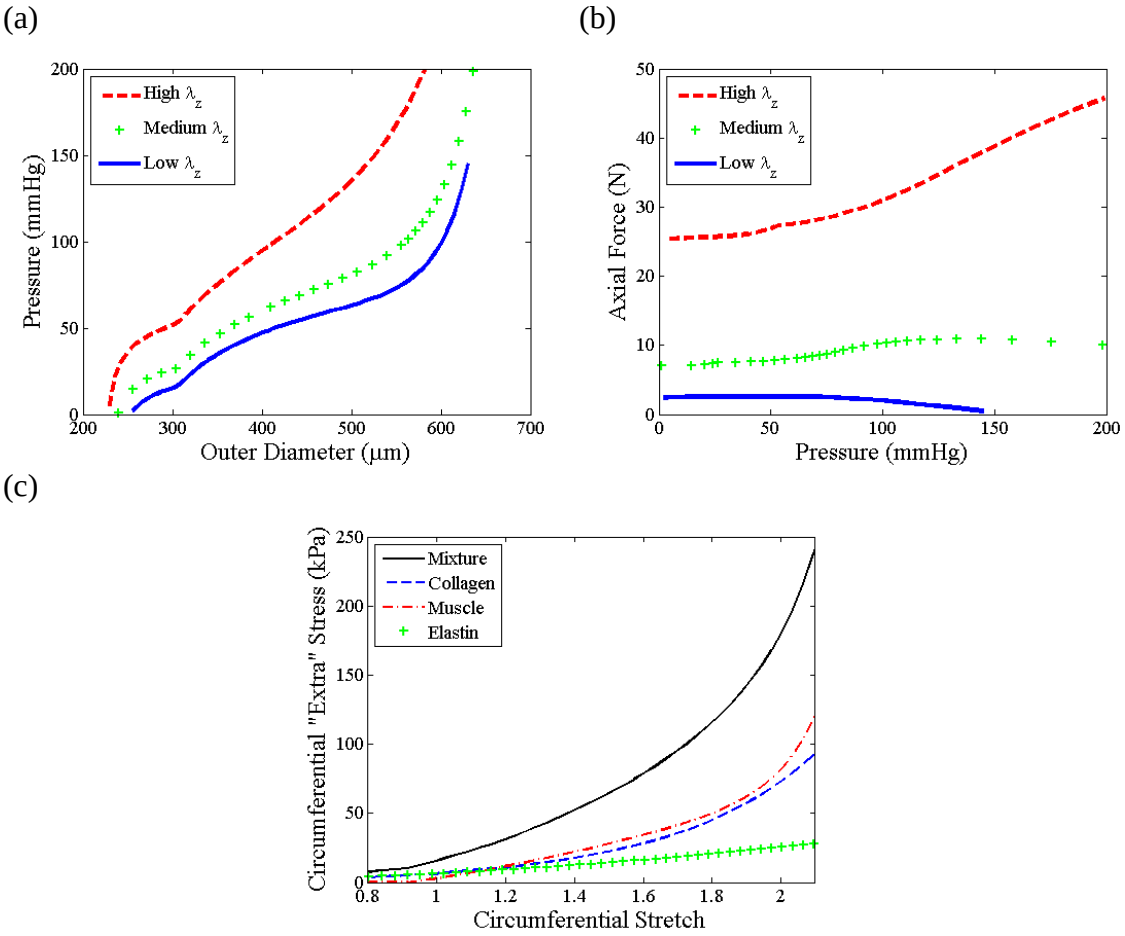

Figure 5.6: (a) Simulated results from a typical pressure-diameter test of a typical mouse carotid artery, (b) simulated axial force-pressure test, and (c) mean circumferential stress strain data for mixture and for constituents using proposed constitutive models with prescribed structural and material parameters.

Given the initial loaded configuration $r(0)$ and ℓ_o, we calculated values for the initial distribution functions $\Phi^j(\tilde{\kappa}_n, r, s=0)$ (by setting $r(s_p) = r(0)$ and $\ell(s_p) = \ell_o$ in equations (5.29), (5.30), and (5.33)), the deformation gradient, and the components of stress for each constituent at each node in each discretized 2-D space (i.e., $\tilde{R} - \tilde{L}$-space and $\tilde{\Gamma} - \tilde{\Omega}$-space) at each radial location. The components of the 'extra' stress were calculated by integrating the second term on the right hand side of equation (5.9); for

elastin and muscle equation (5.9) represents a surface integral over $\tilde{R}$ and $\tilde{L}$; for collagen equation (5.9) becomes a double integral over $\tilde{\Gamma}$ and $\tilde{\Omega}$. The Lagrange multiplier was calculated via equation (5.12) and the total Cauchy stress was calculated via equation (5.9).

At time $s = 0^+$, we imposed the change in applied loads to $P(s) = \beta P_o$, $Q(s) = \varepsilon Q_o$, and $l(s) = \delta l_o$. To impose the assumption that the vessel aims to restore wall shear stress via vasoregulation, we first determined the vasoactive range of radii at any time *s*, by solving equation (5.10) for the inner radius with $T_{act} = T_{act}^{max}$ and $T_{act} = 0$; this yields the maximally constricted and maximally dilated inner radii (r_i^{min} and r_i^{max}), respectively. The ('target') inner radius that restores wall shear stress is $r_i^{targ} = \varepsilon^{1/3} r_i(0^-)$, as shown in Gleason et al. (51). If $r_i^{targ} > r_i^{max}$ then the maximal dilation is not sufficient to restore wall shear stress, and we set $T_{act}(s) = 0$ and $r_i(s) = r_i^{max}$. If $r_i^{targ} < r_i^{min}$ then the maximal constriction is not sufficient to restore wall shear stress, and we set $T_{act}(s) = T_{act}^{max}$ and $r_i(s) = r_i^{min}$. If $r_i^{targ} \in [r_i^{min}, r_i^{max}]$, then $T_{act}(s) \in [0, T_{act}^{max}]$; in this case, we set $r_i(s) = r_i^{targ}$ and solved equation (5.10) for $T_{act}(s)$. Given this new configuration and activation, we calculated $\mathbf{T}(s)$via equation (5.9) with equation (5.12).

Given the calculated values for $T_{\theta\theta}(s)$ and $T_{act}(s)$, the amount of (normalized) mass produced ($d\alpha_{prod}^j(s)$) and removed ($d\alpha_{rem}^j(s)$) for the next time step (*ds*) was calculated via equations (5.21-5.26). The new distribution of mass at each radial location is given as,

$$R^j(\tilde{\kappa}_n; r, s+ds) = \frac{\left(\alpha^j(s) + da^j_{rem}(s)\right) R^j(\tilde{\kappa}_n; r, s) + d\alpha^j_{prod}(s) R^j_h(\tilde{\kappa}_n; r, s)}{\alpha^j(s+\Delta s)} \quad (5.35)$$

where $R^j(\tilde{\kappa}_n; r, s)$ is calculated via equations (5.29) for elastin and muscle, equation (5.33) for collagen, and where the configuration in which the material is produced ($r(s_p)$ and $\ell(s_p)$) is the current configuration ($r(s)$ and $\ell(s)$). Finally, $\Phi^j(\tilde{\kappa}_n; r, s+ds) = \phi^j(r, s+ds) R^j(\tilde{\kappa}_n; r, s+ds)$. Next, we let $s = s + ds$, proceeded to the next time step, and repeated these steps for a specified number of time-steps.

Altered Flow

For all altered flow simulations, we let ε = 2.0 and $\beta = \delta$=1.0; that is, a two-fold increase in flow with no change in pressure or axial length. We considered two illustrative cases: one in which all constituents turnover at equal rates (EQUAL RATES) and one in which constituents are turned over at representative physiological rates (PHYSIOLOGICAL RATES).

Equal Rates

We let $k^e_b = k^m_b = k^c_b = 0.1$, $a^e_{q1} = a^m_{q1} = a^c_{q1} = 1.0$, $a^e_{q2} = a^m_{q2} = a^c_{q2} = 1.0$, $a^e_{g1} = a^m_{g1} = a^c_{g1} = 0.1$, $a^e_{g2} = a^m_{g2} = a^c_{g2} = 10.0$, and $a^e_{g3} = a^m_{g3} = a^c_{g3} = 0.1$. Following altered flow, smooth muscle cell relaxation (via reduction in T_{act}) caused the vessel to dilate; c.f., $r_i(s)/r_i(0^-)$ at $s = 0^-$ before vasodilation and $s = 0^+$ after dilation (Figure 5.7a). The vessel wall thinned with dilation (via incompressibility), and the total circumferential and axial stress across the vessel wall increased (Figures 5.7b and 5.7c). The growth is governed by $(T_{act}/T_B - 1)$, $\left(\langle T_{\theta\theta}(s)\rangle / T^T_{\theta\theta} - 1\right)$, and $\left(T_{\theta\theta}(r,s)/T^T_{\theta\theta} - 1\right)$ via equations (5.26) and (5.27). Following dilation, SMC were fully relaxed (i.e., T_{act} =0

and $(T_{act}/T_B - 1) = -1)$, and the shear stress was not completely restored to the homeostatic value (Figure 5.8a). Also at $s = 0^+$, $\left(\langle T_{\theta\theta}(s)\rangle/T^T_{\theta\theta} - 1\right) = 0.15$ (Figure 5.8b). Since a^j_{g2}=10.0, the term in the first set of square brackets in equation (27) equaled 0.5 at $s = 0^+$. The local stress increased to different extents at different locations across the vessel wall; thus, the term in the second set of square brackets in equation (27) varied across the wall, decreasing monotonically from the inner to outer wall (see Figure 5.7b). Thus, the net effect of $(T_{act}/T_B - 1)$, $\left(\langle T_{\theta\theta}(s)\rangle/T^T_{\theta\theta} - 1\right)$, and $\left(T_{\theta\theta}(r,s)/T^T_{\theta\theta} - 1\right)$ is that g^j was positive immediately following dilation, and the vessel began to accumulate mass to different extents at different radial locations (Figure 5.8c). Note that mass accumulation can be delayed by decreasing a_{g2}; this could cause some initial atrophy before growth occurs. The rate of turnover is governed by $(T_{act}/T_B - 1)$ and $\left(\langle T_{\theta\theta}(s)\rangle/ T^T_{\theta\theta} - 1\right)$, according to equation (5.26); following vasodilation, the rate of turnover increased ~2.7 fold, but varied across the wall. As the vessel wall grew and existing constituents were replaced with new constituents with new natural configurations, the vessel wall radius continued to increase. This increased radius and decreased thickness caused the mean and local wall stresses to be increased further. At $s = 3.1$, the vessel reached the 'target' radius of $a(s) = 1.26a_o$, and the smooth muscles began to contract. As growth and remodeling proceed, T_{act} asymptotically approached its basal value T_B. The total thickness increased to $h/h_o = \varepsilon^{1/3} = 1.26$. Locally, however, since rates of growth varied with radius, there were different levels of local thickening at different locations (see Figure 5.8a); thickening was slightly higher at inner versus outer wall locations. The mean and local values of the circumferential and axial stresses were

restored to initial values. Mean axial stress and mean circumferential stress both reached a maximum value upon increase in flow at $s=0^+$, and then asymptotically decreased to initial values.

(a) (b)

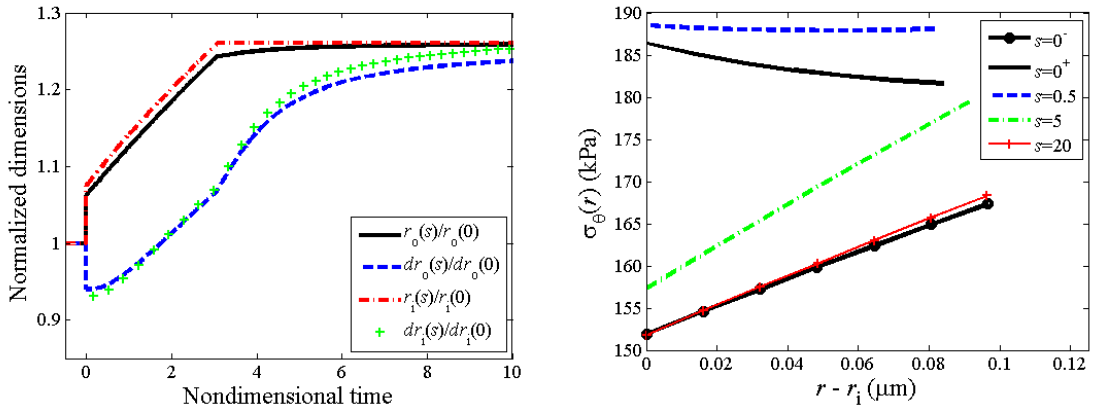

(c)

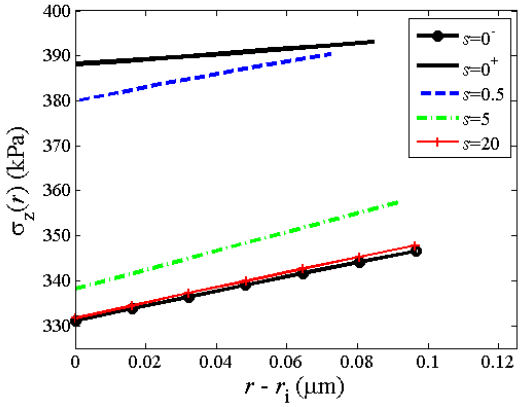

Figure 5.7: Flow: Equal Rates. (a) Normalized radius and local thickness at the inner and outer wall versus time. (b) Circumferential stress distribution and (c) axial stress distribution at different time-points during growth and remodeling.

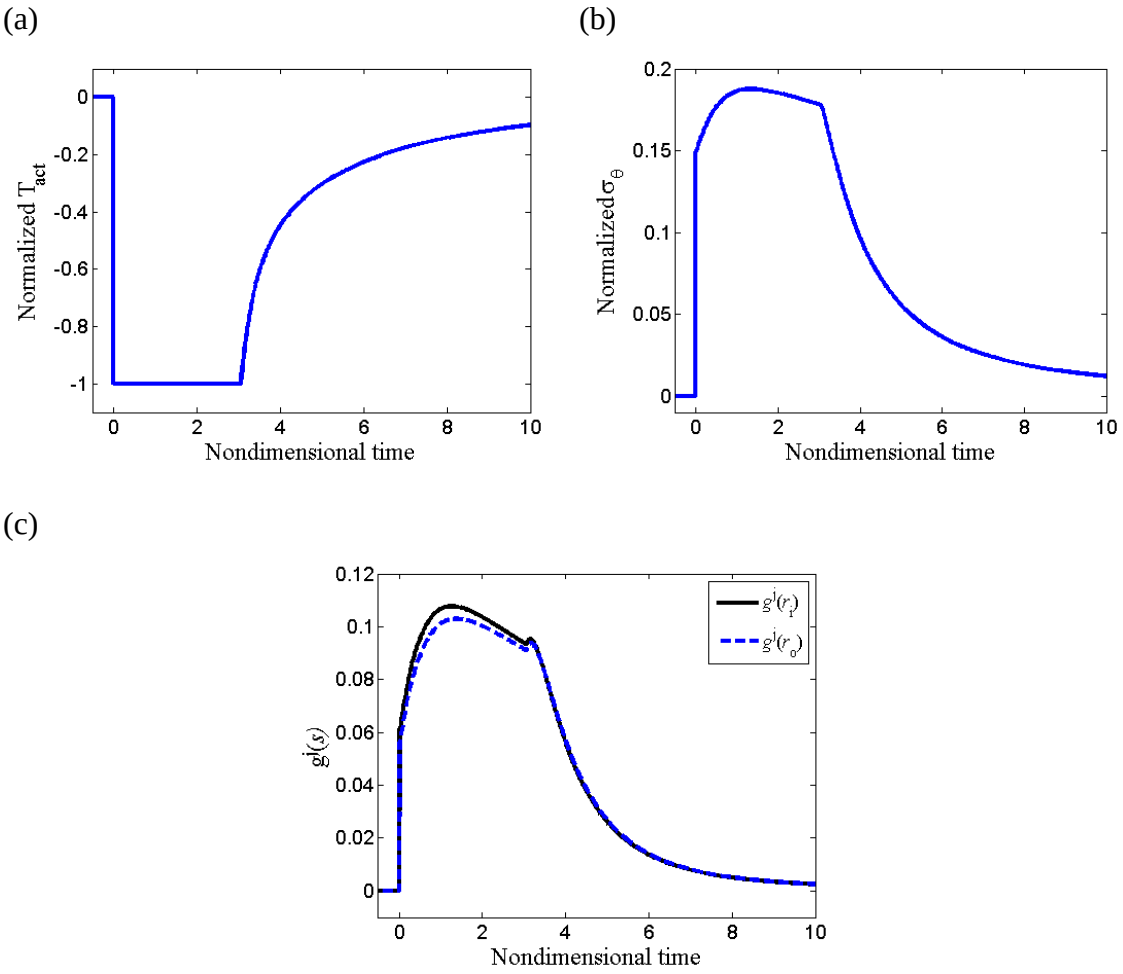

Figure 5.8: Flow: Equal Rates. (a) Normalized muscle activation (T_{act}/T_B - 1), (b) mean circumferential stress, and (c) growth rate versus time.

Prior to dilation, the stretches in each constituent were at their homeostatic values. For example, at $s = 0^-$, the stretches in the muscle were distributed over the ranges $\lambda_\theta^m \in [1.71, 1.73]$ and $\lambda_z^m \in [1.87, 1.89]$ (Figure 5.9a). Following dilation, as the radius increased the circumferential stretch in muscle increased to $\lambda_\theta^m \in [1.83, 1.85]$ (Figure 5.9b); since there is no change in axial length with dilation, the axial stretches remain unchanged. As constituent turnover ensued, newly formed constituents were laid down at the homeostatic values of these stretches. For muscle, newly formed material were laid

down at $\lambda_\theta^m \in [1.71, 1.73]$ and $\lambda_z^m \in [1.87, 1.89]$; thus, at time points when both existing and newly form constituents co-exist, the total mass of muscle became distributed over all possible combinations of in-plane stretches in a bi-modal fashion (see Figures 5.9c and 4.9d). Note too, that material formed immediately after dilation, when $a(s) = 1.07a_o$, and laid down at the homeostatic stretches becomes stretched further as the vessel continued to increase its radius to $a(s) = 1.26a_o$. Eventually, as the vessel reached the configuration that restores wall shear stress and is held constant while constituent turnover continued, material at stretches outside of the homeostatic stretches were eventually replaced with material laid down at the homeostatic stretches (Figure 5.9e and 5.9f).

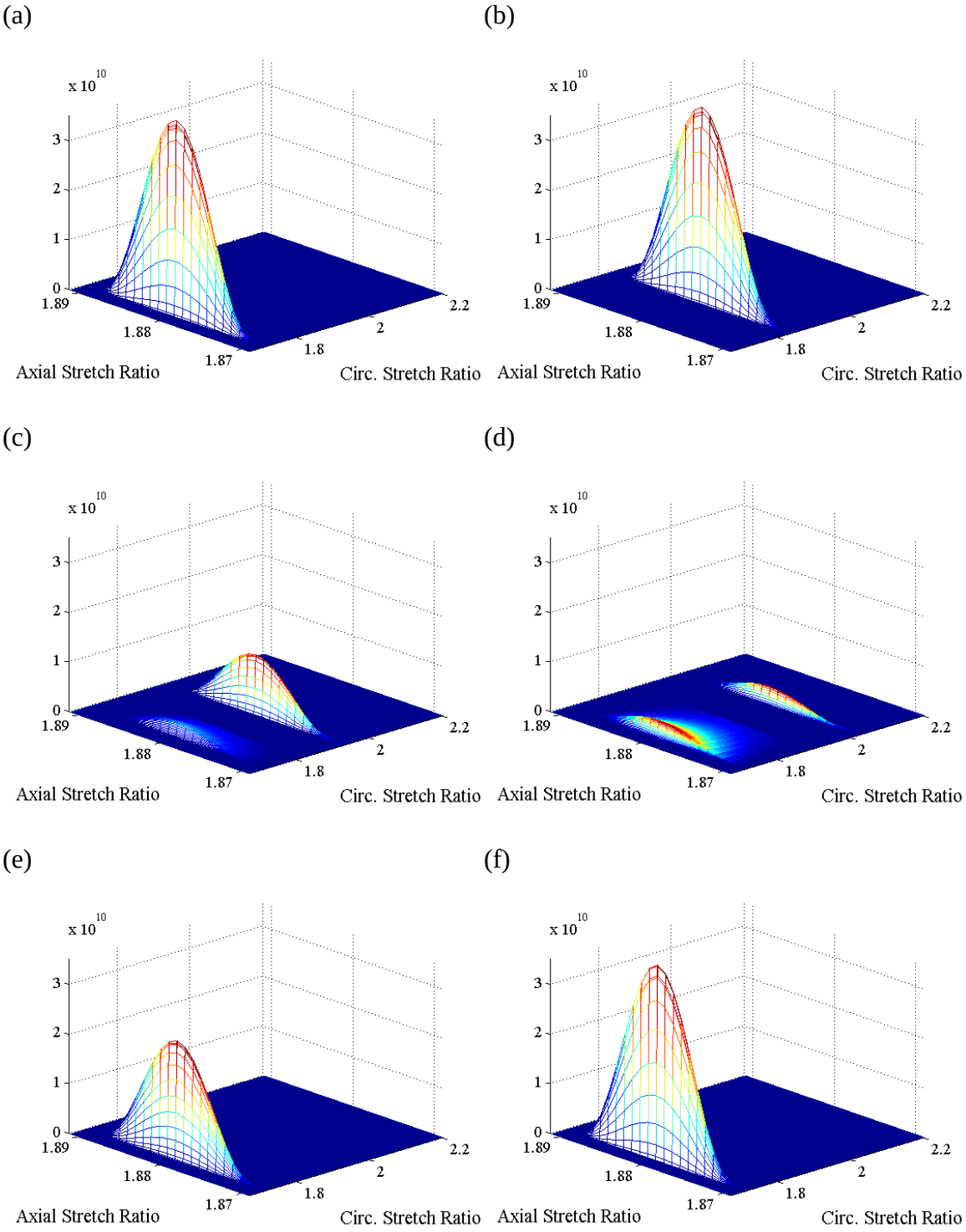

Figure 5.9: Flow: Equal Rates. Surface describing how muscle is distributed over all possible sets of circumferential and axial stretches at (a) $s = 0^-$, (b) $s = 0^+$, (c) $s = 0.86$, (d) $s = 1.73$, (e) $s = 4.92$, (f) $s = \infty$.

Similarly, the distribution of collagen over all possible combinations of fiber angle $\tilde{\omega}$ and fiber stretch $\tilde{\lambda}_f$ in the *in vivo* configuration evolved with growth and remodeling. Initially, the mean fiber angles were $\bar{\omega}_1 = 0°$, and $\bar{\omega}_2 = 28°$ and the mean stretch of these fibers equaled the homeostatic value $\lambda_f^{c1} = \lambda_f^{c2} = 1.34$ (not shown). Upon vasodilation, the fiber angle and fiber stretch ratio deformed to $\bar{\omega}_2 = 29.7°$ and $\lambda_f^{c2} = 1.36$; there was no change in $\bar{\omega}_1$ and since there was no change in vessel length, there was no change in λ_f^{c1}. As new collagen was produced, however, it was laid down at the homeostatic fiber angle and fiber stretch; thus, a bimodal distribution of (between $\bar{\omega}_2 = 28°$ and $\bar{\omega}_2 = 29.7°$, in addition to the peak at $\bar{\omega}_1 = 0°$) resulted. Eventually, as the vessel reached the configuration that restored wall shear stress and was held constant and constituent turnover continued, material at fiber orientations and fiber stretches outside of the homeostatic stretches were eventually replaced with material laid down at the homeostatic fiber orientations and fiber stretches.

Physiological Rates

In vivo, the rates of growth and turnover of elastin, collagen, and muscle vary significantly. We know, for example, that the rate of turnover of smooth muscle is significantly higher than that of collagen, but that the ratio of total mass of collagen to that of muscle remains nearly constant. This may be simulated in our model by setting $a_{q1}^m = 10a_{q1}^c$, still requiring that $a_{g1}^m = a_{g1}^c$. We also know that in adult vertebrates, the rate of production and turnover of elastin is very small compared to that of muscle and collagen. This may be simulated in our model by setting $k_B^e = a_{q1}^e = a_{g1}^e \sim 0$. Thus, we let

$k_B^e = a_{q1}^e = a_{g1}^e = 0$, $k_B^m = k_B^c = 0.1$, $a_{q1}^m = 10$, $a_{q1}^c = 1.0$, $a_{q2}^m = a_{q2}^c = 1.0$, $a_{g1}^m = a_{g1}^c$ = 0.1, $a_{g2}^m = a_{g2}^c = 10.0$, and $a_{g3}^m = a_{g3}^c = 1.0$. For physiological rates of growth and turnover, the circumferential and axial stresses approach, but did not completely restore initial values (Figure 5.10). In addition, the thickness initially decreased, then thickened to h/h_o =1.24, which is less than the 'target' value of $\varepsilon^{1/3} = 1.26$. Thus, neither $\langle T_{\theta\theta}(s) \rangle$ nor $T_{act}(s)$ were restored and remained 2.0% above and 19% below homeostatic values. The mass fractions of collagen, muscle, and elastin varied both with time and radial location, with the greatest increase in collagen and muscle mass fraction at inner versus outer wall locations (not shown). Therefore, in addition to non-uniform thickening, in this case, the vessel evolved from a homogeneous material to a heterogeneous material.

(a)

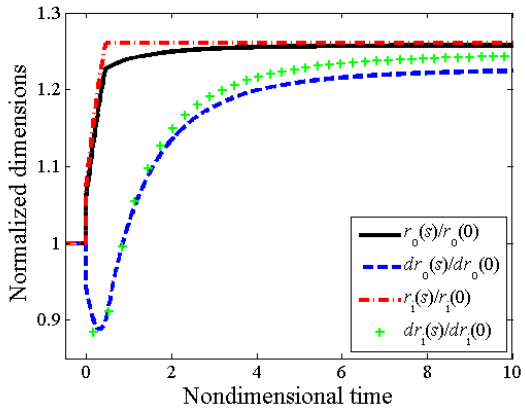

(b)

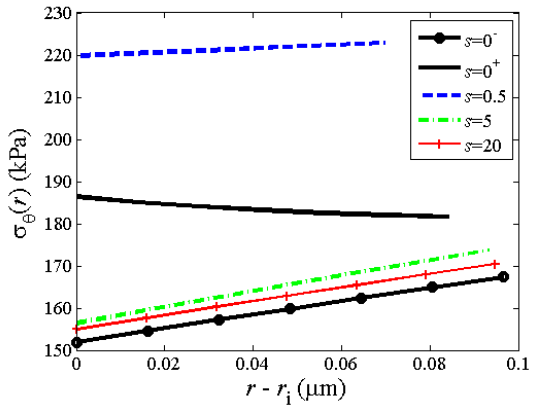

(c)

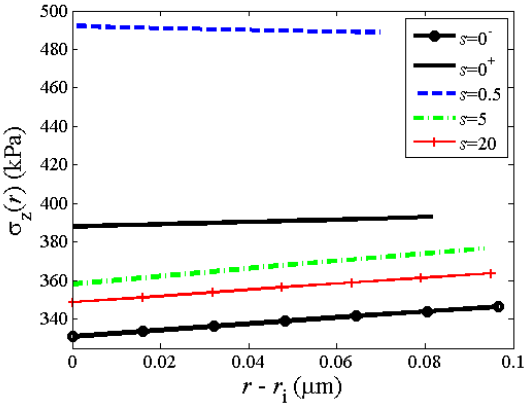

Figure 5.10: Flow: Physiological Rates. (a) Normalized radius and local thickness at the inner and outer wall versus time. (b) Circumferential stress distribution and (c) axial stress distribution at different time-points during growth and remodeling.

Altered Pressure

For this altered pressure simulation, we let β=2.0 and $\varepsilon = \delta$ =1.0; that is, a two-fold increase in pressure with no change in flow or axial length. We performed these simulations at the physiological turnover rates. Following the increase in pressure, the vessel passively distended to enlarge the lumen and simultaneously (within minutes), the smooth muscle activation increased to $T_{act} = T_{act}^{max}$ (with $(T_{act}/T_B - 1) = 1.9$, Figure 5.11a) due to the lower shear stress that occurs due to the increase in radius and

unchanging flow rate. For this large increase in pressure, the maximum smooth muscle activation was not sufficient to restore the inner radius to the 'target' value that restores the wall shear stress (Figure 5.12a). The increased pressure increased the *in vivo* radius and decreased the *in vivo* thickness producing a significant increase in mean and local circumferential stress (Figure 5.11b and 5.12b). The net effect of increased muscle activation and increased mean and local circumferential stress, as governed by equation (5.27), was a step increase in growth followed by a monotonic decrease with time. As growth and remodeling proceeded, T_{act} asymptotically approached its basal value T_B. The circumferential and axial stresses were restored towards initial values with the mean axial stress remaining higher than the original value. The total thickness increased to h/h_o= 2.0, which is the value required by Laplace's Law to restore the mean circumferential stress. Locally, since rates of growth varied with radius, there were different levels of local thickening at different locations (see Figure 5.12a); thickening was higher at inner versus outer wall locations. This is consistent with the observations of Matsumoto and Hayashi (99) that clearly showed greater thickening on the inner versus outer wall locations. Note that the degree of non-uniform thickening may be controlled by adjusting a_{g3}^{j}, with higher values of a_{g3}^{j} corresponding to a higher degree of non-uniform thickening.

(a)

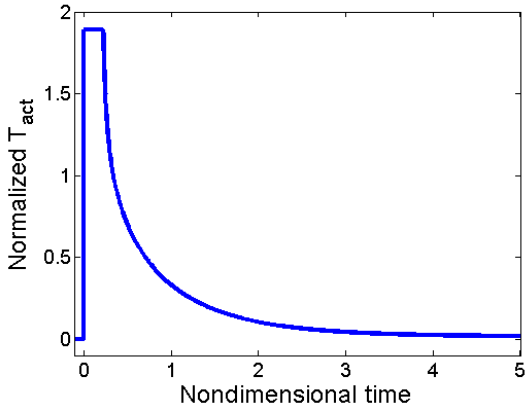

(b)

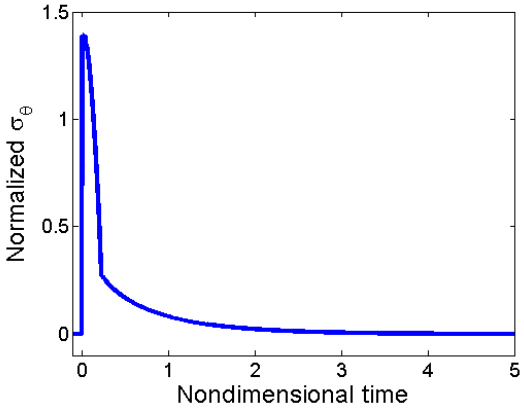

(c)

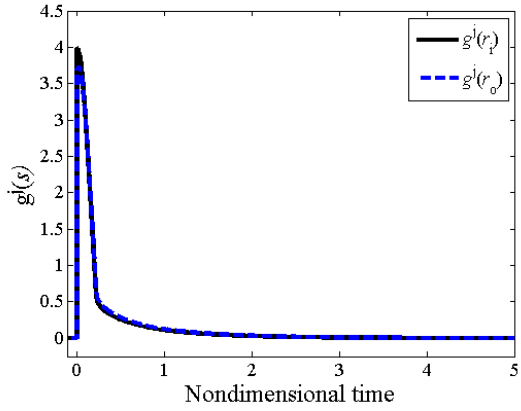

Figure 5.11: Pressure: Physiological Rates. (a) Normalized muscle activation (T_{act} /T_B - 1), (b) mean circumferential stress, and (c) growth rate versus time.

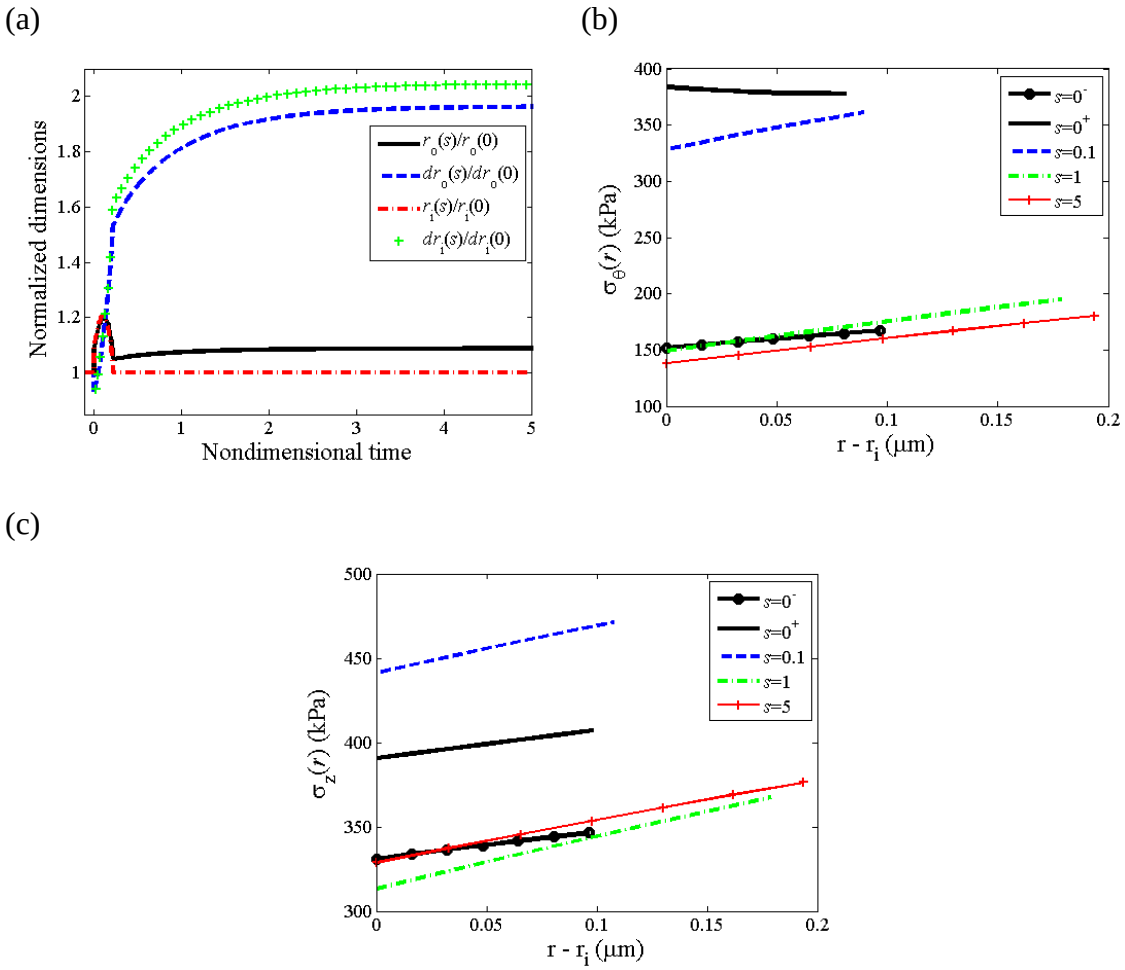

Figure 5.12: Pressure: Physiological Rates. (a) Normalized radius and local thickness at the inner and outer wall versus time. (b) Circumferential stress distribution and (c) axial stress distribution at different time-points during growth and remodeling.

Discussion

We have presented a 3D constrained mixture model for vascular growth and remodeling. This model is capable of describing growth and remodeling in response to alterations in flow and pressure. The mechanical response was modeled via a structurally motivated, rule of mixtures based constitutive equation. One of the utilities of mathematical models is to motivate experimental design; identifying the most insightful experimental protocols and required quantities to be measured. This model has many

parameters and variables that must be quantified via experimental data. While it is difficult to directly measure the kinetic parameters of growth and remodeling, the evolution of mass fractions and fiber orientations may be measured via multiphoton microscopy on live tissue under mechanical loading (see Gleason and Wan (52); Whicker et al. (158)). In addition, it may be possible to quantify, or at least approximate better, natural configurations for individual fibers by evaluating their degree of undulation under various loading scenarios. Changes in mechanical behavior can also be experimentally determined via biaxial biomechanical testing; for a given form of the constitutive equation, material (and structural) parameters may be identified via regression techniques (56). To quantify growth and remodeling, of course, one must determine these quantities at multiple time-points during this process.

A widely applied approach to model soft tissue remodeling employs the concept of *volumetric growth*, put forth by Skalak (129, 131) and extended by many (35, 112, 115, 119, 137-139). In this approach, an original stress-free configuration is allowed to grow into discontinuous (and fictitious) stress-free elements. This growth is defined through the deformation gradient $\mathbf{F}_g$; typically, for the case of remodeling in an axisymmetric tube $\left[\mathbf{F}_g\right] = diag\left\{\lambda_{gr}, \lambda_{g\theta}, \lambda_{gz}\right\}$, where λ_{gi} are growth stretch ratios. The overall deformation gradient is given by $\mathbf{F} = \mathbf{F}_e\mathbf{F}_g$, where $\mathbf{F}_e$ is the gradient of the mapping from the traction-free configuration to an experimentally measured configuration under applied loads (Figure 5.4); for the case of inflation and extension of an axisymmetric tube, $\left[\mathbf{F}_e\right] = diag\left\{\lambda_{er}, \lambda_{e\theta}, \lambda_{ez}\right\}$. To proceed, one must prescribe constitutive equations for the stress ($\mathbf{T}$=$\mathbf{T}$($\mathbf{F}$)) and the rate of growth $\partial\lambda_{gi}/\partial t$ via

evolution equations, which often depend on differences between the current stress and some 'target' value of stress. Whereas the volumetric growth approach may capture some important consequences of growth, we submit that it does not incorporate the underlying remodeling mechanisms. In contrast, microstructurally motivated models are based on the production, removal, and remodeling of individual constituents at different rates and to different extents. Rather than prescribing the evolution of λ_{gi}, these quantities are predicted based on underlying hypotheses of the overall growth, rate of constituent turnover, and mechanical state of newly formed (or newly remodeled) material. In our simulations, we have calculated the growth stretches at basal smooth muscle tone for the case of flow induced remodeling with physiological rates (Figure 5.13). The radial and circumferential growth stretches evolve towards $\varepsilon^{1/3}$; the circumferential growth stretch, however, reaches steady state much earlier than the radial growth stretch. The axial growth stretch remains nearly at λ_{gi}=1. These results are consistent with literature; again, these results are predicted based on the underlying hypotheses of our model, in contrast to volumetric growth models wherein these values are prescribed directly via evolution equations.

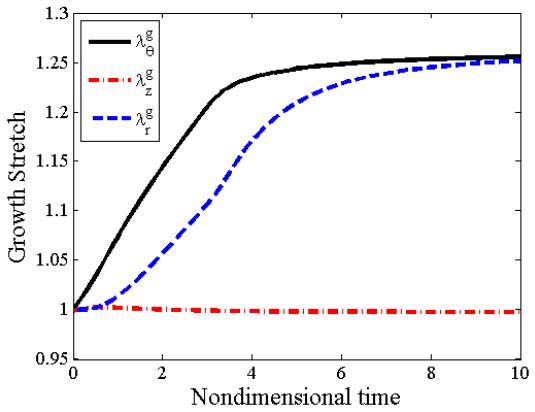

Figure 5.13: Growth stretches λ_{gr}, $\lambda_{g\theta}$ and λ_{gz} predicted for flow induced remodeling under physiological rates.

It has long been postulated that the local remodeling correlates well with the local stresses (99). We present a new functional form for the evolution equations for the growth and turnover of individual structural constituents that depends on the Cauchy stress ($\mathbf{T}$) and the level of muscle activation (T_{act}). Recall that T_{act} is a parameter associated with the degree of muscle activation. Muscle activation is ultimately a function of intracellular calcium concentration but is controlled by many factors including the release of vasoactive molecules such as nitric oxide and endothlin-1 by the endothelium and the myogenic response, amongst other factors. Importantly, nitric oxide is known to inhibit and endothelin-1 is known enhance smooth muscle cell proliferation. Similarly, whereas platelet derived growth factor is known to increase rates of smooth muscle cell proliferation, it is also known to induce smooth muscle cell contraction. Thus, clearly there is a link between signals for vasoregulation and cell proliferation. Similarly, nitric oxide has been shown to downregulate matrix metalloproteinase-9 (MMP-9) expression (165), which suggests a link between vasoregulating proteins and ECM degradation. Taken together, these and many other observations from the literature

clearly support the inclusion of modeling parameters for muscle activation in the growth and turnover of cell and ECM. There is evidence in the literature that supports our claim that the vessel remodels to restore the muscle activation, not the stress, to homeostatic values. For example, Kamiya and Togawa showed that wall shear stress was restored (i.e., $r_i(s) = \varepsilon^{1/3} r_i(0^-)$) in canine carotid arteries at 6-months given an increased flow for ε < 3.5 (76). Many later reports support the finding that wall shear stress is often restored to a target value following a sustained alteration in flow. Results from the literature are less clear whether the mean circumferential stress is likewise restored (i.e., that wall thickness $h(s) = \varepsilon^{1/3} h(0^-)$). For example, Zarins et al. reported that after 6-months of a 9.6-fold increased flow in the iliac artery of an adult monkey (thus, $\varepsilon^{1/3}$ = 2.1) the vessel grew and remodeled such that $r_i(s) = (2.1) r_i(0^-)$, but based on their data (and assuming no changes in axial length) $h(s) = (1.3) h(0^-)$ (168); thus, the radius remodeled to restore wall shear stress (and, thus, the release of vasoactive molecules), but the wall thickness did not remodel to restore the mean circumferential stress. Indeed, their data show that the mean circumferential wall stress after 6-months of elevated flow was 1.6 times that of the initial value; clearly, in this case wall stress was not restored. Our model predicts similar results; namely, that for a large step change in flow, with ε=9.6, the steady state circumferential stress is not restored (data not shown).

In conclusion, we have developed a computational framework to quantify growth and remodeling of blood vessels. We emphasize that these illustrative simulations are but a first step to developing a predictive model for vessel adaptations. Significant experimental data is currently lacking to fully quantify the material and kinetic parameters and validate the underlying hypotheses. In addition, although we present a 3D

model that may incorporate material heterogeneities, we focus our attention on growth and remodeling of the tunic media. There is an ever increasing awareness, however, that the adventitia plays a key role in vascular remodeling, both under physiological and pathophysiological conditions. Thus, further advancement of this computational framework will be to include both medial and adventitial layers, each with a distinct microstructural content and organization, distinct cell types, and therefore, distinct mechanically mediated growth and remodeling responses.

CHAPTER 6

CONSTITUTIVE MODELING OF MOUSE CAROTID ARTERIES USING EXPERIMENTALLY MEASURED MICROSTRUCTURAL PARAMETERS

Introduction

Constitutive relations have long been used to predict the local mechanical environment within biological tissues and to serve as tools for investigating the relationship between biological responses and mechanical stimuli. Early forms of constitutive relations were purely phenomenological while recent constitutive relations for arteries provide a framework for describing both material and structural properties. These models can incorporate parameters that describe microstructural organization such as fiber distributions, fiber angles, fiber crimping, and constituent volume fractions, amongst others. The recently developed technique of imaging the microstructure of a single artery as it undergoes multiple deformations has the potential to provide quantitative structural data that would reduce the number of parameters estimated to ones that are truly experimentally intractable.

In this study, we quantified collagen fiber angle distributions in mouse carotid arteries under various biaxial loading conditions, in parallel with performing cylindrical biaxial biomechanical testing, and used experimentally derived structural data to perform parameter estimation studies. Collagen fibers across the entire wall thickness of the artery were imaged by detection of the second harmonic generation (SHG) signal (172), and a fast fourier transform (FFT) technique was used to calculate fiber angles through the depth of the vessel wall under each loading condition (107). We found that incorporating

an experimentally measured fiber angle in a four fiber model (4) and using an experimentally measured fiber distribution in a distributed fiber model (56) yields similar fitting errors. When using mean estimated parameters to predict the mechanical response of arteries, we found that using a model that described fiber angle distributions using three Gaussian terms yields greater predictive accuracy with lower variances between samples. We also found that deformations between two loading configurations that span the limits of fiber stretch and rotation experienced during a typical biaxial test may be approximated using affine motion transformations with an R-squared value of 0.76 or greater.

Methods

Surgical preparation and vessel isolation

Adult male WT mice (7.7±0.2 weeks old, n=3 on the C57-BL6 X 129/SvEv background were euthanized with an overdose of CO_2. All mice were produced from a breeding pair originally obtained from Dr. Hiromi Yanagisawa (UT Southwestern). Under sterile conditions, both common carotid arteries were excised, placed in physiological saline solution, dissected free of perivascular tissue, and mounted on the glass cannulae of our biomechanical testing device using sterile suture (46). All animal procedures were approved by the Institute Animal Care and Use Committee (IACUC) at the Georgia Institute of Technology.

Biomechanical testing

A custom experimental apparatus was used to perform cylindrical biaxial biomechanical testing and to perform multi-photon confocal microscopy for 3D imaging

of the content and organization of cells and ECM constituents (46). Pressure-diameter (*P*-*d*) data were collected from 0 to 160 mmHg at constant axial extensions, and axial force-length (*f*-ℓ) data were collected over cyclic axial extensions at constant pressures, *P* = 60, 100, and 140 mmHg. Here, $\lambda = \ell / L$ where ℓ is the current length and L is the original unloaded length; ℓ and L were measured as the distance between mounting sutures. The *in vivo* axial stretch ratio was defined as the stretch for which axial force remains nearly constant during the pressurization cycle (24, 140).

Multiphoton Microscopy

Live, freshly isolated, mouse carotid arteries mounted on our bioreactor under controlled transmural pressure and axial stretch were imaged on an LSM 510 META inverted confocal microscope (Zeiss) fitted with a tunable multiphoton laser (Chameleon). The laser reached the sample through a 40x/1.3NA oil immersion objective (Zeiss). The META module of the microscope was configured as a 350-450nm bandpass filter to detect backwards scattering SHG signal from collagen (173). Vessels were imaged under physiological loading conditions of λ_z=1.54 and *P*=110mmHg as well as three distinct geometries for affine motion analysis. Physiological loading conditions were determined through biaxial tests and from previously published data (164). The three loading configurations for affine motion calculations include higher axial stretch, λ_z =1.55, with reduced pressure, *P*=40 mmHg, reduced axial stretch, λ_z =1.25, with higher physiological pressure, *P*=110mmHg, and an intermediate condition with moderate axial stretch, λ_z=1.45, and moderate pressure, *P*=80mmHg (Figure 6.1). These configurations produce geometries of high axial stretch with low circumferential stretch, high circumferential stretch with low axial stretch and a nearly equi-biaxial stretch. The

configurations represent the limits of axial and circumferential deformations for the vessel as well as limits of deformation and rotation of engaged collagen fibers experienced during a typical biaxial mechanical test. Zeiss LSM Image Browser (Zeiss) was used to export image stacks to .tiff files for analysis.

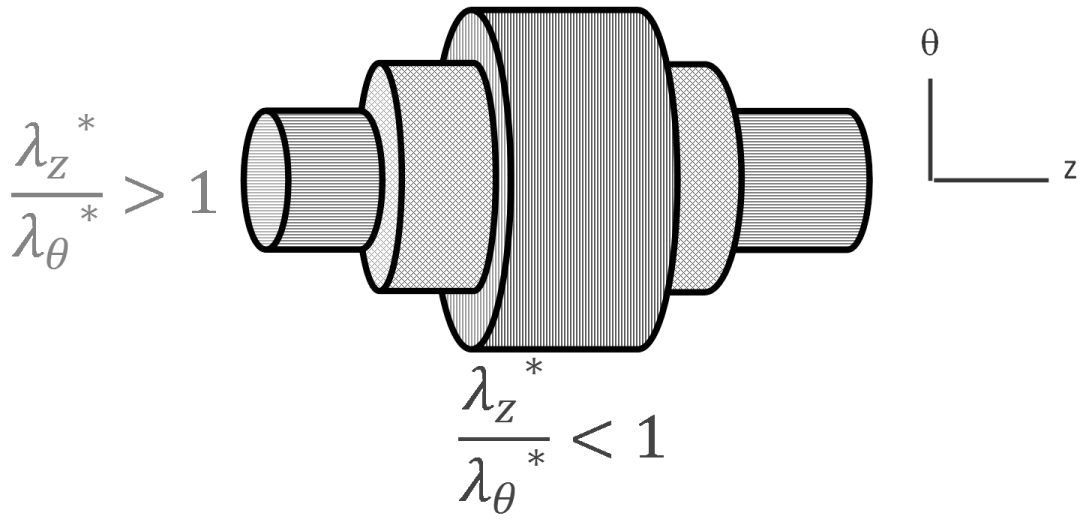

Figure 6.1: In addition to physiological loading conditions, arteries were also imaged under three distinct geometric configurations. These configurations represent states of increased axial stretch and decreased pressure (horizontally stripped), reduced axial stretch and increased pressure (vertically stripped), and an intermediate configuration (crosshatched). The indicated axial (λ_z^*) and circumferential (λ_θ^*) stretch ratios are relative to the intermediate loading configuration.

Estimation of collagen fiber angle distribution

The angular distribution of collagen fibers for each optical slice in a z-stack was estimated using MATLAB code that was modified from a fast Fourier series algorithm reported previously (107). The inner and outer bounds of the collagen fiber layer within the image stack were determined by examining the orthogonal views of the reconstructed vessel. Each optical slice was low passed filtered, converted to a binary image using Otsu's method to threshold, and windowed with a 2D Tukey window; a fast Fourier

transform was performed, and a power spectrum was generated. This power spectrum was filtered and used to generate a histogram of frequency intensities between -90 and 90 degrees in 4 degree increments (Figure 6.2). The fiber angle distribution at each wall location was averaged across the entire image stack to obtain a mean fiber distribution for each vessel. For each loading configuration, fiber angle distributions at corresponding normalized wall locations were averaged across all samples to obtain a representative surface of fiber distributions as a function of wall location.

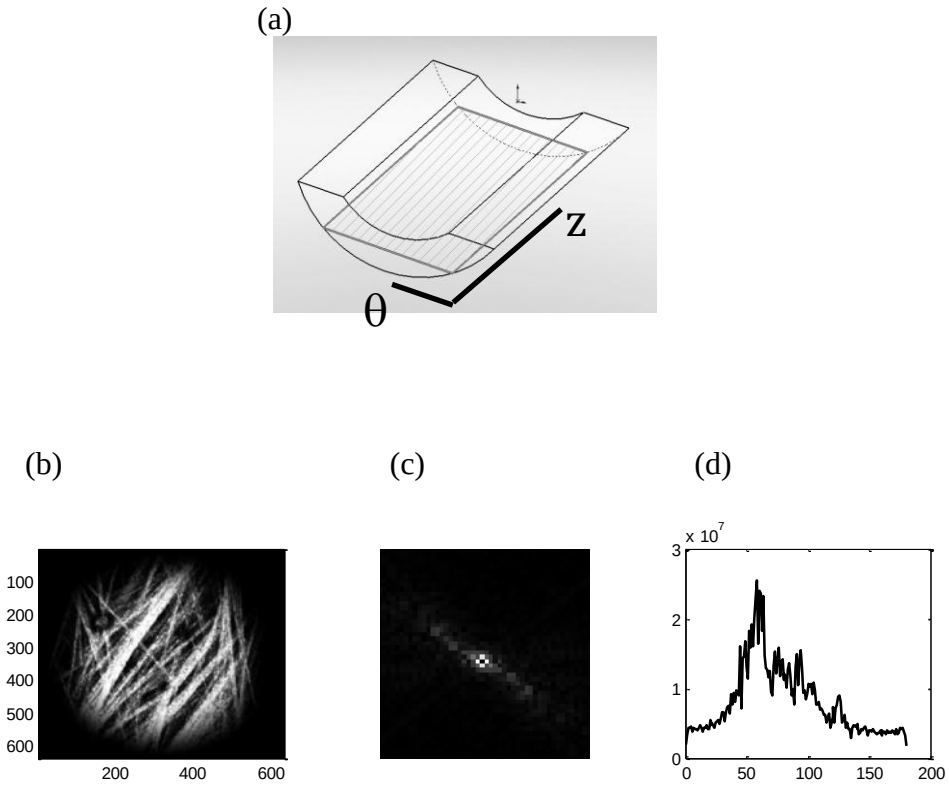

Figure 6.2: Image slices were taken at 0.5μm intervals across the entire thickness of the adventitial layer. Each image slice (a) is then divided into square segments, windowed (b) and a fast Fourier transform algorithm (c) was used to determine the distribution of fiber angles (d). Fiber distributions at normalized wall locations were averaged to determine a mean distribution for each experimental group.

Prediction of fiber angles at different loading conditions

Fiber angles measured at physiological loading conditions were transformed to angles in the stress-free state according to the relation

$$\alpha_R = \tan^{-1}\left(\frac{\lambda_z^h}{\lambda_\theta^h}\tan\alpha_{phys}\right) \tag{6.1}$$

where α_R is the predominant fiber angle at the stress-free state, and are in vivo axial and circumferential stretch ratios, and α_{phys} is the predominant fiber angle measured under physiological loading conditions. This relation was also used to transform fiber distributions between different states of axial and circumferential stretch.

Parameter estimation

Parameter estimation was performed according to previous studies (56); however, this study used experimentally measured opening angles to calculate circumferential stretches. A four-fiber constitutive model was used to estimate material and structural parameters (4). A constrained mixture model used in previous studies (56, 153), incorporating material and structural parameters as well as distributed fiber angles, was also used. In the previous version of the constrained mixture model, the fiber distribution was defined using a normal distribution; however, this study used a distribution defined by either a sum of three Gaussian terms or a single Gaussian term, equation (6.2).

$$f(\omega) = \sum_n a_n \exp\left(-\frac{(\omega - b_n)^2}{2{c_n}^2}\right) \tag{6.2}$$

Here, n=3 or 1, ω is the loaded fiber angle and a_n, b_n and c_n are parameters determined by fitting the mean fiber distribution determined from multiphoton images to a three or one term Gaussian distribution. Parameter estimation was first performed while allowing structural parameters to be determined through non-linear regression, and

performed a second time using fiber angles and fiber distributions measured from multiphoton images. Constants for equation (6.2) were determined using the MATLAB curve fitting toolbox. Fitting errors were calculated by minimizing the error function,

$$error = \sum_{i=1}^{n} \left(\frac{P_{meas}(i) - P_{model}(i)}{P_{mean}} \right)^2 + \sum_{i=1}^{n} \left(\frac{f_{meas}(i) - f_{model}(i)}{f_{mean}} \right)^2 \qquad (6.3)$$

where $P_{meas}(i)$ is the measured pressure for data point i, $P_{model}(i)$ is the pressure predicted by the model at data point i, P_{mean} is the mean of all measured pressures, $f_{meas}(i)$ is the measured axial force for data point i, $f_{model}(i)$ is the axial force predicted by the model at data point i, and f_{mean} is the mean of all axial force measurements (56).

Predictive power of models using measured microstructural data

Mean best fit parameters for each model were used to predict the mechanical response of arteries used in biaxial tests. The error between predicted and experimentally measured mechanical response was calculated using the error function minimized in parameter estimation, equation 6.3.

Statistical analysis

Mean values were compared using unpaired, two-tailed t-tests, with significance taken at $p<0.05$. For comparisons of more than two means, a one-way ANOVA was used with a Tukey's post hoc test. Bartlett's test was used determine differences in variances with significance taken at $p<0.05$.

Results

Biomechanical testing.

The results of biaxial tests, Figure 6.3, indicate mechanical behavior similar to that of previous studies of mouse blood vessels (29, 45, 154). During fixed length inflation, the pressure-force response taken at higher axial stretches, the axial force increased with increases in pressure while tests performed at lower axial stretches the axial force decreased with increases in pressure.

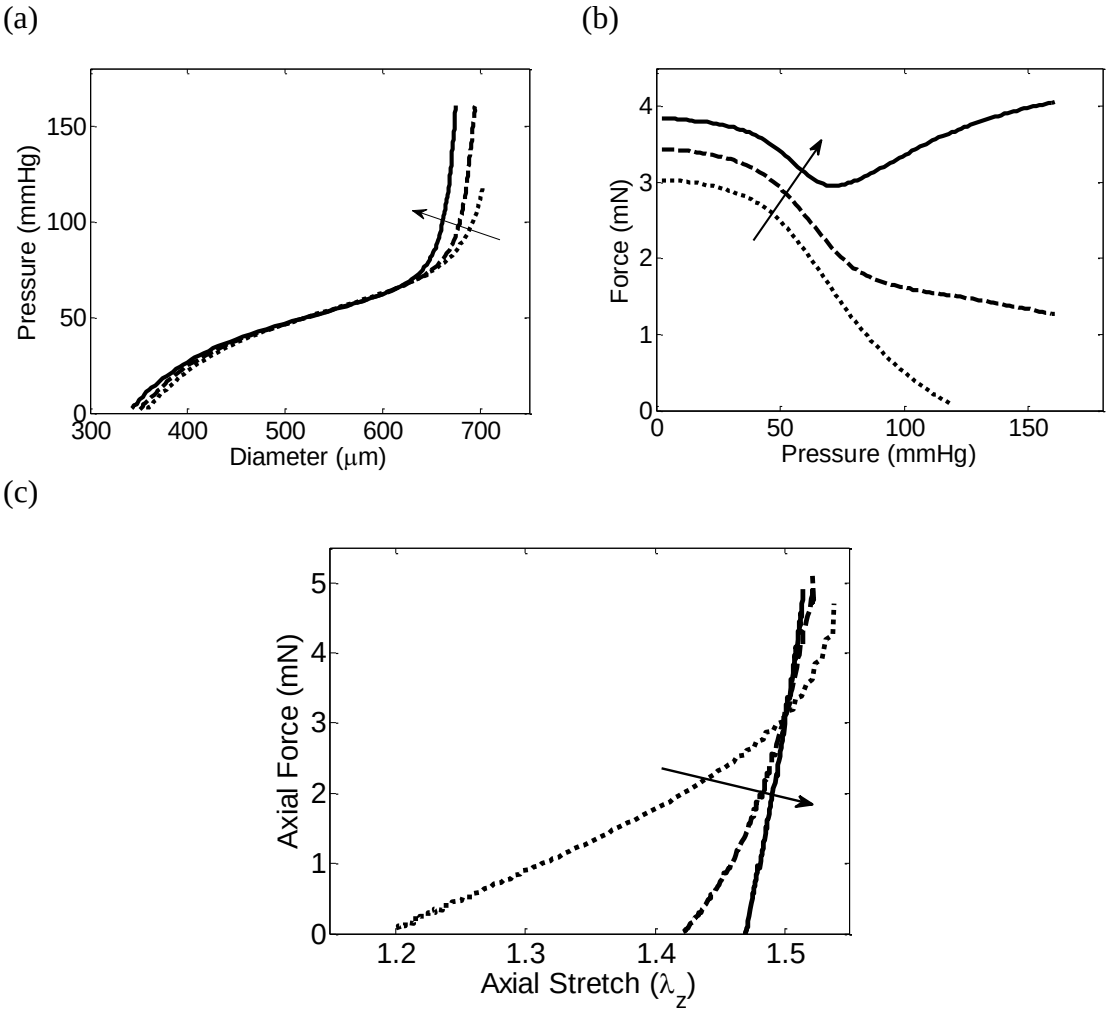

Figure 6.3: Representative results from biaxial testing reveal mechanical behavior similar to previous tests of mouse carotid arteries (53, 154). Arrows in panel a and panel b indicate increasing axial stretch ratio, and the arrow in panel c indicates increasing pressure.

During force-length tests, vessels exhibit stiffer mechanical behavior for tests performed at higher pressures. The curves for force-length tests performed at different pressures intersect at a point known as the *in vivo* axial stretch ratio (24, 147).

Multiphoton microscopy

Optical image slices can be reconstructed to reveal the structure of collagen fibers within the blood vessel wall, Figure 6.4, Collagen fibers exist at a variety of orientations that can be quantified and can be imaged through the entire thickness of the wall, up to 100μm).

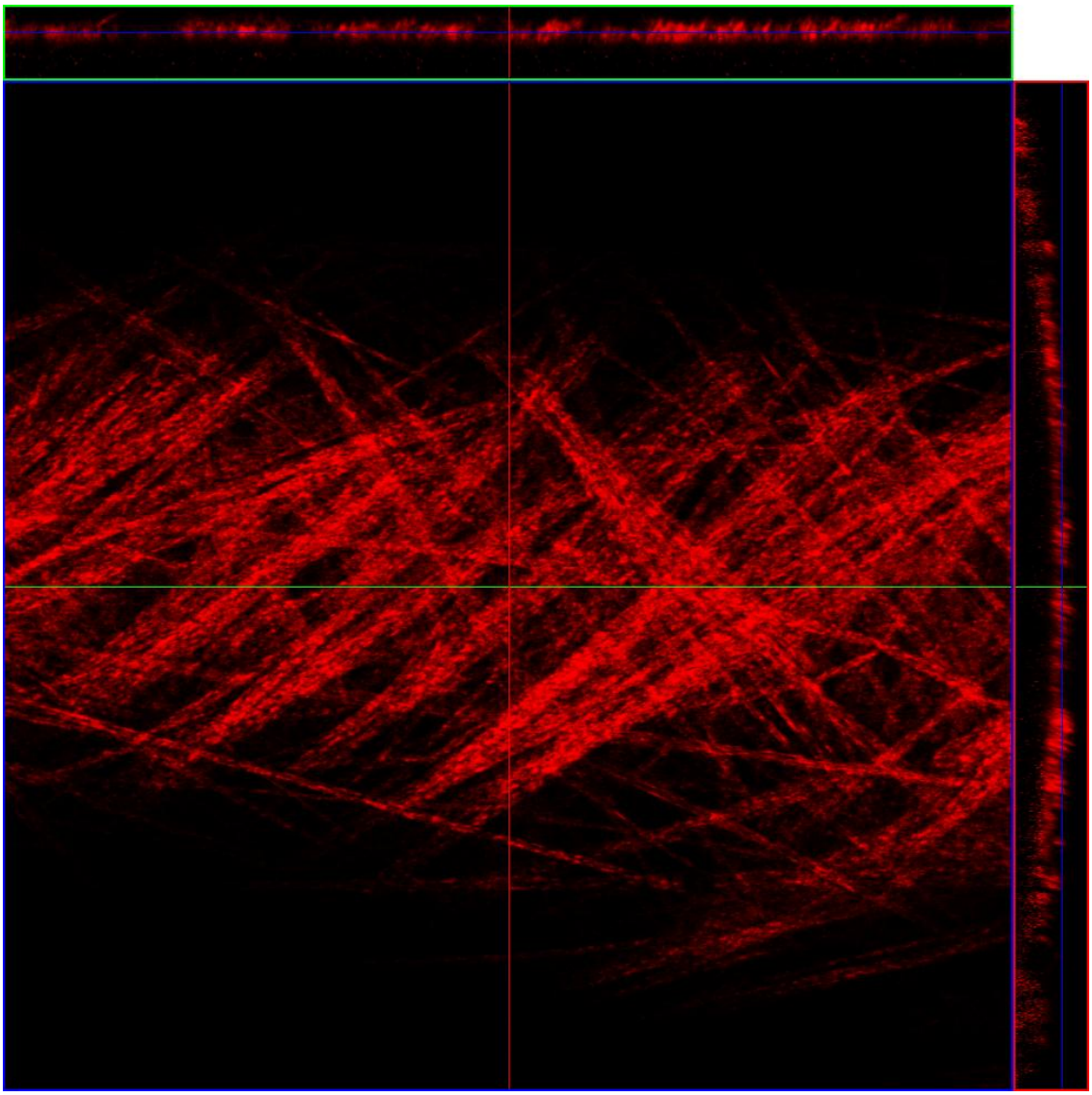

Figure 6.4: Reconstruction of optical slices reveal longitudinal and cross section views of arteries. Scale bar represents 50μm

Image processing

Fiber angle distributions measured at physiological pressures and axial stretches reveal variations in fiber angle distribution shape at locations throughout the vessel wall, Figure 6.5a The mean fiber angle distribution surface suggests that fibers are predominately distributed in a diagonal direction towards the lumen of the vessel

(normalized wall location of 0) while fibers at the outermost surface (normalized wall location of 1) of the adventitia have a preference for axial alignment. When averaging across the entire thickness of the adventitia, the resulting physiological fiber distribution suggests a mean bimodal distribution with a peak in the axial direction at 0° and a second peak at -32°, Figure 6.5b. The mean histogram of all vessels was fitted to Gaussian distributions for use in parameter estimation studies, Figure 6.5c and Table 6.1.

Table 6.1: The mean *in vivo* fiber angle distribution was fitted to Gaussian distributions described using one and three terms as defined by equation 6.2. These constants produce the curves depicted in Figure 6.5c. The constants b1, b2, and b3 represent the mean fiber angle, in radians, of separate fiber families.

Three-term Gaussian		One-term Gaussian	
a1 =	0.00331	a1 =	0.008391
b1 =	0.02141	b1 =	-0.1675
c1 =	0.2554	c1 =	1.273
a2 =	0.003526		
b2 =	-0.5742		
c2 =	0.2637		
a3 =	0.005881		
b3 =	-0.0868		
c3 =	1.697		

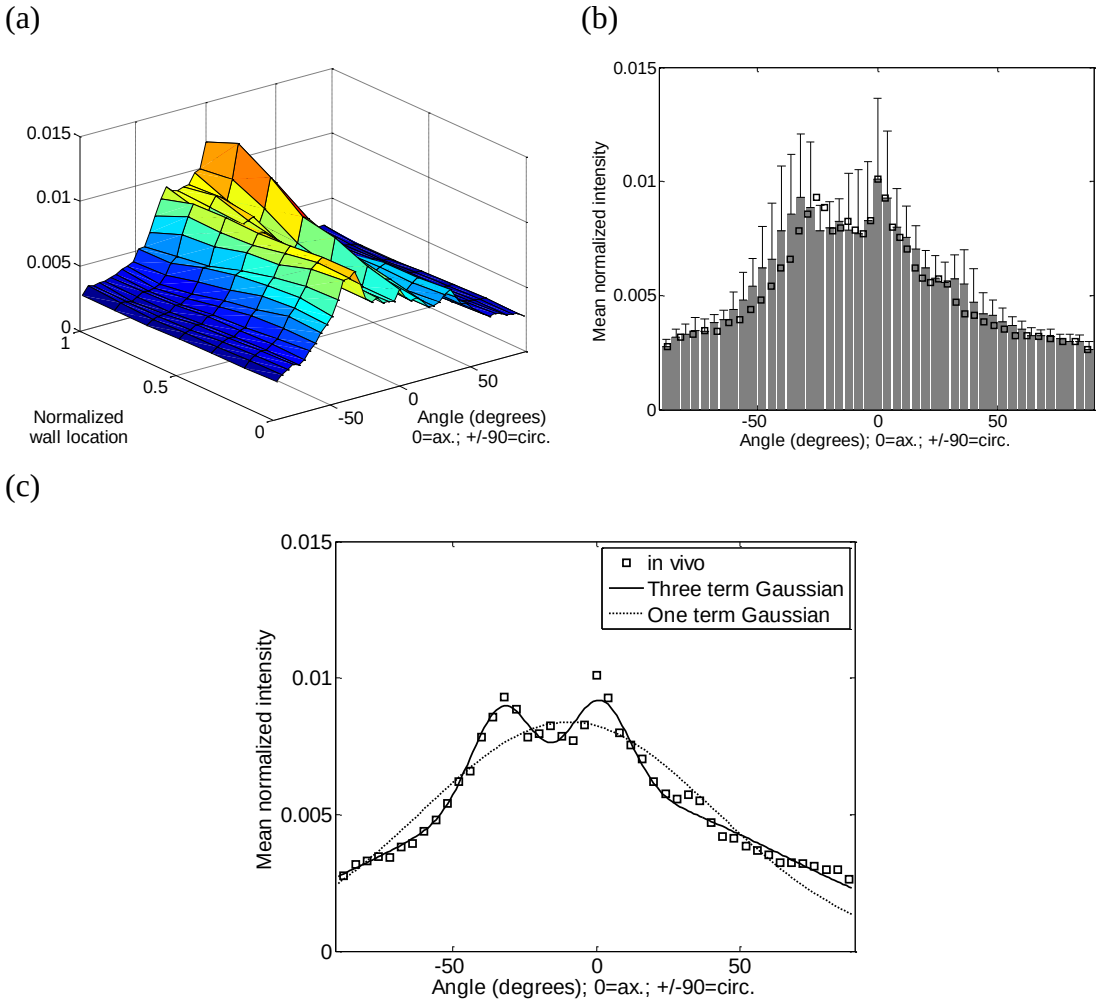

Figure 6.5: The distribution of fiber alignment varies through the depth of the vessel wall. Fiber distributions for samples imaged at physiological loading were averaged across normalized wall locations to obtain a mean local fiber distributions (a). The fiber distribution through the wall was also averaged to generate a mean distribution (b) which was transformed into a stress-free configuration (square markers). The stress-free configuration was fitted to three and one term Gaussian curves which were then used for parameter estimation.

Affine deformation assumption

Fiber angle distributions were measured for arteries imaged under three geometric configurations – high axial with low circumferential stretch, low axial with high

circumferential stretch and an intermediate configuration (Figure 6.6). In the configuration with high axial and low circumferential stretch (Figure 6.6a, b), fibers were highly aligned in the axial direction. As pressure is increased and axial stretch is reduced, fibers rotated in the circumferential direction and become less aligned axially (Figure 6.6c, d, e, f). Mean fiber distributions were also predicted (square markers on Figure 6.6b, f) using equation 6.1 and using the fiber distribution of the intermediate configuration as the reference configuration for deformation. While the overall shape of the distributions suggest that fibers rotate in directions consistent with stretching in the axial and circumferential directions, correlation coefficients, R^2, between predicted and measured fiber distributions vary with the type of deformation (Figure 6.6b, f).

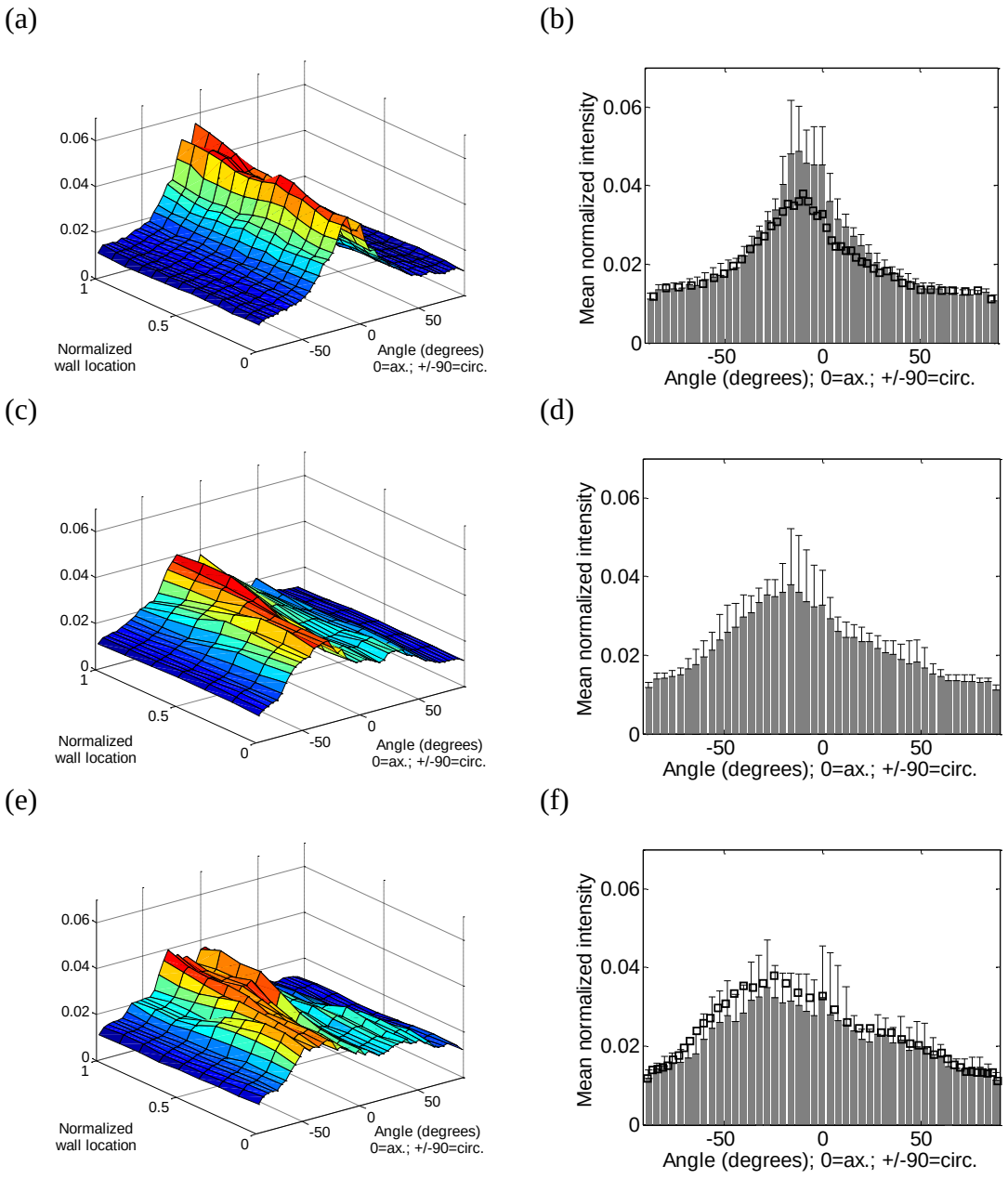

Figure 6.6: Fibers through the depth of the vessel wall become more aligned axially when the vessel is stretched axially (a-d). The rotations of fibers agree with affine motion assumptions with an R-squared value of 0.76 or greater. Local fiber distributions were averaged at normalized wall locations to generate a fiber distribution surface (a, c, e), and fiber distributions surfaces were averaged through the depth of the wall to obtain mean fiber distributions. The inset figures correspond to loading conditions in Figure 6.1, and open squares indicate the predicted distribution based on the fiber distribution measured in the intermediate state and assuming affine deformations. R^2 values represent correlation coefficients between measured and predicted fiber orientations

Parameter estimation

Material and structural parameters were estimated using a four-fiber model (4) and a fiber distribution model (56). When estimating all material and structural parameters (Table 6.2a, Table 6.3a), the mean fitting errors were not statistically different between four-fiber and fiber distribution models (Figure 6.7).

Table 6.2: When using a fixed fiber angle, many estimated material parameters, especially those associated with diagonal and axial fibers, are significantly different (b). The isotropic parameter and parameters associated with circumferential fibers were not statistically different. *p* indicates differences in means between corresponding parameters of the upper and lower tables.

(a)

Variable α	b_0 (Pa)	$b_{1,1}$ (Pa)	$b_{1,2}$	$b_{2,1}$ (Pa)	$b_{2,2}$	$b_{3,1}$ (Pa)	$b_{3,2}$	α	Error
#1	20735	173.41	0.3311	7332.8	0.1211	57.346	.4912	36.86	0.035
#2	15562	277.91	0.1572	8314.5	0.0044	65.227	1.2365	30.98	0.020
#3	16377	66.368	0.3627	4451.8	0.0830	2.6547	2.0908	33.03	0.022
#4	14500	1078.3	0.1112	7769.9	0.0001	33.591	1.1152	34.19	0.028
#5	13854	78.371	0.1858	4335.3	0.2609	69.533	1.5906	27.55	0.032
#6	16285	284.61	0.1957	6963.1	0.0851	27.996	1.6447	30.28	0.023
Mean	16219	326	0.2239	6527.9	0.0924	42.725	1.5282	32.15	0.027
SD	2425	380	0.1001	1714.0	0.0955	25.864	0.3438	3.26	0.006

(b)

Fixed α	b_0 (Pa)	$b_{1,1}$ (Pa)	$b_{1,2}$	$b_{2,1}$ (Pa)	$b_{2,2}$	$b_{3,1}$ (Pa)	$b_{3,2}$	α	Error
#1	16537	2160.7	0.1324	664.65	0.0001	4497.6	0.4887	-25.47	0.051
#2	15333	768.35	0.1066	5272.2	0.0001	741.3	0.8199	-25.47	0.035
#3	162	159.02	0.2980	0.0001	0.0001	1173.5	0.6685	-25.47	0.053
#4	12152	2149.5	0.0767	0.0001	0.0001	4236.6	0.2534	-25.47	0.046
#5	13769	225.91	0.1431	5664.4	0.0001	125.07	1.5670	-25.47	0.036
#6	16935	587.27	0.1529	6228.9	0.0001	177.93	1.3474	-25.47	0.033
Mean	15381	1008	0.1516	2971.7	0.0001	1825.3	0.8575		0.042
SD	2075	916	0.0768	3037.7	0.0000	2008.0	0.5063		0.009
p<0.05	0.53	0.12	0.19	0.032	0.039	0.055	0.023		

Table 6.3: Estimating all material and structural parameters yielded the smallest fitting error. Lower case letters in the row $p<0.05$ indicate significant differences in parameters, and NS indicates $p>0.05$.

(a) Symmetric	b^e (Pa)	b^m (Pa)	b^m_1 (Pa)	b^m_2	b^{cz}_1 (Pa)	b^{cz}_2	b^{ca}_1 (Pa)	b^{ca}_2	λ_f^h	Error
#1	170170	113450	2516	0.3068	230730	0.1557	6170.3	2.39	1.50	0.043
#2	142300	76616	3340	0.1522	277660	0.0173	3337.4	2.42	1.53	0.022
#3	136910	91134	603	0.3759	148110	0.0732	85.2	3.61	1.56	0.023
#4	119980	80951	11592	0.1133	262910	0.0001	957.0	1.96	1.62	0.030
#5	127910	67866	972	0.1808	146460	0.2779	3267.4	3.21	1.47	0.034
#6	142650	86529	3072	0.1962	231140	0.0955	630.2	3.21	1.53	0.023
Mean	139987	86091	3683	0.2209	216168	0.1033	2407.9	2.80	1.54	0.029
SD	17199	15636	4031	0.0999	56380	0.1022	2298.6	0.63	0.05	0.008
p<0.05	a	NS	NS	NS						

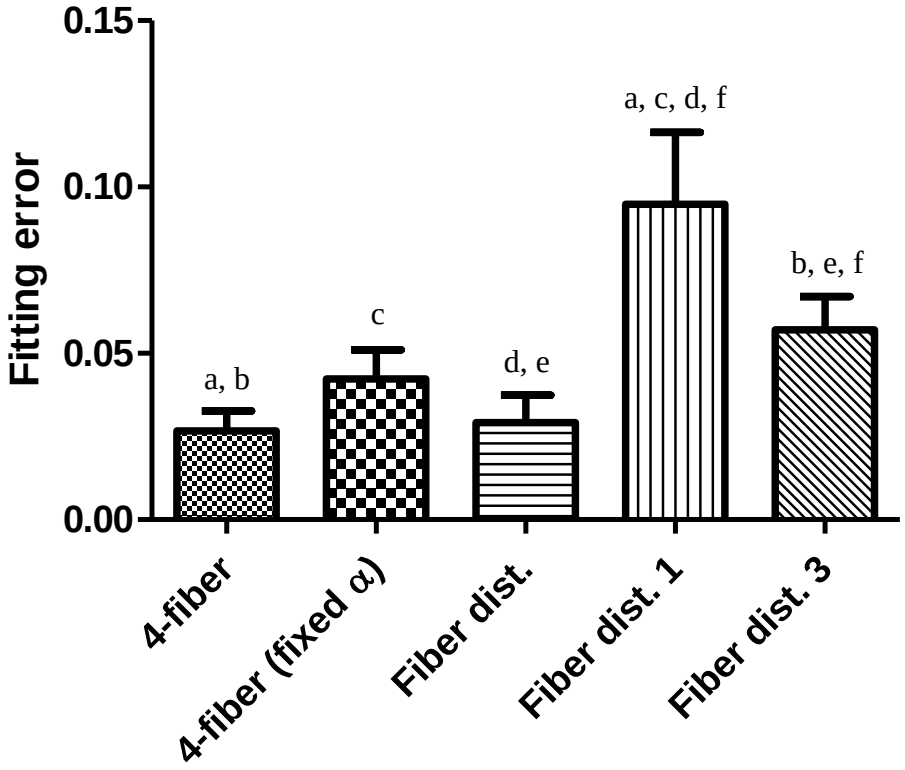

Figure 6.7: Mean fitting errors increased when using experimentally measured fiber distributions (columns 4 and 5); however, using a measured fiber angle did not increase the fitting error of the four-fiber model. The third column indicates error when estimating all material and structural parameters, and the fourth and fifth columns indicate errors for one and three term Gaussian distributions, respectively. (Symbols a-f indicate $p<0.05$, all other pair-wise comparisons are $p>0.05$)

Using microstructure information in parameter estimation

Parameter estimation was also performed using structural parameters determined from multiphoton images. For the four-fiber model, the *in vivo* distribution was transformed to the stress-free state and the non-axially aligned peak, -25.47°, was used as the diagonal fiber angle, Figure 6.5b. The mean fiber distribution of the vessels imaged under physiological conditions was curve fitted to one and three term Gaussian distributions (Figure 6.5c). A one term Gaussian distribution was used because it requires

a similar number of parameters as the four-fiber model, and a three term Gaussian distribution was used because it accurately captures the shape of the measured in vivo fiber distribution, Figure 6.5c.

Using a predefined diagonal fiber angle significantly increased the fitting errors, Figure 6.7, and resulted in significant changes to a number of material parameters (Table 6.2, Table 6.3). Parameters from the same model were compared while fitting errors were compared across all forms of models. In the four-fiber model, no significant changes were seen in the isotropic, b_o, and circumferential parameters, $b_{1,1}$ and $b_{1,2}$; however, significant changes were seen for parameters associated with axial, $b_{2,1}$ and $b_{2,2}$, and diagonal fibers, $b_{3,1}$ and $b_{3,2}$. Incorporating the fiber angle distribution measured in Figure 6.6.d into a more advanced constrained mixture model (56) resulted in increases to fitting error as well as changes in the b^e parameter, Table 6.4.

Table 6.4: Defining measured fiber distributions using one or a sum of three Gaussian terms increased fitting errors (a, b). Lower case letters in the row $p<0.05$ indicate significant differences in parameters, and NS indicates $p>0.05$.

(a)

Three-term Gaussian	b^e (Pa)	b^m (Pa)	b^{m_1} (Pa)	b^{m_2}	b^{ca_1} (Pa)	b^{ca_2}	b^{cb_1} (Pa)	b^{cb_2}	b^{cc_1} (Pa)	b^{cc_2}	λ^{f_h}	Error
#1	111980	104270	24622	0.1216	0.0001	0.3744	303900	0.6387	373.9	0.0001	1.5	0.057
#2	97174	81440	13259	0.0770	0.0001	0.1446	239200	0.6260	371.8	0.0001	1.53	0.054
#3	113220	100080	2256	0.2771	0.0001	0.3241	122430	0.6158	0.1631	0.0001	1.56	0.065
#4	85020	74577	20578	0.0806	0.0001	0.3470	254740	0.3026	0.0712	0.0001	1.62	0.049
#5	82272	61173	15828	0.0517	0.0001	0.1540	210010	0.9026	0.0378	0.0001	1.47	0.072
#6	109090	95810	6305	0.1487	0.0001	0.0741	174740	0.7299	4245	0.0001	1.53	0.045
Mean	99793	86225	13808	0.1261	0.0001	0.2363	217503	0.6359	831.8	0.0001	1.54	0.057
SD	13765	16707	8449	0.0817	0.0000	0.1269	63633	0.1957	1682.0	0.0000	0.05	0.010
p<0.05	a	NS	NS	NS								

(b)

One-term Gaussian	b^e (Pa)	b^m (Pa)	b^{m_1} (Pa)	b^{m_2}	b^{ca_1} (Pa)	b^{ca_2}	λ^{f_h}	Error
#1	132390	116010	18629	0.1042	97590	0.5841	1.5	0.084
#2	112100	83340	10958	0.0578	99721	0.4331	1.53	0.099
#3	122740	106550	102.58	0.4714	63934	0.3424	1.56	0.098
#4	108490	79190	11233	0.0936	100030	0.2079	1.62	0.073
#5	115830	93466	2.0414	0.3805	69210	0.6488	1.47	0.134
#6	127080	110900	99.22	0.3539	74669	0.4813	1.53	0.081
Mean	119772	98243	6837	0.2436	84192	0.4496	1.54	0.095
SD	9199	15184	7910	0.1785	16715	0.1606	0.05	0.022
p<0.05	NS	NS	NS	NS				

As expected, larger increases in fitting error were associated with a decreasing number of parameters used to describe the fiber distribution. This model was similar to the fiber distribution model used in ref. (56); however, this study assumed that constituent reference lengths were equal to the reference lengths of the mixture. In addition, parameter tables show a mean *in vivo* fiber stretch ratio, λ_f^h, rather than the previously used ω^h. Because λ_f^h is directly calculated from ω^h and vessel geometry, and ω^h is not used to define the measured distributions, rather this study uses λ_f^h. When comparing fitting errors across both the four-fiber and the fiber distribution models, the fitting errors were not significantly different between the four-fiber models and the fiber-distribution model that estimated the fiber distribution, Figure 6.7.

Prediction of mechanical response using mean parameters

Confidence intervals for all models overlap; however, the model using fiber distributions approximated using three Gaussian had a smaller 95% confidence interval range, Figure 6.8a.

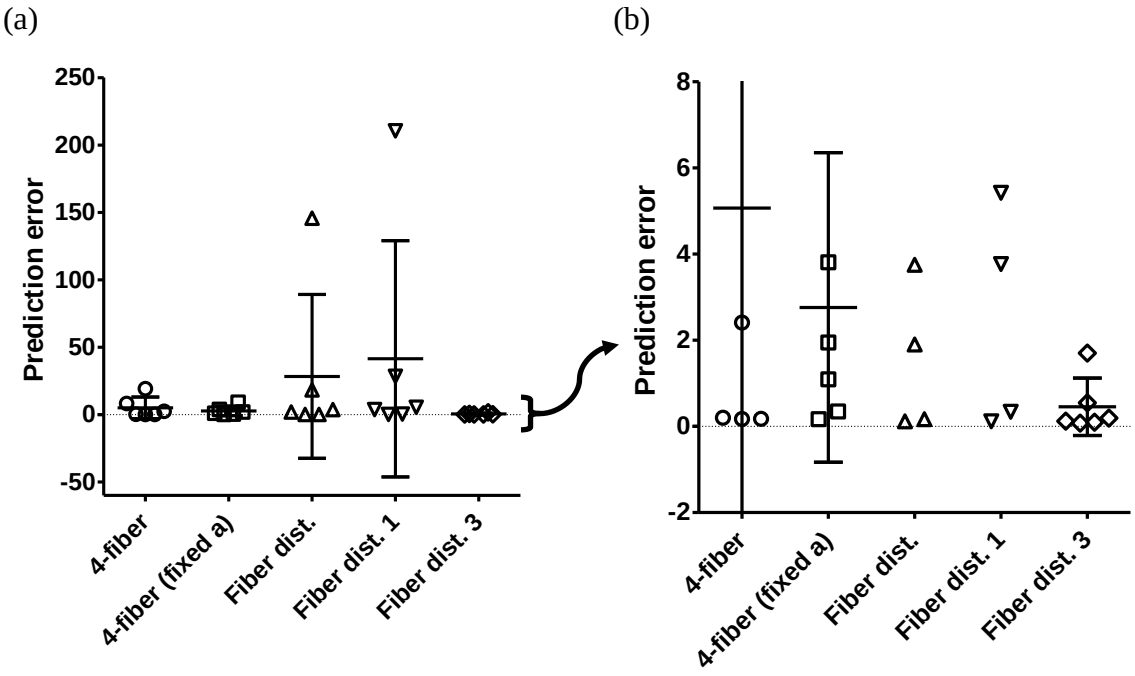

Figure 6.8: The fiber distribution model using three Gaussian terms is able to approximate previously measured mechanical response data with the smallest 95% confidence interval (a). Examining the data over a smaller range reveals that errors for the fiber distribution model using three Gaussian terms are clustered near 1 while errors for all other models are distributed over a wider range of errors; this suggests that closely matching the *in vivo* fiber distribution in a constitutive model predicts the mechanical response more consistently and with smaller errors (b). Horizontal bars indicate means and symbols designate errors of individual samples. The means were not statistically different, $p>0.05$, however variances differed significantly, $p<0.0001$.

The large variations in errors of many models resulted in statistically insignificant differences in mean errors; however, the relatively close clustering of data points near the mean suggests a trend in which using three Gaussian distributions to describe fiber angle distributions results in more accurate and more consistent model predictions, Figure 6.8b.

Discussion

Constitutive relations have the power to both predict the mechanical response of tissues under load as well as to aid in understanding the interactions between various constituents of biological tissues. Recent formulations of constitutive relations have incorporated the physical structure of arteries in predicting their mechanical response (56, 63, 175). Though structurally motivated constitutive relations provide a more physically meaningful description of arteries, they often increase the number of parameters that must be estimated, thus increasing the possibility of non-unique solutions. Advances in experimental techniques can aid in quantifying many parameters that previously must be estimated and reduce the number of free parameters to those that are truly experimentally intractable.

In this study, we used multiphoton imaging to measure collagen fiber angle distributions of intact, pressurized and stretched adult mouse carotid arteries. This technique permits the imaging of the entire wall thickness of a single artery under various loading conditions. When experimentally measured structural information is used in parameter estimation, a fiber distribution model using three Gaussian terms yielded similar fitting errors as a four-fiber model using a single mean fiber angle, Figure 6.7. However, when predicting the mechanical response of arteries using mean material parameters, modeling the entire distribution of fiber angles produced lower mean errors ($p>0.05$) with lower variances ($p<0.0001$), Figure 6.8b. Although the mean error for the fiber distribution model was not statistically lower, the clustering of data points near the mean suggests better predictive accuracy. When comparing material parameters, axial ($b_{2,1}$ and $b_{2,2}$) and diagonal ($b_{3,2}$) fiber parameters were significantly different when using a fixed diagonal fiber angle while the isotropic (b_o) and the circumferential ($b_{1,1}$ and $b1_{,2}$)

fiber parameters did not significantly change, Table 6.2b. This result is expected because b_o represents the non-fibrous isotropic matrix of the vessel and should be less sensitive to changes in the structure of the fibrous components of the vessel. Further interpretation of these results, however, is made difficult by the large standard deviations in many of the material parameters. In a previous study, Wicker et al. also showed that using a fixed fiber angle in the four-fiber model altered the fitting error, but the study did not report the level of statistical significance. In the context of structurally motivated constitutive relations, the four-fiber model assumes that the artery consists of circumferential, axial and two families of symmetric diagonal fibers whereas images collected in this study reveal axial fibers and only one family of diagonal fibers, Figure 6.5b. This study also shows that fiber angle distributions vary through the wall of the artery, Figure 6.5a, and this is consistent with previous studies showing variations in fiber angle distributions throughout the wall of arteries from other species (145, 158). Variations in fiber angles may be reconciled through averaging, as in this study, or through weighted averaging as performed in previous studies (158). Employing a multilayered model may also improve the accuracy of model predictions (63).

Parameter estimation was also performed by modifying a previously described distributed fiber model (56) to use Gaussian distributions of fiber angles measured from multiphoton images, Figure 6.5c. When estimating all material and structural parameters, the fitting errors for the fiber distribution model were not significantly different from the four-fiber models; however, fitting errors increased when measured fiber distributions were used, Table 6.3 and Figure 6.7. The largest increase in error was associated with the use of only one Gaussian distribution term, which describes only one fiber family, while

using the three terms in the Gaussian distribution produced a fitting error that was not significantly different than the error obtained when using a fixed fiber angle in the four fiber model, Figure 6.7. Using measured fiber distributions also produced changes in the isotropic parameter associated with elastin, b^e; however, there were no statistical differences in the parameters associated with SMC, b^m, b^m_1, and b^m_2. Results from the three-term Gaussian distribution included a modulus-like parameter, b^{ca}_1, which reached the lower limits (0.0001) for the range of possible parameters, Table 6.3b. The parameters b^{ca}_1 and b^{ca}_2 correspond to a family of collagen fibers with a mean angle of -1.22°, thus the mechanical response may partially overlap that of parameters b^{cc}_1 and b^{cc}_2. This suggests that using three terms to describe the fiber distribution may not be necessary to capture the salient features of the mechanical response of the artery; however, three Gaussian terms were necessary to adequately capture the shape of the fiber angle distribution, especially the non-zero values at ±90°. The lack of differences in fitting errors when using a more complex but more physically descriptive model suggests that the four fiber model may be sufficient for accurately modeling experimental results; however, parameter estimation using a model that incorporates multiple distributed fiber families may provide insight into material properties that are experimentally intractable.

Constitutive relations also have the ability to predict the mechanical response of arteries when material and structural parameters are known. Prediction of mechanical behavior is desired when excising, removing and testing an artery is not feasible, such as in a live animal or patient. When structural information can be directly measured, we show that using the entire distribution of fiber angles, rather than a single mean angle, can offer lower prediction errors and errors with less variance across different samples,

Figure 6.8b. Though mean prediction errors are not statistically different, the magnitudes of the means as well as the relative sizes of confidence intervals suggest a trend that using three Gaussian terms to represent the fiber angle distribution in a constitutive relation offers better predictive accuracy over other forms of constitutive models examined in this study. Even when using a measured fiber angle in the four-fiber model, the resulting errors have a lower variance than when fiber angles are estimated, Figure 6.8b. These results suggest that using measured structural parameters rather than estimated structural parameters produces lower prediction errors; thus, it may be possible to accurately predict mechanical response of an artery by measuring its structural parameters and using previously determined material parameters.

Constitutive relations often assume that the tissue is undergoing affine deformations at all stretches; however previous studies suggest that not all biological tissues may undergo affine deformations (6). This study examined the deformation of fibers while the vessel is pressurized and stretched to three different aspect ratios, and the results suggest that, qualitatively, fibers undergo expected rotations with measured fiber orientations matching predicted orientations to varying extents throughout the range of fiber angles. Our results suggest that agreement between measure and predicted fiber distributions may vary according to the type of deformation, Figure 6.6b, f. With R^2 values of 0.76 and 0.80, the results suggest a reasonable agreement between measure and predicted fiber distributions. In contrast to the physiological fiber distribution, Figure 6.5a, the geometries examined for affine motion analysis yielded fiber distributions that were predominantly non-bimodal. This may result from differences in fiber distribution

through the wall of the vessel and from the combination of axial stretches and pressures used to create the three distinct geometries.

This study only examined a small range of deformations because the Fourier transform analysis used to measure fiber angles provides the best resolution when fibers are straightened and not undulated. This limited the study to a narrower range of stretch ratios; thus, inferences cannot be made whether deformations while fibers are undulated are affine or non-affine. The possibility of non-affine motions at lower stretches may explain larger fitting errors that sometimes occur at lower stretch ratios. It should also be noted that the resulting fiber angle distribution measured from Fourier analysis may include information about fiber stretch as well as fiber orientation. For example, fibers aligned perfectly at zero or 90 degrees will remain aligned at zero or 90 degrees as long as the deformations do not have shear; however, their lengths may change and this length change may be incorporated in the orientation analysis. Ultimately, future studies should image and quantify arteries under loading conditions experienced throughout biaxial tests; this will help test some of the fundamental assumptions underlying constitutive relations. Imaging multiple segments of the artery may also provide a more representative mean distribution. Indeed, it is possible that non-affine motions may minimally affect the overall mechanical behavior of the tissue when examined on the tissue level (59).

In the current study, we have incorporated microstructural information, collagen fiber angle distributions, into structurally based constitutive relations and have shown that the addition of experimentally measured structural parameters does not increase fitting errors for structurally descriptive constitutive relations. When evaluating the predictive capabilities of structurally motivated constitutive relations, using a measured fiber angle

distribution yields lower and more consistent prediction errors. This finding suggests that when material parameters are known, the measurement of the *in vivo* fiber angle distribution may be sufficient to predict the mechanical response of an artery. We also show that the deformation of collagen fibers can be qualitatively predicted using affine motion assumptions. Absent of detailed fiber distribution information, the four-fiber model remains useful in capturing the mechanical response of arteries. When combined, the techniques used in this study for measuring fiber distributions under different loading conditions and for incorporating measured fiber distributions in constitutive models offers a novel approach for reducing the number of parameters to be estimated and for using measureable structural parameters to predict the mechanical behavior of arteries.

Chapter 7

CLOSURE, LIMITATIONS AND FUTURE CONSIDERATIONS

Closure

A central theme of this dissertation was the development of a multi-scale theoretical-experimental framework for quantifying the evolution of the biomechanical behavior and microstructural content and organization of arteries. The experiments were undertaken with the context of cardiovascular disease in mind and with the goal of further understanding the complex interactions between observations of cell-mediate processes made at the microstructural level with the tissue level mechanical response. A fibulin-5 knockout mouse model was used to quantify the biomechanical and microstructural properties carotid arteries throughout maturation. Carotid arteries from KO mice are tortuous and have fragmented elastic fibers. We developed microscopy and image analysis techniques for quantifying the microstructure of mouse carotid arteries, and we described the correlation between microstructure of these arteries and their mechanical response as well as the evolution of material parameters during maturation. Finally, we developed a microstructurally-motivated mathematical model that describes vascular biomechanics and a three-dimensional stress-mediated model of growth and remodeling. Illustrative simulations show that stress-driven local evolution of the microstructure can capture the salient effects of mechanically mediated growth and remodeling previously shown in experiments.

The experimental aspects of this project established a framework for quantifying both the tissue level mechanical response as well as the microstructural organization of mouse carotid arteries. We used a *fbln5* knockout mouse with disrupted elastic fibers and

quantified biomechanical and microstructural differences in carotid arteries. In adult KO mice, increased axial and circumferential stiffness was observed coincident with increased opening angle and decreased *in vivo* axial stretch. Confocal microscopy revealed well defined elastic lamella in WT mice and amorphous elastin in KO mice. Two-photon microscopy showed that collagen fibers in KO mice become engaged at a lower axial stretch than in WT mice. Thus, our initial study established correlations between differences in tissue level mechanical response and microstructural organization. Motivated by distinct differences in structural and biomechanical properties, we sought to directly measure structural differences between KO and WT mice. We collected data at various time points throughout maturation because it was hypothesized that the effects of functional elastic fibers on the mechanical response of carotid arteries is age-dependent, and quantifying the temporal effects of *fbln5* would reveal insight into relationship between the evolution of microstructural and biomechanical properties. Indeed, between 3 and 13 weeks, we observed significant differences the in vivo axial stretch ratio, in vivo axial force, compliance, and opening angle of WT arteries while any changes in KO arteries were not statistically significant. The findings in KO arteries is analogous to the growth and remodeling simulation cases in which all constituents are turned over while findings from WT arteries is analogous to the case in which elastin has a much longer half-life than SMC and collagen.

This project also developed a microstructurally-motivated computational framework for vascular growth and remodeling. We developed stress-mediated evolution equations and microstructurally-motivated constitutive relations and simulated cases of altered flow and altered pressure. In growth and remodeling simulations, simulating

physiological conditions (no elastin turnover) leads to the altered wall stresses while simulating the turnover of all vascular constituents results in the maintenance of original wall stresses. We also quantified collagen fiber orientation and used this information to recapitulate the mechanical response of mouse carotid arteries. Previous studies in tissues such as heart valves and human aortas have experimentally quantified changes in collagen fiber orientations due to damage and aging; however, the approached developed here provides a three-dimensional measurement of fiber orientations though the thickness of the arterial wall and we are able to image the artery under multiple loading conditions. The growth and remodeling approach we used evolves the material properties of the artery through the deposition or constituents at their homeostatic stretch. The imaging methods developed here provide a method for experimentally validating the microstructural predictions of the model.

The results from these experimental and theoretical studies illustrate the power of a combined approach towards studying vascular growth and remodeling. We developed a constrained-mixture model for vascular growth and remodeling in which changes in mechanical response due to altered loading is predicted by evolving constituent microstructure in a stress-mediated manner. Allowing constituents to be deposited at defined homeostatic stretches provides a more physiological representation of growth and remodeling by simulating the process of a cell-mediated response to altered loading. This is in contrast to evolving the volume of constituents which simulates the consequences of growth and remodeling. The experimental and imaging techniques developed provide method for validating model simulations by directly quantifying microstructural organization and the resulting changes in mechanical response. Cardiovascular diseases

are characterized by changes in the mechanical behavior of arteries which is governed by vessel geometry as well as the organization of structural components of arteries such as collagen, elastin and SMC. The microstructure of arteries is ultimately governed by biologically-mediated processes such as cell proliferation, ECM crosslinking, and ECM degradation. Whereas previous experiments have performed isolated biomechanical tests on arteries or used destructive histological methods to characterize microstructure, the work undertaken in this dissertation provides a framework for simultaneously synthesizing experimental observations made at both the microstructure and tissue levels. Incorporating the microstructurally-motivated constitutive relation into a model for vascular growth and remodeling allows the simulation of both cell-mediated processes of evolving microstructure as well as the evolution of tissue level mechanical response. The multi-scaled nature of the models developed here combine previously isolated experimental observations into a unified system that can be used to test competing hypotheses and motivate future experiments. The ability to incorporate experimental data collected at different hierarchical scales into a single framework can also help identify the key drivers of disease progression and aid in the development of new therapeutic targets.

Limitations

This project has a number of limitations that leave room for improvements in future studies. The use of mouse models in *ex vivo* experiments brings inherent advantages in precisely controlling testing environments; however, *ex vivo* experimentation removes the tissue from its native environment and surrounding tissues may affect the *in vivo* geometry of some embedded vessels (69, 89). We estimated structural and material parameters, and we directly quantified the microstructural

organization of collagen fibers. However the high degree of variance in some material parameters makes drawing conclusions difficult.

In the fbln5 biomechanics study, we sought to identify the role of a single ECM protein, *fbln5*, on the overall biomechanical behavior of arteries; interpretation of these data are complicated by the fact that, throughout their development and maturation, mechanisms could compensate for the lack of *fbln5*. Nevertheless, given the striking differences in the mechanical and microstructural behavior of $fbln5^{-/-}$ versus $fbln5^{+/+}$, broad conclusion regarding the role of functional elastin fiber may be made. Second, we present plots of mean stress versus mid-wall strain and perform stress analyses with the assumption that the tissue is homogeneous. Clearly, however, there are significant heterogeneities, particularly between the media and adventitia, in mouse common carotid arteries. Future studies could include the incorporation of such heterogeneities, which may be based on heterogeneities in the content and organization of cells and ECM observed in our stacks of confocal microscopy images. Third, although the constitutive model employed here is microstructurally motivated, no direct correlation are made between material parameters and cell and ECM content and organization. Thus, future studies may include the use of constrained mixture models to ascribe such microstructural meaning to each parameter (56).

In studying the effects of *fbln5* on the maturation of mouse carotid arteries, we observed differences in mechanical response as well as differences in microstructural organization. These effects were observed over a period of weeks and occurred under *in vivo* conditions; thus, adaptations to the lack of *fbln5* may have also affected growth and remodeling. While physiological changes that occur during maturation can be

approximated in an organ culture experiment, it would be difficult to separate physiological change due to normal maturation from changes occurring due to dysfunctional elastin. A conditional knockout mouse model may mitigate some of these affect. We also measured collagen and elastin mass fractions, but did not measure smooth muscle cells content. Active smooth muscle cells play a role in the mechanical response of an artery, and during growth and remodeling, they undergo changes such as hypertrophy (99), proliferation (19) and migration (40, 96). Measurement of smooth muscle cell content and imaging of smooth muscle cell orientation (95) would provide additional insight into the role of fibulin-5 in the microstructural and mechanical properties of arteries. The protein content assays quantified total collagen and elastin content; however, quantification of the degree of crosslinking may provide further insight into changes in material properties of microconstituents. This study also performed multiphoton imaging and biaxial testing on separate groups of arteries. Performing both tests on a single artery would provide structural information unique to each sample for parameter estimation studies. Finally, because *fbln5* binds to other proteins such as integrins and extracellular superoxide dismutase, the effects observed in this study may not be isolated to fragmented alone (108, 133).

Growth and remodeling is a complex, hierarchical process with changes occurring at multiple length and time scales. A model that completely describes growth and remodeling should include processes ranging from gene expression to geometric changes. Our model predicts growth and remodeling using only local and mean wall stresses and does not account for biological changes such as production of signaling molecules, growth factors or changes in gene expression. While including biological changes at the

cellular and sub-cellular level would provide a higher fidelity model, doing so would require integrating a vast body of literature detailing experiments conducted under varying conditions with at varying length and time scales. Future studies will attempt to incorporate biological changes and determine the level of detail required for a satisfactory level of accuracy in prediction.

There are several limitations in the microstructure and image analysis study (152) that permit room for future improvement. Images collected in this study as well as previous studies suggest that the fiber angle distribution changes between the adventitial and luminal surfaces of the arterial wall (145, 158). Incorporation of fiber angle distributions that vary through the wall may improve the results of parameter estimation studies (41). Here, we used mean material parameters to evaluate the predictive capabilities of constitutive relations; however, a larger sample size and using a more comprehensive method such as bootstrapping may produce a more robust analysis of the predictive power of constitutive models (30). This study also used a mean fiber distribution rather than the fiber distributions of biaxially tested arteries. While performing imaging and biaxial testing on the same artery is ideal when possible, our parameter estimation results suggest that, in most cases, directly specifying mean structural information does not significantly increase fitting errors. This study, however, did not evaluate the ability of the resulting material parameters in predicting mechanical response *a priori*. In depth analysis of fiber crimping and imaging at a wider variety of loading conditions may also allow a better estimation of the limits of affine motions.

These limitations represent examples of the limits of current experimental techniques, the scope of this dissertation as well as opportunities for future studies.

Despite these limitations the studies presented here represent a significant advance in the field of biomechanics and provide a foundation for future investigations. We developed methods for experimentally quantifying microstructural information in mouse carotid arteries and methods for incorporating the microstructural information in to a computational framework for studying growth and remodeling.

Future considerations

The results in this dissertation advance the field of biomechanics from separately investigating tissue microstructure and constitutive relations towards directly using microstructural parameters to predict mechanical response. The long term goal of this work was to develop a multi-scale, theoretical framework for investigating vascular growth and remodeling by examining the effects of biological processes on the evolution of material and microstructural parameters. Many of these biological processes have already been characterized in isolated experiments, examples include changes in expression of matrix proteases (5, 8, 9, 166), reactive oxygen species production (108, 125), ECM production (109, 135), SMC migration (96, 169) as well as many more. Incorporating these processes into a growth and remodeling framework can lead to a better understanding of interactions between the multiple hierarchical levels of biological and mechanical observations that characterize vascular growth and remodeling. The work presented in this dissertation incorporates measurements of microstructure organization into structurally-motivated constitutive relations, which can be used in a growth and remodeling model to predict the evolution of microstructure. With the techniques presented here, results of future growth and remodeling simulations can be experimentally validated at the microstructure level and at multiple time points. Improved

understanding of the mechanisms in growth and remodeling may lead to novel interventions through targeting of biological processes or through mechanically correcting the underlying pathology. We developed a novel imaging method that facilitates the direct measurement of microstructural parameters from multiphoton image stacks. The incorporation of additional structural details, such as muscle orientations (95) or elastin fenestrations (3, 101), into constitutive relations will provide a more physiologically accurate structural model and may further reduce the number of free parameters. Another unanswered question involves the role of surrounding perivascular tissue. It has been previously shown in pigs that surrounding perivascular tissue significantly affects the mechanical response of some carotid and femoral arteries (89); however in other arteries such as cerebral arteries may not be subject to tethering effect (69). Thus, it is possible that in our system, the *in vivo* pressure-diameter relationship is different than that measured in *ex vivo* tests. *In vivo* imaging techniques can capture general geometric information (Figure 7.1).

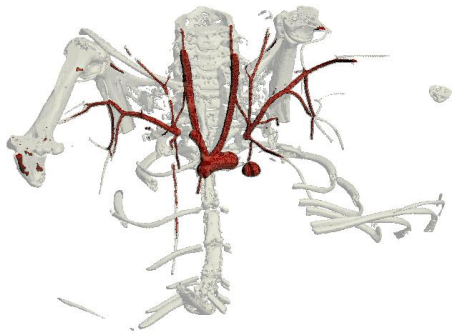

Figure 7.1: Mouse carotid arteries and associated vasculature can be visualized using micro-computed tomography (μCT) imaging.

However, accurate measurement of pressurization using viscous contrast agents remains a challenge. In addition, accurately measuring the perivascular tethering effects may be

critical when using clinically obtained *in vivo* measurements of arterial geometry. The complexity of vascular growth and remodeling is evident by the numerous experimental observations made at varying length and time scales from studying biological processes to performing mechanical characterizations. Incorporating these results into a unifying theory will not only develop further insight into the underlying mechanisms of vascular disease but will also help motivate key experiments that may identify the most impactful clinical interventions.

REFERENCES

1. **Albig A and Schiemann W.** Fibulin-5 antagonizes vascular endothelial growth factor (VEGF) signaling and angiogenic sprouting by endothelial cells. *DNA and cell biology* 23: 367, 2004.

2. **Albig AR, Neil JR, and Schiemann WP.** Fibulins 3 and 5 Antagonize Tumor Angiogenesis In vivo. *Cancer Res* 66: 2621-2629, 2006.

3. **Arribas S, Gordon J, Daly C, Dominiczak A, and McGrath J.** Confocal microscopic characterization of a lesion in a cerebral vessel of the stroke-prone spontaneously hypertensive rat. *Stroke; a journal of cerebral circulation* 27: 1118, 1996.

4. **Baek S, Gleason R, Rajagopal K, and Humphrey J.** Theory of small on large: potential utility in computations of fluid–solid interactions in arteries. *Computer Methods in Applied Mechanics and Engineering* 196: 3070-3078, 2007.

5. **Bendeck MP, Irvin C, Reidy M, Smith L, Mulholland D, Horton M, and Giachelli CM.** Smooth Muscle Cell Matrix Metalloproteinase Production Is Stimulated via {alpha}v{beta}3 Integrin. *Arterioscler Thromb Vasc Biol* 20: 1467-1472, 2000.

6. **Billiar K and Sacks M.** A method to quantify the fiber kinematics of planar tissues under biaxial stretch. *Journal of biomechanics* 30: 753-756, 1997.

7. **Brankov G, Rachev AI, and Stoychev S.** A composite model of large blood vessels. *Mechanics of Bological Solid: Proceedings of the Euromech Colloquium*, edited by Brankov G, Varna, Bulgaria. Publishing House of the Bulgarian Academy of Sciences, 1975, p. 71-78.

8. **Bruno G, Todor R, Lewis I, and Chyatte D.** Vascular extracellular matrix remodeling in cerebral aneurysms. *Journal of Neurosurgery* 89: 431-440, 1998.

9. **Budatha M, Roshanravan S, Zheng Q, Weislander C, Chapman SL, Davis EC, Starcher B, Word RA, and Yanagisawa H.** Extracellular matrix proteases contribute to progression of pelvic organ prolapse in mice and humans. *The Journal of clinical investigation* 121: 2048-2059, 2011.

10. **Busuttil R, Abou-Zamzam A, and Machleder H.** Collagenase activity of the human aorta. A comparison of patients with and without abdominal aortic aneurysms. *Archives of surgery (Chicago, Ill: 1960)* 115: 1373, 1980.

11. **Campa J, Greenhalgh R, and Powell J.** Elastin degradation in abdominal aortic aneurysms* 1. *Atherosclerosis* 65: 13-21, 1987.

12. **Chandran PL and Barocas VH.** Affine versus non-affine fibril kinematics in collagen networks: theoretical studies of network behavior. *Journal of Biomechanical Engineering* 128: 259, 2006.

13. **Chapman S, Sicot F, Davis E, Huang J, Sasaki T, Chu M, and Yanagisawa H.** Fibulin-2 and Fibulin-5 Cooperatively Function to Form the Internal Elastic Lamina and Protect From Vascular Injury. *Arteriosclerosis, thrombosis, and vascular biology* 30: 68, 2010.

14. **Cheng G, Loree H, Kamm R, Fishbein M, and Lee R.** Distribution of circumferential stress in ruptured and stable atherosclerotic lesions. A structural analysis with histopathological correlation. *Circulation* 87: 1179-1187, 1993.

15. **Choi J, Bergdahl A, Zheng Q, Starcher B, Yanagisawa H, and Davis E.** Analysis of dermal elastic fibers in the absence of fibulin-5 reveals potential roles for fibulin-5 in elastic fiber assembly. *Matrix Biology*, 2009.

16. **Chuong CJ and Fung YC.** On residual stresses in arteries. *J Biomech Eng* 108: 189-192, 1986.

17. **Csiszar K.** Lysyl oxidases: a novel multifunctional amine oxidase family. *Prog Nucleic Acid Res Mol Biol* 70: 1-32, 2001.

18. **Curci J.** Digging in the "Soil" of the Aorta to Understand the Growth of Abdominal Aortic Aneurysms. *Vascular* 17: S21, 2009.

19. **Daemen M, Lombardi D, Bosman F, and Schwartz S.** Angiotensin II induces smooth muscle cell proliferation in the normal and injured rat arterial wall. *Circulation Research* 68: 450-456, 1991.

20. **de Schepper S, Loeys B, de Paepe A, Lambert J, and Naeyaert J.** Cutis laxa of the autosomal recessive type in a consanguineous family. *European journal of dermatology: EJD* 13: 529.

21. **Del Corso L, Moruzzo D, Conte B, Agelli M, Romanelli AM, Pastine F, Protti M, Pentimone F, and Baggiani G.** Tortuosity, Kinking, and Coiling of the Carotid Artery: Expression of Atherosclerosis or Aging? *Angiology* 49: 361-371, 1998.

22. **Demiray H.** A note on the elasticity of soft biological tissues. *Journal of biomechanics* 5: 309-311, 1972.

23. **Dobrin P, Canfield T, and Sinha S.** Development of longitudina retraction of carotid arteries in neonatal dogs. *Cellular and Molecular Life Sciences (CMLS)* 31: 1295-1296, 1975.

24. **Dobrin PB.** Biaxial anisotropy of dog carotid artery: estimation of circumferential elastic modulus. *Journal of biomechanics* 19: 351-358, 1986.

25. **Dobrin PB, Schwarcz TH, and Mrkvicka R.** Longitudinal retractive force in pressurized dog and human arteries. *Journal of Surgical Research* 48: 116-120, 1990.

26. **Dollery C, McEwan J, and Henney A.** Matrix metalloproteinases and cardiovascular disease. *Circulation Research* 77: 863, 1995.

27. **Driessen NJB, Boerboom RA, Huyghe JM, Bouten CVC, and Baaijens FPT.** Computational analyses of mechanically induced collagen fiber remodeling in the aortic heart valve. *Journal of Biomechanical Engineering* 125: 549, 2003.

28. **Dye WW, Gleason RL, Wilson E, and Humphrey JD.** Altered biomechanical properties of carotid arteries in two mouse models of muscular dystrophy. *J Appl Physiol* 103: 664-672, 2007.

29. **Eberth JF, Taucer AI, Wilson E, and Humphrey JD.** Mechanics of carotid arteries in a mouse model of Marfan Syndrome. *Ann Biomed Eng* 37: 1093-1104, 2009.

30. **Ferruzzi J, Vorp DA, and Humphrey JD.** On constitutive descriptors of the biaxial mechanical behaviour of human abdominal aorta and aneurysms. *Journal of the royal society interface* 8: 435-450, 2011.

31. **Fillinger M, Raghavan M, Marra S, Cronenwett J, and Kennedy F.** In vivo analysis of mechanical wall stress and abdominal aortic aneurysm rupture risk. *Journal of vascular surgery: official publication, the Society for Vascular Surgery [and] International Society for Cardiovascular Surgery, North American Chapter* 36: 589, 2002.

32. **Fillinger MF, Racusin J, Baker RK, Cronenwett JL, Teutelink A, Schermerhorn ML, Zwolak RM, Powell RJ, Walsh DB, and Rzucidlo EM.** Anatomic characteristics of ruptured abdominal aortic aneurysm on conventional CT scans: Implications for rupture risk. *J Vasc Surg* 39: 1243-1252, 2004.

33. **Fischman DL, Leon MB, Baim DS, Schatz RA, Savage MP, Penn I, Detre K, Veltri L, Ricci D, Nobuyoshi M, Cleman M, Heuser R, Almond D, Teirstein PS, Fish RD, Colombo A, Brinker J, Moses J, Shaknovich A, Hirshfeld J, Bailey S, Ellis S, Rake R, and Goldberg S.** A Randomized Comparison of Coronary-Stent Placement and Balloon Angioplasty in the Treatment of Coronary Artery Disease. *New England Journal of Medicine* 331: 496-501, 1994.

34. **Freeman LJ, Lomas A, Hodson N, Sherratt MJ, Mellody KT, Weiss AS, Shuttleworth A, and Kielty CM.** Fibulin-5 interacts with fibrillin-1 molecules and microfibrils. *The Biochemical journal* 388: 1-5, 2005.

35. **Fridez P, Rachev A, Meister J-J, Hayashi K, and Stergiopulos N.** Model of geometrical and smooth muscle tone adaptation of carotid artery subject to step change in pressure. *American Journal of Physiology: Heart and Circulatory Physiology* 280: H2752-H2760, 2001.

36. **Fridez P, Rachev A, Meister JJ, Hayashi K, and Stergiopulos N.** Model of geometrical and smooth muscle tone adaptation of carotid artery subject to step change in pressure. *Am J Physiol Heart Circ Physiol* 280: H2752-2760, 2001.

37. **Fung Y.** *Biomechanics: Mechanical Properties of Living Tissues*: Springer, 1993.

38. **Fung Y.** Biorheology of soft tissues. *Biorheology* 10: 139, 1973.

39. **Fung Y.** *Stress, strain, growth and remodeling of living Organisms*. Basel, SUISSE: Springer, 1995.

40. **Galis ZS, Johnson C, Godin D, Magid R, Shipley JM, Senior RM, and Ivan E.** Targeted Disruption of the Matrix Metalloproteinase-9 Gene Impairs Smooth Muscle Cell Migration and Geometrical Arterial Remodeling. *Circ Res* 91: 852-859, 2002.

41. **Gasser TC, Ogden RW, and Holzapfel GA.** Hyperelastic modelling of arterial layers with distributed collagen fibre orientations. *Journal of the royal society interface* 3: 15, 2006.

42. **Giattina S, Courtney B, Herz P, Harman M, Shortkroff S, Stamper D, Liu B, Fujimoto J, and Brezinski M.** Assessment of coronary plaque collagen with polarization sensitive optical coherence tomography (PS-OCT). *International journal of cardiology* 107: 400, 2006.

43. **Gilbert TW, Sacks MS, Grashow JS, Savio LYW, Badylak SF, and Chancellor MB.** Fiber kinematics of small intestinal submucosa under biaxial and uniaxial stretch. *Journal of Biomechanical Engineering* 128: 890, 2006.

44. **Gleason R and Humphrey J.** A mixture model of arterial growth and remodeling in hypertension: altered muscle tone and tissue turnover. *Journal of Vasc Res* 41: 352-363, 2004.

45. **Gleason RL, Dye WW, Wilson E, and Humphrey JD.** Quantification of the mechanical behavior of carotid arteries from wild-type, dystrophin-deficient, and sarcoglycan-delta knockout mice. *Journal of biomechanics* 41: 3213-3218, 2008.

46. **Gleason RL, Gray SP, Wilson E, and Humphrey JD.** A multiaxial computer-controlled organ culture and biomechanical device for mouse carotid arteries. *J Biomech Eng* 126: 787-795, 2004.

47. **Gleason RL, Hu J-J, and Humphrey JD.** Building a functional artery: issue from the perspective of mechanics. *Front Biosci* 9: 2045-2055, 2004.

48. **Gleason RL and Humphrey JD.** Effects of a sustained extension on arterial growth and remodeling: a theoretical study. *J Biomech* 38: 1255-1261, 2005.

49. **Gleason RL and Humphrey JD.** A mixture model of arterial growth and remodeling in hypertension: altered muscle tone and tissue turnover. *J Vasc Res* 41: 352-363, 2004.

50. **Gleason RL, Jr. and Humphrey JD.** A 2D constrained mixture model for arterial adaptations to large changes in flow, pressure and axial stretch. *Math Med Biol* 22: 347-369, 2005.

51. **Gleason RL, Taber LA, and Humphrey JD.** A 2-D model of flow-induced alterations in the geometry, structure, and properties of carotid arteries. *J Biomech Eng* 126: 371-381, 2004.

52. **Gleason RL and Wan W.** Theory and experiments for mechanically-induced remodeling of tissue engineered blood vessels. *Advances in Science and Technology* 57: 226-234, 2008.

53. **Gleason RL, Wilson E, and Humphrey JD.** Biaxial biomechanical adaptations of mouse carotid arteries cultured at altered axial extension. *Journal of biomechanics* 40: 766-776, 2007.

54. **Greenberg CS, Birckbichler PJ, and Rice RH.** Transglutaminases: multifunctional cross-linking enzymes that stabilize tissues. *Faseb J* 5: 3071-3077, 1991.

55. **Guerin HAL and Elliott DM.** Degeneration affects the fiber reorientation of human annulus fibrosus under tensile load. *Journal of biomechanics* 39: 1410-1418, 2006.

56. **Hansen L, Wan W, and Gleason RL.** Microstructurally-motivated constitutive modeling of mouse arteries cultured under altered axial stretch. *J Biomech Eng* 131: 11, 2009.

57. **Haskett D, Johnson G, Zhou A, Utzinger U, and Vande Geest J.** Microstructural and biomechanical alterations of the human aorta as a function of age and location. *Biomechanics and Modeling in Mechanobiology* 9: 725-736, 2010.

58. **Henderson EL, Geng Y-J, Sukhova GK, Whittemore AD, Knox J, and Libby P.** Death of Smooth Muscle Cells and Expression of Mediators of Apoptosis by T Lymphocytes in Human Abdominal Aortic Aneurysms. *Circulation* 99: 96-104, 1999.

59. **Hepworth D, Steven-fountain A, Bruce D, and Vincent J.** Affine versus non-affine deformation in soft biological tissues, measured by the reorientation and stretching of collagen fibres through the thickness of compressed porcine skin. *Journal of biomechanics* 34: 341, 2001.

60. **Hirai M, Horiguchi M, Ohbayashi T, Kita T, Chien K, and Nakamura T.** Latent TGF-beta-binding protein 2 binds to DANCE/fibulin-5 and regulates elastic fiber assembly. *The EMBO Journal* 26: 3283, 2007.

61. **Hirai M, Ohbayashi T, Horiguchi M, Okawa K, Hagiwara A, Chien K, Kita T, and Nakamura T.** Fibulin-5/DANCE has an elastogenic organizer activity that is abrogated by proteolytic cleavage in vivo. *Journal of Cell Biology* 176: 1061, 2007.

62. **Holzapfel G, Gasser T, and Ogden R.** Comparison of a multi-layer structural model for arterial walls with a fung-type model, and issues of material stability. *Journal of Biomechanical Engineering* 126: 264, 2004.

63. **Holzapfel G, Gasser TC, and Ogden RW.** A New Constitutive Framework for Arterial Wall Mechanics and a Comparative Study of Material Models. *Journal of Elasticity* V61: 1-48, 2000.

64. **Hornstra IK, Birge S, Starcher B, Bailey AJ, Mecham RP, and Shapiro SD.** Lysyl oxidase is required for vascular and diaphragmatic development in mice. *The Journal of biological chemistry* 278: 14387-14393, 2003.

65. **Hu Z, Ai Q, Xu H, Ma X, Li H, Shi T, Wang C, Gong D, and Zhang X.** Fibulin-5 is down-regulated in urothelial carcinoma of bladder and inhibits growth and invasion of human bladder cancer cell line 5637. *Urologic oncology*, 2009.

66. **Huang Y, Guo X, and Kassab GS.** Axial nonuniformity of geometric and mechanical properties of mouse aorta is increased during postnatal growth. *Am J Physiol Heart Circ Physiol* 290: H657-664, 2006.

67. **Humphrey J and Rajagopal K.** A constrained mixture model for growth and remodeling of soft tissues. *Mathematical models and methods in applied sciences* 12: 407-430, 2002.

68. **Humphrey JD.** *Cardiovascular Solid Mechanics: cells, tissues, and organs/Jay D. Humphrey*: Springer, 2002.

69. **Humphrey JD and Na S.** Elastodynamics and Arterial Wall Stress. *Annals of Biomedical Engineering* 30: 509-523, 2002.

70. **Iakovou I, Schmidt T, Bonizzoni E, Ge L, Sangiorgi GM, Stankovic G, Airoldi F, Chieffo A, Montorfano M, Carlino M, Michev I, Corvaja N, Briguori C, Gerckens U, Grube E, and Colombo A.** Incidence, Predictors, and Outcome of Thrombosis After Successful Implantation of Drug-Eluting Stents. *JAMA: The Journal of the American Medical Association* 293: 2126-2130, 2005.

71. **Ishii T, Kuwaki T, Masuda Y, and Fukuda Y.** Postnatal development of blood pressure and baroreflex in mice. *Autonomic Neuroscience* 94: 34-41, 2001.

72. **Jackson ZS, Dajnowiec D, Gotlieb AI, and Langille BL.** Partial Off-Loading of Longitudinal Tension Induces Arterial Tortuosity. *Arterioscler Thromb Vasc Biol* 25: 957-962, 2005.

73. **Jackson ZS, Gotlieb AI, and Langille BL.** Wall Tissue Remodeling Regulates Longitudinal Tension in Arteries. *Circ Res* 90: 918-925, 2002.

74. **Jacob T, Hingorani A, and Ascher E.** Examination of the Apoptotic Pathway and Proteolysis in the Pathogenesis of Popliteal Artery Aneurysms. *European Journal of Vascular and Endovascular Surgery* 22: 77-85, 2001.

75. **Joannides R, Haefeli W, Linder L, Richard V, Bakkali E, Thuillez C, and Lüscher T.** Nitric oxide is responsible for flow-dependent dilatation of human peripheral conduit arteries in vivo. *Circulation* 91: 1314, 1995.

76. **Kamiya A and Togawa T.** Adaptive regulation of wall shear stress to flow change in the canine carotid artery. *Am J Physiol* 239: H14-21, 1980.

77. **Kowal RC, Richardson JA, Miano JM, and Olson EN.** EVEC, a novel epidermal growth factor-like repeat-containing protein upregulated in embryonic and diseased adult vasculature. *Circ Res* 84: 1166-1176, 1999.

78. **Kuang P, Goldstein R, Liu Y, Rishikof D, Jean J, and Joyce-Brady M.** Coordinate expression of fibulin-5/DANCE and elastin during lung injury repair. *American Journal of Physiology- Lung Cellular and Molecular Physiology* 285: 1147, 2003.

79. **Kuang P, Joyce-Brady M, Zhang X, Jean J, and Goldstein R.** Fibulin-5 gene expression in human lung fibroblasts is regulated by TGF-beta and phosphatidylinositol 3-kinase activity. *American Journal of Physiology- Cell Physiology* 291: C1412, 2006.

80. **Kuhl E and Holzapfel GA.** A continuum model for remodeling in living structures. *Journal of Materials Science* 42: 8811-8823, 2007.

81. **Lakatta EG and Levy D.** Arterial and Cardiac Aging: Major Shareholders in Cardiovascular Disease Enterprises: Part I: Aging Arteries: A "Set Up" for Vascular Disease. *Circulation* 107: 139-146, 2003.

82. **Lake S, Cortes D, Kadlowec J, Soslowsky L, and Elliott D.** Evaluation of affine fiber kinematics in human supraspinatus tendon using quantitative projection plot analysis. *Biomechanics and Modeling in Mechanobiology*: 1-9.

83. **Langille B.** Remodeling of developing and mature arteries: endothelium, smooth muscle, and matrix. *Journal of cardiovascular pharmacology* 21: S11, 1993.

84. **Lanir Y.** Constitutive equations for fibrous connective tissues. *Journal of biomechanics* 16: 1-12, 1983.

85. **Lee MJ, Roy NK, Mogford JE, Schiemann WP, and Mustoe TA.** Fibulin-5 promotes wound healing in vivo. *J Am Coll Surg* 199: 403-410, 2004.

86. **Liapis CD and Paraskevas KI.** The pivotal role of matrix metalloproteinases in the development of human abdominal aortic aneurysms. *Vasc Med* 8: 267-271, 2003.

87. **Liu M, Roubin G, and King S.** Restenosis after coronary angioplasty. Potential biologic determinants and role of intimal hyperplasia. *Circulation* 79: 1374-1387, 1989.

88. **Liu SQ and Fung YC.** Relationship Between Hypertension, Hypertrophy, and Opening Angle of Zero-Stress State of Arteries Following Aortic Constriction. *Journal of Biomechanical Engineering* 111: 325-335, 1989.

89. **Liu Y, Dang C, Garcia M, Gregersen H, and Kassab GS.** Surrounding tissues affect the passive mechanics of the vessel wall: theory and experiment. *American Journal of Physiology - Heart and Circulatory Physiology* 293: H3290-H3300, 2007.

90. **Loeys B, Van Maldergem L, Mortier G, Coucke P, Gerniers S, Naeyaert JM, and De Paepe A.** Homozygosity for a missense mutation in fibulin-5 (FBLN5) results in a severe form of cutis laxa. *Hum Mol Genet* 11: 2113-2118, 2002.

91. **Lomas A, Mellody K, Freeman L, Bax D, Shuttleworth C, and Kielty C.** Fibulin-5 binds human smooth-muscle cells through alpha5beta1 and alpha4beta1 integrins, but does not support receptor activation. *The Biochemical journal* 405: 417, 2007.

92. **Mackay J and Mensah GA.** *The Atlas of Heart Disease and Stroke*: World Health Organization, 2004.

93. **Maiellaro-Rafferty K, Weiss D, Joseph G, Wan W, Gleason RL, and Taylor WR.** Catalase overexpression in aortic smooth muscle prevents pathological mechanical changes underlying abdominal aortic aneurysm formation. *American Journal of Physiology - Heart and Circulatory Physiology*, 2011.

94. **Maki JM, Rasanen J, Tikkanen H, Sormunen R, Makikallio K, Kivirikko KI, and Soininen R.** Inactivation of the lysyl oxidase gene Lox leads to aortic aneurysms, cardiovascular dysfunction, and perinatal death in mice. *Circulation* 106: 2503-2509, 2002.

95. **Martinez-Lemus LA, Hill MA, Bolz SS, Pohl U, and Meininger GA.** Acute mechanoadaptation of vascular smooth muscle cells in response to continuous arteriolar vasoconstriction: implications for functional remodeling. *Faseb J* 18: 708-710, 2004.

96. **Mason D, Kenagy R, Hasenstab D, Bowen-Pope D, Seifert R, Coats S, Hawkins S, and Clowes A.** Matrix metalloproteinase-9 overexpression enhances vascular smooth muscle cell migration and alters remodeling in the injured rat carotid artery. *Circulation Research* 85: 1179, 1999.

97. **Materson BJ, Reda DJ, Cushman WC, Massie BM, Freis ED, Kochar MS, Hamburger RJ, Fye C, Lakshman R, Gottdiener J, Ramirez EA, and Henderson WG.** Single-Drug Therapy for Hypertension in Men -- A Comparison of Six Antihypertensive Agents with Placebo. *New England Journal of Medicine* 328: 914-921, 1993.

98. **Matsumoto T and Hayashi K.** Mechanical and dimensional adaptation of rat aorta to hypertension. *J Biomech Eng* 116: 278-283, 1994.

99. **Matsumoto T and Hayashi K.** Stress and strain distribution in hypertensive and normotensive rat aorta considering residual strain. *J Biomech Eng* 118: 62-73, 1996.

100. **McFadden EP, Stabile E, Regar E, Cheneau E, Ong ATL, Kinnaird T, Suddath WO, Weissman NJ, Torguson R, Kent KM, Pichard AD, Satler LF, Waksman R, and Serruys PW.** Late thrombosis in drug-eluting coronary stents after discontinuation of antiplatelet therapy. *The Lancet* 364: 1519-1521, 2004.

101. **Megens RT, Reitsma S, Schiffers PH, Hilgers RH, De Mey JG, Slaaf DW, oude Egbrink MG, and van Zandvoort MA.** Two-photon microscopy of vital murine elastic and muscular arteries. Combined structural and functional imaging with subcellular resolution. *Journal of vascular research* 44: 87-98, 2007.

102. **Miyashiro JK, Poppa V, and Berk BC.** Flow-Induced Vascular Remodeling in the Rat Carotid Artery Diminishes With Age. *Circ Res* 81: 311-319, 1997.

103. **Mullins R, Olvera M, Clark A, and Stone E.** Fibulin-5 distribution in human eyes: relevance to age-related macular degeneration. *Experimental eye research* 84: 378-380, 2007.

104. **Nakamura T, Lozano PR, Ikeda Y, Iwanaga Y, Hinek A, Minamisawa S, Cheng CF, Kobuke K, Dalton N, Takada Y, Tashiro K, Ross Jr J, Honjo T, and Chien KR.** Fibulin-5/DANCE is essential for elastogenesis in vivo. *Nature* 415: 171-175, 2002.

105. **Nakamura T, Ruiz-Lozano P, Lindner V, Yabe D, Taniwaki M, Furukawa Y, Kobuke K, Tashiro K, Lu Z, Andon NL, Schaub R, Matsumori A, Sasayama S, Chien KR, and Honjo T.** DANCE, a novel secreted RGD protein expressed in developing, atherosclerotic, and balloon-injured arteries. *The Journal of biological chemistry* 274: 22476-22483, 1999.

106. **Newby AC and Zaltsman AB.** Molecular mechanisms in intimal hyperplasia. *The Journal of Pathology* 190: 300-309, 2000.

107. **Ng CP, Hinz B, and Swartz MA.** Interstitial fluid flow induces myofibroblast differentiation and collagen alignment in vitro. *Journal of cell science* 118: 4731, 2005.

108. **Nguyen AD, Itoh S, Jeney V, Yanagisawa H, Fujimoto M, Ushio-Fukai M, and Fukai T.** Fibulin-5 is a novel binding protein for extracellular superoxide dismutase. *Circ Res* 95: 1067-1074, 2004.

109. **O'Callaghan CJ and Williams B.** Mechanical Strain-Induced Extracellular Matrix Production by Human Vascular Smooth Muscle Cells : Role of TGF-{beta}1. *Hypertension* 36: 319-324, 2000.

110. **Oliver JJ and Webb DJ.** Noninvasive Assessment of Arterial Stiffness and Risk of Atherosclerotic Events. *Arterioscler Thromb Vasc Biol* 23: 554-566, 2003.

111. **Owens G.** Influence of blood pressure on development of aortic medial smooth muscle hypertrophy in spontaneously hypertensive rats. *Hypertension* 9: 178, 1987.

112. **Rachev A.** A Model of Arterial Adaptation to Alterations in Blood Flow. *Journal of Elasticity* 61: 83-111, 2000.

113. **Rachev A.** Theoretical study of the effect of stress-dependent remodeling on arterial geometry under hypertensive conditions. *Journal of biomechanics* 30: 819-827, 1997.

114. **Rachev A and Hayashi K.** Theoretical study of the effects of vascular smooth muscle contraction on strain and stress distributions in arteries. *Ann Biomed Eng* 27: 459-468, 1999.

115. **Raykin J, Rachev AI, and Gleason RL, Jr.** A phenomenological model for mechanically mediated growth, remodeling, damage, and plasticity of gel-derived tissue engineered blood vessels. *J Biomech Eng* 131: 101016, 2009.

116. **Reddy GK.** Cross-linking in collagen by nonenzymatic glycation increases the matrix stiffness in rabbit achilles tendon. *Experimental diabesity research* 5: 143-153, 2004.

117. **Reiser K, McCormick RJ, and Rucker RB.** Enzymatic and nonenzymatic cross-linking of collagen and elastin. *Faseb J* 6: 2439-2449, 1992.

118. **Roach MR and Burton AC.** The reason for the shape of the distensibility curves of arteries. *Can J Biochem Physiol* 35: 681-690, 1957.

119. **Rodriguez EK, Hoger A, and McCulloch AD.** Stress-dependent finite growth in soft elastic tissues. *Journal of biomechanics* 27: 455-467, 1994.

120. **Roger VL, Go AS, Lloyd-Jones DM, Adams RJ, Berry JD, Brown TM, Carnethon MR, Dai S, de Simone G, Ford ES, Fox CS, Fullerton HJ, Gillespie C, Greenlund KJ, Hailpern SM, Heit JA, Michael Ho P, Howard VJ, Kissela BM, Kittner SJ, Lackland DT, Lichtman JH, Lisabeth LD, Makuc DM, Marcus GM, Marelli A, Matchar DB, McDermott MM, Meigs JB, Moy CS, Mozaffarian D, Mussolino ME, Nichol G, Paynter NP, Rosamond WD, Sorlie PD, Stafford RS, Turan TN, Turner MB, Wong ND, and Wylie-Rosett J.** Executive Summary: Heart Disease and Stroke Statistics—2011 Update. *Circulation* 123: 459-463, 2011.

121. **Sacks MS and Schoen FJ.** Collagen fiber disruption occurs independent of calcification in clinically explanted bioprosthetic heart valves. *Journal of Biomedical Materials Research* 62: 359-371, 2002.

122. **Sacks MS and Smith DB.** Effects of accelerated testing on porcine bioprosthetic heart valve fiber architecture. *Biomaterials* 19: 1027-1036, 1998.

123. **Sato Y, Sawada S, and Nakanuma Y.** Fibulin-5 is involved in phlebosclerosis of major portal vein branches associated with elastic fiber deposition in idiopathic portal hypertension. *Hepatology Research* 38: 166-173, 2008.

124. **Schiffrin E.** State-of-the-Art lecture. Role of endothelin-1 in hypertension. *Hypertension* 34: 876, 1999.

125. **Schluterman M, Chapman S, Korpanty G, Yanagisawa H, and Brekken R.** Fibulin-5 inhibits integrin-induced ROS production. *Matrix Biology* 27: 11-11, 2008.

126. **Schwartz SM.** Perspectives series: cell adhesion in vascular biology. Smooth muscle migration in atherosclerosis and restenosis. *Journal of Clinical Investigation* 99: 2814, 1997.

127. **Schwartz SM, Heimark R, and Majesky M.** Developmental mechanisms underlying pathology of arteries. *Physiological reviews* 70: 1177, 1990.

128. **Skalak R.** Growth as a finite displacement field. Kluwer Academic Pub, 1982, p. 347.

129. **Skalak R.** *Growth as a finite displacement field*. Martinus Nijhoff: The Hague, 1981.

130. **Skalak R, Dasgupta G, Moss M, Otten E, Dullumeijer P, and Vilmann H.** Analytical description of growth. *Journal of theoretical biology* 94: 555, 1982.

131. **Skalak R, Zargaryan S, Jain RK, Netti PA, and Hoger A.** Compatibility and the genesis of residual stress by volumetric growth. *J Math Biol* 34: 889-914, 1996.

132. **Spencer A.** *Constitutive theory for strongly anisotropic solids*: Springer-Verlag, 1984.

133. **Spencer JA, Hacker SL, Davis EC, Mecham RP, Knutsen RH, Li DY, Gerard RD, Richardson JA, Olson EN, and Yanagisawa H.** Altered vascular remodeling in fibulin-5-deficient mice reveals a role of fibulin-5 in smooth muscle cell proliferation and migration. *Proc Natl Acad Sci U S A* 102: 2946-2951, 2005.

134. **Stone E, Braun T, Russell S, Kuehn M, Lotery A, Moore P, Eastman C, Casavant T, and Sheffield V.** Missense variations in the fibulin 5 gene and age-related macular degeneration. *New England Journal of Medicine* 351: 346, 2004.

135. **Strauss BH, Robinson R, Batchelor WB, Chisholm RJ, Ravi G, Natarajan MK, Logan RA, Mehta SR, Levy DE, Ezrin AM, and Keeley FW.** In Vivo Collagen Turnover Following Experimental Balloon Angioplasty Injury and the Role of Matrix Metalloproteinases. *Circ Res* 79: 541-550, 1996.

136. **Sullivan KM, Bissonnette R, Yanagisawa H, Hussain SN, and Davis EC.** Fibulin-5 functions as an endogenous angiogenesis inhibitor. *Lab Invest* 87: 818-827, 2007.

137. **Taber LA.** A model of aortic growth based on fluid shear and fiber stresses. *Journal of Biomechanical Engineering* 120: 348-354, 1998.

138. **Taber LA and Eggers DW.** Theoretical study of stress-modulated growth in the aorta. *Journal of Theoretical Biology* 180: 343-357, 1996.

139. **Taber LA, Lin IE, and Clark EB.** Mechanics of cardiac looping. *Developmental Dynamics* 203: 42-50, 1995.

140. **Takamizawa K and Hayashi K.** Strain energy density function and uniform strain hypothesis for arterial mechanics. *Journal of biomechanics* 20: 7, 1987.

141. **Theron JG, Payelle GG, Coskun O, Huet HF, and Guimaraens L.** Carotid artery stenosis: treatment with protected balloon angioplasty and stent placement. *Radiology* 201: 627-636, 1996.

142. **Thom T, Haase N, Rosamond W, Howard VJ, Rumsfeld J, Manolio T, Zheng Z-J, Flegal K, O'Donnell C, Kittner S, Lloyd-Jones D, Goff DC, Jr., Hong Y, Members of the Statistics Committee and Stroke Statistics S, Adams R, Friday G, Furie K, Gorelick P, Kissela B, Marler J, Meigs J, Roger V, Sidney S, Sorlie P, Steinberger J, Wasserthiel-Smoller S, Wilson M, and Wolf P.** Heart Disease and Stroke Statistics--2006 Update: A Report From the American Heart Association Statistics Committee and Stroke Statistics Subcommittee. *Circulation* 113: e85-151, 2006.

143. **Thompson RW and Parks WC.** Role of matrix metalloproteinases in abdominal aortic aneurysms. *Ann N Y Acad Sci* 800: 157-174, 1996.

144. **Tiemann K, Weyer D, Djoufack PC, Ghanem A, Lewalter T, Dreiner U, Meyer R, Grohé C, and Fink KB.** Increasing myocardial contraction and blood pressure in C57BL/6 mice during early postnatal development. *American Journal of Physiology - Heart and Circulatory Physiology* 284: H464-H474, 2003.

145. **Timmins L, Wu Q, Yeh A, Moore J, and Greenwald S.** Structural Inhomogeneity and Fiber Orientation in the Inner Arterial Media. *American journal of physiology Heart and circulatory physiology*, 2010.

146. **Tsamis A and Stergiopulos N.** Arterial remodeling in response to hypertension using a constituent-based model. *Am J Physiol Heart Circ Physiol* 293: H3130-3139, 2007.

147. **Van Loon P.** Length-force and volume-pressure relationships of arteries. *Biorheology* 14: 181-201, 1977.

148. **Vorp D, Raghavan M, and Webster M.** Mechanical wall stress in abdominal aortic aneurysm: influence of diameter and asymmetry. *Journal of vascular surgery: official publication, the Society for Vascular Surgery [and] International Society for Cardiovascular Surgery, North American Chapter* 27: 632, 1998.

149. **Wachi H, Nonaka R, Sato F, Shibata-Sato K, Ishida M, Iketani S, Maeda I, Okamoto K, Urban Z, and Onoue S.** Characterization of the molecular interaction between tropoelastin and DANCE/fibulin-5. *Journal of biochemistry* 143: 633, 2008.

150. **Wagenseil JE, Ciliberto CH, Knutsen RH, Levy MA, Kovacs A, and Mecham RP.** Reduced vessel elasticity alters cardiovascular structure and function in newborn mice. *Circ Res* 104: 1217-1224, 2009.

151. **Wagenseil JE, Nerurkar NL, Knutsen RH, Okamoto RJ, Li DY, and Mecham RP.** Effects of elastin haploinsufficiency on the mechanical behavior of mouse arteries. *Am J Physiol Heart Circ Physiol* 289: H1209-1217, 2005.

152. **Wan W and Gleason R.** Constitutive modeling of mouse carotid arteries using experimentally measured microstructural parameters. *Biophysical Journal* (submitted), 2011.

153. **Wan W, Hansen L, and Gleason R.** A 3-D constrained mixture model for mechanically mediated vascular growth and remodeling. *Biomechanics and Modeling in Mechanobiology* 9: 403-419, 2010.

154. **Wan W, Yanagisawa H, and Gleason R.** Biomechanical and Microstructural Properties of Common Carotid Arteries from Fibulin-5 Null Mice. *Annals of Biomedical Engineering* 38: 1-13, 2010.

155. **Wang X, LeMaire S, Chen L, Carter S, Shen Y, Gan Y, Bartsch H, Wilks J, Utama B, and Ou H.** Decreased expression of fibulin-5 correlates with reduced elastin in thoracic aortic dissection. *Surgery* 138: 352-359, 2005.

156. **Watton PN, Hill NA, and Heil M.** A mathematical model for the growth of the abdominal aortic aneurysm. *Biomechanics and modeling in mechanobiology* 3: 98-113, 2004.

157. **Weber T, Auer J, O'Rourke MF, Kvas E, Lassnig E, Berent R, and Eber B.** Arterial Stiffness, Wave Reflections, and the Risk of Coronary Artery Disease. *Circulation* 109: 184-189, 2004.

158. **Wicker BK, Hutchens HP, Wu Q, Yeh AT, and Humphrey JD.** Normal basilar artery structure and biaxial mechanical behaviour. *Computer Methods in Biomechanics and Biomedical Engineering* 11: 539 - 551, 2008.

159. **Wiesmann F, Ruff J, Hiller K-H, Rommel E, Haase A, and Neubauer S.** Developmental changes of cardiac function and mass assessed with MRI in neonatal, juvenile, and adult mice. *American Journal of Physiology - Heart and Circulatory Physiology* 278: H652-H657, 2000.

160. **Wlazlinski A, Engers R, Hoffmann MJ, Hader C, Jung V, Müller M, and Schulz WA.** Downregulation of several fibulin genes in prostate cancer. *The Prostate* 67: 1770-1780, 2007.

161. **Wolinsky H.** Response of the rat aortic media to hypertension. Morphological and chemical studies. *Circ Res* 26: 507-522, 1970.

162. **Wong LC and Langille BL.** Developmental remodeling of the internal elastic lamina of rabbit arteries: effect of blood flow. *Circ Res* 78: 799-805, 1996.

163. **Xie L, Palmsten K, MacDonald B, Kieran M, Potenta S, Vong S, and Kalluri R.** Basement membrane derived fibulin-1 and fibulin-5 function as angiogenesis inhibitors and suppress tumor growth. *Experimental biology and medicine (Maywood, NJ)* 233: 155, 2008.

164. **Yanagisawa H, Davis EC, Starcher BC, Ouchi T, Yanagisawa M, Richardson JA, and Olson EN.** Fibulin-5 is an elastin-binding protein essential for elastic fibre development in vivo. *Nature* 415: 168-171, 2002.

165. **Yang M, Mun C, Choi Y, Baik J, Park A, Lee W, and Lee J.** Agmatine inhibits matrix metalloproteinase-9 via endothelial nitric oxide synthase in cerebral endothelial cells. *Neurol Res* 29: 749-754, 2007.

166. **Yue W, Sun Q, Landreneau R, Wu C, Siegfried JM, Yu J, and Zhang L.** Fibulin-5 Suppresses Lung Cancer Invasion by Inhibiting Matrix Metalloproteinase-7 Expression. *Cancer Res* 69: 6339-6346, 2009.

167. **Zanchi A, Wiesel P, Aubert J-F, Brunner HR, and Hayoz D.** Time Course Changes of the Mechanical Properties of the Carotid Artery in Renal Hypertensive Rats. *Hypertension* 29: 1199-1203, 1997.

168. **Zarins CK, Zatina MA, Giddens DP, Ku DN, and Glagov S.** Shear stress regulation of artery lumen diameter in experimental atherogenesis. *J Vasc Surg* 5: 413-420, 1987.

169. **Zempo N, Koyama N, Kenagy R, Lea H, and Clowes A.** Regulation of vascular smooth muscle cell migration and proliferation in vitro and in injured rat arteries

by a synthetic matrix metalloproteinase inhibitor. *Arteriosclerosis, thrombosis, and vascular biology* 16: 28, 1996.

170. **Zheng Q, Choi J, Rouleau L, Leask RL, Richardson JA, Davis EC, and Yanagisawa H.** Normal Wound Healing in Mice Deficient for Fibulin-5, an Elastin Binding Protein Essential for Dermal Elastic Fiber Assembly. *J Invest Dermatol* 126: 2707-2714, 2006.

171. **Zheng Q, Davis EC, Richardson JA, Starcher BC, Li T, Gerard RD, and Yanagisawa H.** Molecular Analysis of Fibulin-5 Function during De Novo Synthesis of Elastic Fibers. *Mol Cell Biol* 27: 1083-1095, 2007.

172. **Zoumi A, Lu X, Kassab GS, and Tromberg BJ.** Imaging coronary artery microstructure using second-harmonic and two-photon fluorescence microscopy. *Biophys J* 87: 2778-2786, 2004.

173. **Zoumi A, Yeh A, and Tromberg BJ.** Imaging cells and extracellular matrix in vivo by using second-harmonic generation and two-photon excited fluorescence. *Proc Natl Acad Sci U S A* 99: 11014-11019, 2002.

174. **Zulliger MA, Fridez P, Hayashi K, and Stergiopulos N.** A strain energy function for arteries accounting for wall composition and structure. *Journal of biomechanics* 37: 989-1000, 2004.

175. **Zulliger MA, Rachev A, and Stergiopulos N.** A constitutive formulation of arterial mechanics including vascular smooth muscle tone. *Am J Physiol Heart Circ Physiol* 287: H1335-1343, 2004.